Studies on Electrochemical Reactions Using Concentrated Aqueous Electrolytes

Shota Inoguchi

2021

Studies on Electrochemical Reactions Using Concentrated Aqueous Electrolytes

Shota Inoguchi

Department of Materials Science and Engineering

Graduate School of Engineering

Kyoto University

March 2021

Contents

General introduction

1. Solution chemistry involved in electrochemical processes

Electrochemical processes are essential in broad fields such as hydrometallurgy, surface finishing, electronics packaging, and energy storage. Because electrochemical reactions involve electric charges transferring between electrodes and a solute, solution chemistry is intimately involved in understanding and developing electrochemical processes.

Aqueous electrolytes are used in many industrial electrolysis processes. However, the electrochemical window of water limits electrochemical processes in aqueous systems . In the case of metal species with a negative electrode potential, the species are not electrodeposited from aqueous systems because hydrogen evolution reactions occur due to the reduction of water and/or proton. Besides, when aqueous solutions are utilized as electrolytes for energy storage, such as batteries and capacitors, the low stability of water involves a low voltage of the devices.

For broader electrochemical processes and the enhanced performances of electrochemical devices, non-aqueous solvents that are difficult to be reduced and/or oxidized compared to water, such as organic solvents, ionic liquids, and molten salts, are essential. For example, organic solvents are utilized as electrolytes in energy storage (*e.g.*, lithium-ion batteries) because their wider potential window than water enhances operating voltages.[1] Besides, molten salts are indispensable to produce various substances, such as metals with a negative electrode potential (*e.g.*, sodium (Na) and aluminum (Al)) and fluorine gases, and so on.[2] However, there are desirable conditions for operating the non-aqueous solvents. For organic solvents and ionic liquids, because the contamination of water and

oxygen sometimes degrades the electrolytic solutions, associated instruments to prevent the contamination are necessary. In addition, molten salt electrolysis is usually conducted at high temperatures, giving heavy environmental burdens and high costs. Therefore, although the use of non-aqueous solvents offers tremendous advantages, they are more difficult to be handled than aqueous solutions and need to prepare associated instruments, resulting in complex processes and increased costs.

2. Applications of concentrated aqueous electrolytes to electrochemical processes

The low stability of water gives the necessity of non-aqueous solvents and associated instruments in some electrochemical processes and devices. If the electrochemical stability of water increases, the enhanced stability can improve device performances and expand electrochemical processes using aqueous systems. Besides, since aqueous solutions are easy to be handled without concern for water or oxygen contamination, replacing non-aqueous solvents with aqueous solutions can eliminate the associated instruments and simplify the processes.

An effective approach to improving the water stability is an increase in solute concentration, *i.e.*, the use of concentrated aqueous electrolytes. Concentrated aqueous electrolytes have different structures from conventional aqueous systems, *i.e.*, dilute aqueous solutions with high water content, because the proportion of water molecules coordinating to dissolved ions increases. In other words, uncoordinated water, which is so-called free water, decreases in concentrated electrolytes. Figure G.1 shows schematic illustrations of a structure of dilute and concentrated aqueous electrolytes.

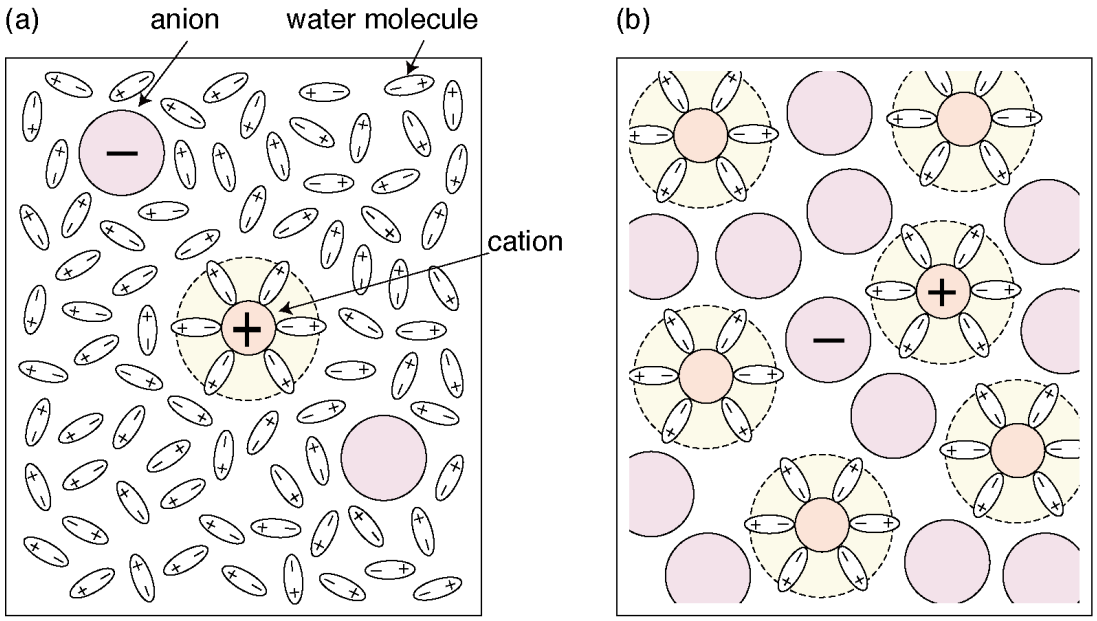

Figure G.1 Schematic illustrations of (a) dilute and (b) concentrated aqueous electrolytes.

Aqueous solutions with extremely high solute concentrations and low water contents have been investigated for about half a century.[3–13] However, the studies on the highly-concentrated solutions have been limited to the measurements of physicochemical properties, and the applications to industrial processes, such as electrochemical processes, have been seldom attempted. The attention to highly-concentrated aqueous solutions has revived within this decade regarding their application to electrochemical processes. Since the expansion of the potential window of water to *ca.* 3.0 V has been reported for a 21 mol kg^{-1} lithium bis(trifluoromethylsulfonyl)amide ($LiTf_2N$, Tf = SO_2CF_3) aqueous solution,[14] several studies have attempted to apply the concentrated aqueous systems to energy storage.[15–28] For the applications of the concentrated systems to energy storage, metal salts with substantially high solubility in water and their compositions have been specially investigated to further decrease water content and thus expand the potential window.[15–19]

As well as energy storage, concentrated aqueous electrolytes with

improved water stability have been applied to surface finishing that is impossible using conventional aqueous solutions with high water content, *e.g.*, electrodeposition,[26–31] and anodization.[32,33] As an example of using the concentrated systems for metal electrodeposition, chromium (Cr) electrodeposition with high current efficiency has been demonstrated in highly-concentrated lithium chloride (LiCl) or calcium chloride ($CaCl_2$) aqueous solutions containing Cr^{3+} salts.[30] Beside, the concentrated systems have also been expected as electrolytes for zinc-air secondary batteries because an increase in zinc (Zn) salt concentration improves water stability and inhibits dendritic Zn precipitation during repeating charge-discharge cycles.[26,27] In the case of anodization, the use of concentrated $LiTf_2N$ aqueous electrolytes has been reported to save alternating current in the fabrication of anodized black-colored aluminum.[33] Therefore, concentrated aqueous electrolytes with higher water stability are expected to apply for various electrochemical processes, *e.g.*, energy storages, surface finishing.

In addition to the use of concentrated bulk electrolytes, a combination of controlling electrode shape and selecting solutes can also create a spontaneous environment where solute concentrations are locally increased. Several investigations have demonstrated that confinement of aqueous solutions within nanospaces of porous materials gives different properties from bulk solutions.[34–38] In the case of a kind of porous material, *i.e.*, porous silicon (Si) obtained by anodizing single-crystalline Si in hydrofluoric acid solution, unique properties of solutions confined within nanopores have also been reported. Surface-induced interactions are one of unique phenomena that occur within the nanopores of the porous Si with hydrophobic surfaces. Theoretical analyses have suggested that, even when the bulk is stable as a single phase, the interactions can create a second phase with high concentrations of hydrophobic solutes in the vicinity of a hydrophobic surface.[39,40] It has demonstrated the fast supply of precursors and the spontaneous formation of a concentrated phase within the nanopores under the surface-induced interactions between hydrophobic

nanoporous Si and hydrophobic solutes with low charge density.[41–45] Controlling the pore size of porous electrodes and the use of hydrophobic solutes give to spontaneously increase solute concentration, giving the dense metal deposition and the control of local pH within the nanopores.

3. Enhancement of the properties of dissolved ions by increasing the solute concentration of aqueous electrolytes

As mentioned in the previous section, lower water content improves water stability due to the increase in solute concentrations. Besides, the increase in solute concentrations is expected to enhance the effects of dissolved ions on water molecules, giving changes in solution structures and electrochemical reactions associated with water in concentrated aqueous electrolytes.

Interactions between dissolved ions and water molecules, such as hydration, depend on dissolved ions. Figure G.2 shows schematic illustrations of the interactions between dissolved ions and water molecules in dilute aqueous solutions with various solutes. In the case of hydrophilic cations with a small size and high charge density (*e.g.*, metal cations), water molecules are strongly coordinated to the cations (Figure G.2(a)). On the other hand, in the cases of hydrophobic cations with a large size and low charge density, such as quaternary alkylammonium cations (*e.g.*, tetraethylammonium (TEA^+) cations and tetrabuthylammonium (TBA^+) cations), their low affinity with water molecules give to weakly hydrate to the cations and get stronger hydrogen bonds among water molecules around the cations, *i.e.*, hydrophobic hydration (Figure G.2(b)).[46–48] As with cation species, hydration behaviors depend on anion species. Although interactions between dissolved ions and water molecules for anions are usually less significant than those for cations, some anions, such as perchlorate (ClO_4^-) anions and Tf_2N^- anions, are known to form strong

hydrogen bonds with water molecules (Figure G.2(c)).[15,49,50] In addition, the increase in the hydrogen-bonded anion concentration gives rise to break hydrogen-bonding networks formed by interactions among free water molecules in aqueous solutions.[47,48]

The increase in solute concentrations increases the number of water molecules affected by dissolved ions and thus highlights the effects of the dissolved ions on hydration behaviors and hydrogen-bonding networks. Therefore, the enhanced effects involve the properties of aqueous electrolytes and electrochemical reactions associated with water in aqueous solutions. Appropriate selections of solutes used in concentrated aqueous solutions can further broaden the electrochemical processes in aqueous electrolytes and enhance the device performances using aqueous systems.

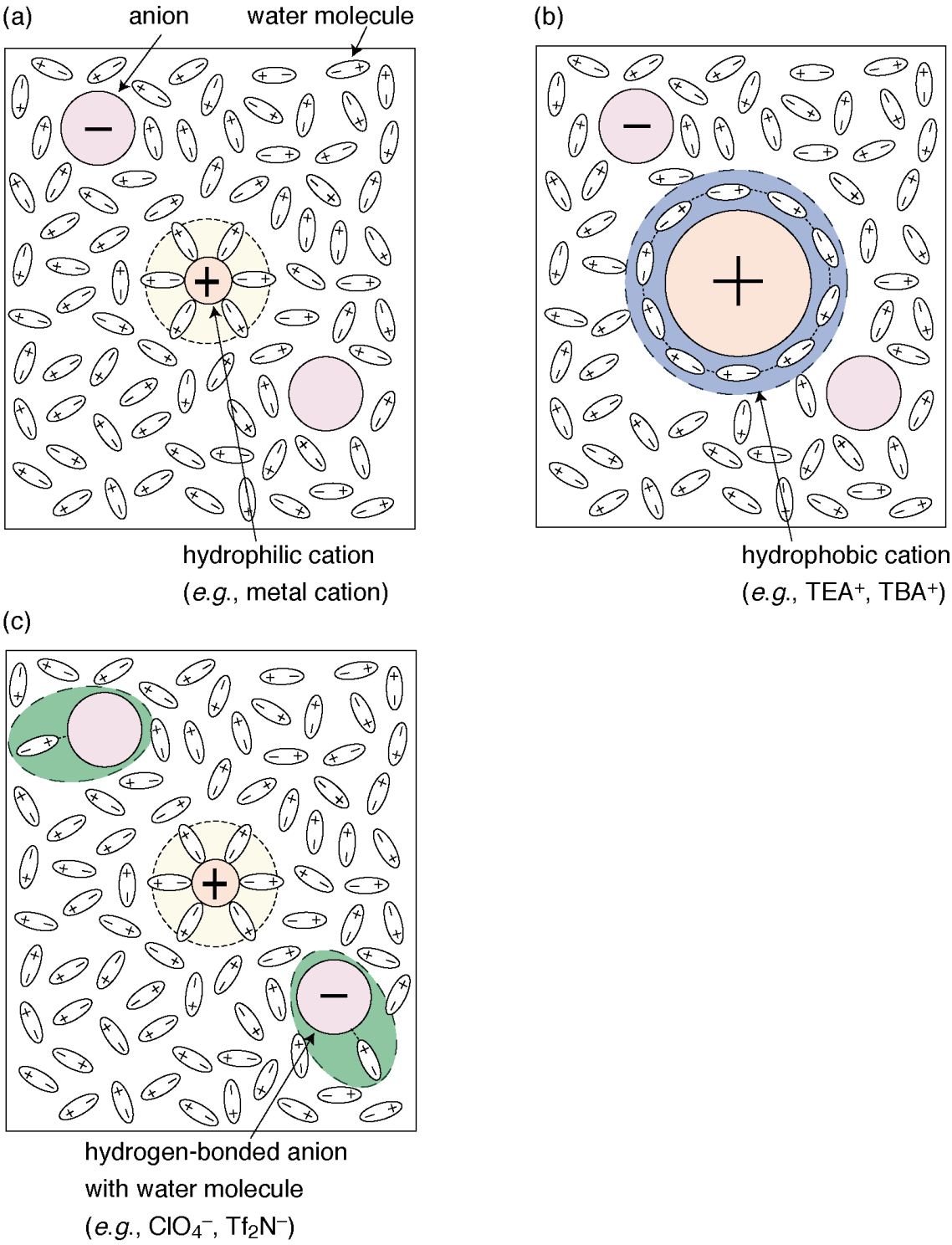

Figure G.2 Schematic illustrations of the interactions between dissolved ions and water molecules in dilute aqueous solutions containing (a) hydrophilic cations, (b) hydrophobic cations, and (c) hydrogen-bonded anions with water molecules.

4. Outline of the present thesis

Although concentrated aqueous systems with numerous advantages for applications in various electrochemical processes have been actively investigated, unknowns and potentials of the aqueous solutions are still present, *e.g.*, in terms of the enhanced effects of solutes on water molecules. The present thesis aims at investigating electrochemical reactions using concentrated aqueous electrolytes in terms of the enhanced unique properties of dissolved ions. Three studies were conducted using concentrated aqueous electrolytes with the enhanced unique properties. The first is Zn electrodeposition, which competes with hydrogen evolution/adsorption. The second is the adsorption/desorption behaviors of hydrogen underpotential deposition (H_{upd}) on platinum (Pt) electrodes. The third is the enrichment behaviors of hydrophobic cations and hydrolytic reactivity of metal salts within nanoporous Si electrodes.

In chapter 1, the effects of loss of free water in concentrated aqueous solutions on Zn electrodeposition that competes with hydrogen evolution/adsorption were investigated. The electrodeposition was conducted in two types of solutions: concentrated $Zn(Tf_2N)_2$ solutions with the breakdown of the hydrogen-bonding networks and loss of free water, and concentrated $ZnSO_4$ solutions without them. Only with concentrated $Zn(Tf_2N)_2$ solutions, basal-plane oriented electrodeposited Zn was obtained. This is because the decrease in the contribution of adsorbed hydrogen to Zn electrodeposition gives rise to promote surface diffusion of Zn adions and the growth of the basal planes with the lowest surface free energy.

In chapter 2, the dependences of concentrations and anions on proton reduction and H_{upd} adsorption/desorption on polycrystalline Pt electrodes using acidic lithium salt solutions were investigated. Three types of aqueous electrolytes, LiCl, $LiTf_2N$, and $LiClO_4$ solutions, were used. The proton reduction at the equilibrium potential of H^+/H_2 was suppressed with increasing lithium salt concentration, regardless of anions, due to a tight

supply of proton to electrodes. The H_{upd} adsorption/desorption behaviors depended on anions, suggesting that anion species affect local pH in the vicinity of the Pt electrode. Effects of the presence or breakdown of the hydrogen-bonding networks on the adsorption/desorption and the local conditions in the vicinity of electrodes are also discussed.

In chapter 3, the dependence of the bulk TEA^+ concentration on the spontaneous TEA^+ enrichment within hydrophobic nanopores of porous Si was investigated. The enrichment behaviors were evaluated by electrochemical measurements and thermal analysis. Increasing bulk TEA^+ concentration enhanced the enrichment behavior, resulting in an increased local pH of aqueous solutions confined within the nanopores. Besides, the hydrolytic reactivity of Zn^{2+} cations in the TEA^+ accumulated solution within the nanopores was also investigated and discussed as model cases to evaluate reactivities of metal cations in nanoconfined solutions.

References

1. K. Izutsu, *Electrochemistry in Nonaqueous Solutions*, Wiley, New York, 313 (2002).
2. G. Mamantov, R. Marassi, *Molten Salt Chemistry: An Introduction and Selected Application*s, Springer Netherlands, Dordrecht, **73**, 417 (1987).
3. C. A. Angell, *J. Electrochem. Soc.*, **112**, 1224 (1965).
4. C. T. Moynihan, C. R. Smalley, C. A. Angell, and E. J. Sare, *J. Phys. Chem.*, **73**, 2287 (1969).
5. C. A. Angell and J. C. Tucker, *J. Phys. Chem.*, **78**, 278 (1974).
6. D. R. MacFarlane and C. A. Angell, *J. Phys. Chem.*, **88**, 4779 (1984).
7. S. Deki, M. Ohtawa, and Y. Kanaji, *J. Chem. Soc. Jpn.* (in Japanese), **12**, 1623 (1979).

8. T. B. Tripp, *J. Chem. Thermodyn.*, **7**, 263 (1975).
9. J. H. Ambrus, C. T. Moynihan, and P. B. Macedo, *J. Electrochem. Soc.*, **119**, 192 (1972).
10. L. Greenspan, *J. Res. Natl. Bur. Stand. Phys. Chem.*, **81**, 89 (1977).
11. M. E. Guendouzi, A. Mounir, and A. Dinane, *J. Chem. Thermodyn.*, **35**, 209 (2003).
12. J. A. Rard and S. L. Clegg, *J. Chem. Eng. Data*, **42**, 819 (1997).
13. H. Majima and Y. Awakura, *Metall. Trans. B*, **19**, 347 (1988).
14. L. Suo, O. Borodin, T. Gao, M. Olguin, J. Ho, X. Fan, C. Luo, C. Wang, and K. Xu, *Science*, **350**, 938 (2015).
15. Y. Yamada, K. Usui, K. Sodeyama, S. Ko, Y. Tateyama, and A. Yamada, *Nat. Energy*, **1**, 1 (2016).
16. L. Suo, O. Borodin, W. Sun, X. Fan, C. Yang, F. Wang, T. Gao, Z. Ma, M. Schroeder, A. von Cresce, M. Russell, M. Armand, A. Angell, K. Xu, and C. Wang, *Angew. Chem. Int. Ed.*, **128**, 7252 (2016).
17. C. Yang, J. Chen, T. Qing, X. Fan, W. Sun, A. von Cresce, M. S. Ding, O. Borodin, J. Vatamanu, M. A. Schroeder, N. Eidson, C. Wang, and K. Xu, *Joule*, 1, 122 (2017).
18. L. Chen, J. Zhang, Q. Li, J. Vatamanu, X. Ji, T. P. Pollard, C. Cui, S. Hou, J. Chen, C. Yang, L. Ma, M. S. Ding, M. Garaga, S. Greenbaum, H. Lee, O. Bolodin, K. Xu, and C. Wang, *ACS Energy Lett.*, **5**, 968 (2020).
19. S. Ko, Y. Yamada, and A. Yamada, *Electrochem. Commun.*, **116**, 106764 (2020).
20 L. Coustan, G. Shul, and D. Bélanger, *Electrochem. Commun.*, **77**, 89 (2017).
21. Y. Yokoyama, T. Fukutsuka, K. Miyazaki, and T. Abe, *J. Electrochem. Soc.*, **165**, A3299 (2018).
22. P. Lannelongue, R. Bouchal, E. Mourad, C. Bodin, M. Olarte, S. le Vot, F. Favier, and O. Fontaine, *J. Electrochem. Soc.*, **165**, A657 (2018).

23. W. Deng, X. Wang, C. Liu, C. Li, J. Chen, N. Zhu, R. Li, and M. Xue, *Energy Storage Mater.*, **20**, 373 (2019).
24. W. S. V. Lee, T. Xiong, G. C. Loh, T. L. Tan, and J. Xue, *ACS Appl. Energy Mater.*, **1**, 3070 (2018).
25. D. Reber, R. S. Kühnel, and C. Battaglia, *Sustain. Energy Fuels*, **1**, 2155 (2017).
26. F. Wang, O. Borodin, T. Gao, X. Fan, W. Sun, F. Han, A. Faraone, J. A. Dura, K. Xu, and C. Wang, *Nat. Mater.*, **17**, 543 (2018).
27. C. Y. Chen, K. Matsumoto, K. Kubota, R. Hagiwara, and Q. Xu, *Adv. Energy Mater.*, **9**, 1 (2019).
28. N. Zhang, F. Cheng, Y. Liu, Q. Zhao, K. Lei, C. Chen, X. Liu, and J. Chen, *J. Am. Chem. Soc.*, **138**, 12894 (2016).
29. K. Adachi, A. Kitada, K. Fukami, and K. Murase, *J. Electrochem. Soc.*, **166**, D409 (2019).
30. K. Adachi, A. Kitada, K. Fukami, and K. Murase, *Electrochim. Acta*, **338**, 135873 (2020).
31. Q. Huang and Y. Hu, *J. Electrochem. Soc.*, **165**, D796 (2018).
32. R. S. Kühnel, D. Reber, A. Remhof, R. Figi, D. Bleiner, and C. Battaglia, *Chem. Commun.*, **52**, 10435 (2016).
33. A. Kitada, M. Kurihara, R. Takai, K. Fukami, and K. Murase, *J. Surf. Finish. Soc. Jpn.*, **71**, 376 (2020).
34. K. Otake, K. Otsubo, T. Komatsu, S. Dekura, J. M. Taylor, R. Ikeda, K. Sugimoto, K. Fujiwara, C. P. Chou, A. W. Sakti, Y. Nishimura, H. Nakai, and H. Kitagawa, *Nat. Commun.*, **11** (2020).
35. S. Jonchhe, S. Pandey, T. Emura, K. Hidaka, M. A. Hossain, P. Shrestha, H. Sugiyama, M. Endo, and H. Mao, *Proc. Natl. Acad. Sci. U. S. A.*, **115**, 9539 (2018).
36. K. Mawatari, Y. Kazoe, H. Shimizu, Y. Pihosh, and T. Kitamori, *Anal. Chem.*, **86**, 4068 (2014).
37. K. V. Agrawal, S. Shimizu, L. W. Drahushuk, D. Kilcoyne, and M. S. Strano, *Nat. Nanotechnol.*, **12**, 267 (2017).

38. W. Choi, Z. W. Ulissi, S. F. E. Shimizu, D. O. Bellisario, M. D. Ellison, and M. S. Strano, *Nat. Commun.*, **4**, 1 (2013).
39. M. Kinoshita, *J. Solution Chem.*, **33**, 661 (2004).
40. M. Kinoshita, *Biophys. Rev.*, **5**, 283 (2013).
41. K. Fukami, R. Koda, T. Sakka, Y. Ogata, and M. Kinoshita, *J. Chem. Phys.*, **138** (2013).
42. R. Koda, A. Koyama, K. Fukami, N. Nishi, T. Sakka, T. Abe, A. Kitada, K. Murase, and M. Kinoshita, *J. Chem. Phys.*, **141** (2014).
43. A. Koyama, K. Fukami, T. Sakka, T. Abe, A. Kitada, K. Murase, and M. Kinoshita, *J. Phys. Chem. C*, **119**, 19105 (2015).
44. A. Koyama, K. Fukami, Y. Suzuki, A. Kitada, T. Sakka, T. Abe, K. Murase, and M. Kinoshita, *J. Phys. Chem. C*, **120**, 24112 (2016).
45. A. Koyama, K. Fukami, Y. Imaoka, A. Kitada, T. Sakka, T. Abe, K. Murase, and M. Kinoshita, *Phys. Chem. Chem. Phys.*, **19**, 16323 (2017).
46. J. Stangret and T. Gampe, *J. Phys. Chem. A*, **106**, 5393 (2002).
47. T. Takekiyo and Y. Yoshimura, *J. Phys. Chem. A*, **110**, 10829 (2006).
48. J. Stangret and T. Gampe, *J. Phys. Chem. B*, **103**, 3778 (1999).
49. A. W. Omta, M. F. Kropman, S. Woutersen, and H. J. Bakker, *J. Chem. Phys.*, **119**, 12457 (2003).
50. Y. Chen, Y. Zhang, and L. Zhao, *Phys. Chem. Chem. Phys.*, **6**, 537 (2004).

Chapter 1

Basal-plane orientation of zinc electrodeposits induced by loss of free water in concentrated aqueous solutions

1.1. Introduction

The electrochemical window of water limits electrochemical reactions in aqueous media. The low stability of water involves not only the low voltage of storage batteries but also a limit to metal species electrodeposited from aqueous systems. An effective approach to improve water stability is an increase in solute concentration, *i.e.* the use of concentrated aqueous solutions.

Although aqueous solutions with extremely high concentrations have been studied for about half a century,[1–4] the attention to highly-concentrated aqueous solutions has revived within this decade. The expansion of the potential window to *ca.* 3.0 V has been reported for a 21 mol kg^{-1} lithium bis(trifluoromethylsulfonyl)amide ($LiTf_2N$, Tf = SO_2CF_3) aqueous solution.[5] In such concentrated aqueous solutions, the amount of free water is considerably decreased to suppress water electrolysis, which is beneficial for energy storage,[6–11] surface finishing,[12–16] and so on. For example, zinc (Zn) electrodeposition from concentrated zinc chloride ($ZnCl_2$) aqueous solutions have demonstrated the suppression of both water decomposition and dendritic growth, which is promising for zinc-air batteries.[9] However, nothing has been studied so far on crystallization mechanism in concentrated aqueous solutions, *i.e.*, how the decrease in free water affects the crystallization process of electrodeposits is unknown.

Zn electrodeposition thermodynamically competes with hydrogen evolution and/or adsorption because of the relatively negative electrode

potential (Zn^{2+} + 2e = Zn; $E°$ = –0.76 V *vs*. SHE). However, the hydrogen overpotential is large for Zn and the current efficiency is more than 90% even in conventional aqueous solutions with much amount of free water. In other words, Zn electrodeposition from concentrated aqueous solutions is a good example to examine the effect of a decrease in free water on electrodeposition behaviors because there is no need to take into account the change in current efficiency that affects electrodeposition behaviors.

To identify how the decrease in free water affects Zn electrodeposition behaviors, concentrated aqueous solutions where zinc cations exist as hydrated ions and counter anions are electrochemically stable are desired. In other words, the use of anions is undesirable that coordinate with metal cations and/or are easily reduced. For this reason, the author use neither Cl^- anions that coordinate with Zn^{2+},[10,17] nor nitrate (NO_3^-) anions that decompose into nitrite (NO_2^-) anions during cathodic reactions.[18,19] In this study, the author report Zn electrodeposition behaviors using concentrated $Zn(Tf_2N)_2$ aqueous solutions. In this system, the hydration of metal cations and the decrease in free water are considered to occur as in concentrated $LiTf_2N$ aqueous solutions. For comparison, electrodeposition from concentrated zinc sulfate (SO_4^{2-}) solutions are also studied.

1.2. Experimental

Materials and preparation. Zinc sulfate heptahydrates ($ZnSO_4 \cdot 7H_2O$; Nacalai tesque, ≥ 99.0% purity) was used as purchased. $Zn(Tf_2N)_2$ was synthesized from bis(trifluoromethylsulfonyl)imide (HTf_2N; Fluka, ≥ 95.0% purity) and basic zinc carbonate ($2ZnCO_3 \cdot 3Zn(OH)_2$; Nacalai tesque, chemical pure grade) through acid-base reactions. Their aqueous solutions were prepared with ultra-pure water (18.2 MΩ cm, Millipore, Milli-Q Reference A+). HTf_2N (20 mmol) and $2ZnCO_3 \cdot 3Zn(OH)_2$ (4 mmol) in 20 mL of water were stirred at 500 rpm at 70 °C for 2 h. They were heated at

120 °C for 12 h to remove excess water. A white, hygroscopic solid was obtained at room temperature. The water amount in this salt was measured by coulometric Karl-Fischer titration. The molalities of $ZnSO_4$ or $Zn(Tf_2N)_2$ solutions were adjusted to 0.1, 0.5, 1.0, 2.0, and 3.5 mol kg^{-1}. The author also prepared $ZnSO_4$-$Zn(Tf_2N)_2$ mixed solutions at total Zn^{2+} molality of 2.0 mol kg^{-1}, where molar fractions of $Zn(Tf_2N)_2$, x = $[Zn(Tf_2N)_2]/\{[Zn(Tf_2N)_2] + [ZnSO_4]\}$, were adjusted to be 0.01, 0.10, and 0.20.

Vibration spectroscopy. For Infrared (IR) measurement, a JASCO FT/IR–460 plus system was used with barium fluoride (BaF_2) window materials. For Raman spectroscopy, an integrated Raman system (B&W Tek, innoRam 785) —consisting of a semiconductor laser light source (785 nm), an axial transmissive spectrograph, a holographic probe head, and a CCD detector— was used. For pH measurements, a pH meter (HORIBA, Laquaact D-71) was used.

Electrochemical cells. Electrochemical measurements were performed at room temperature (RT) using a potentiostat (Bio-Logic Science Instruments, SP-150) by three-electrode method: Cu substrate (YAMAMOTO-MS) as the working electrode (WE), Zn sheet (Nilaco, ≥ 99.99% purity) as the counter electrode (CE), Ag/AgCl electrode immersed in 3.0 M (= mol dm^{-3}) sodium chloride (NaCl) aqueous solution as the reference electrode (RE). The RE was separated from the main solution by porous Vycor glass. NaCl was used instead of potassium chloride (KCl) to avoid precipitation of less-soluble potassium bis(trifluoromethylsulfonyl)amide (KTf_2N) at the Vycor glass. The potential of the RE is 0.226 ± 0.004 V vs. SHE.[20] The liquid junction potential in the RE caused by the difference of ionic mobility between Na^+ cations and Cl^- anions was calculated from Henderson's equation, resulting in below 10 mV. Before the electrochemical measurements, Cu substrate

was ultrasonically cleaned by acetone and ethanol for 20 min and 10 min, respectively.

Electrochemical measurements. Linear sweep voltammetry was performed at a scan rate of 10 mV s^{-1}. Prior to linear sweep voltammetry for each electrolyte, the solution resistance was determined by electrochemical impedance spectroscopies at a frequency of 100 kHz and AC voltage amplitude of 20 mV to compensate for the ohmic drop between the WE and the RE.

Electrodeposition and characterization of electrodeposits. Galvanostatic electrolysis was carried out at a current density of 50 mA cm^{-2} for 400 s without any agitation at RT by the same potentiostat and RE referred before. The thickness of electrodeposits was always *ca*. 10 μm that is thick is enough to eliminate the influence of Cu substrate on Zn electrodeposition, *e.g*. epitaxial growth. To calculate the current efficiency, the weight of the electrodeposits was calculated by comparing the weight of the substrate before and after the electrodeposition. The efficiency was calculated by dividing the weight of the obtained electrodeposits by the weight of the elemental zinc that would be obtained if the current efficiency were 100%. To characterize the electrodeposits, X-ray diffraction (XRD) measurements with Cu*Kα* (λ = 0.1542 nm and scanning electron microscope (SEM) observations were performed using Rigaku RINT2200 and KEYENCE VE-8800, respectively.

1.3. Results and discussion

1.3.1. Infrared spectroscopy.

The presence of free water was examined in $Zn(Tf_2N)_2$ and $ZnSO_4$ solutions with various concentrations. Figure 1.1 shows the IR spectra of

O-H stretching vibration. Broad absorptions ranging from 3000 to 3800 cm^{-1} are observed in 0.1–0.5 mol kg^{-1} $Zn(Tf_2N)_2$ and all $ZnSO_4$ solutions, proving the existence of hydrogen-bonding networks of water clusters.[21] By contrast, increasing $Zn(Tf_2N)_2$ molality leads to a different situation: The higher shift in O-H vibration ranging from 3200–3500 cm^{-1} to 3500–3700 cm^{-1} indicates that hydrogen-bonding networks of water clusters are broken.

Similar shifts have also been observed in $LiTf_2N$ hydrate melts and concentrated aqueous solutions containing perchlorate (ClO_4^-) anions.[6,22,23] The blue shift at high ClO_4^- concentrations has indicated an increase in the number of water monomers that form hydrogen bonds with ClO_4^- anions.[23] It has been reported that oxygen atoms of the sulfonyl group of Tf_2N^- anions form hydrogen bonds with water molecules.[24] The IR spectra for the concentrated $Zn(Tf_2N)_2$ solutions indicate an increase in the number of water monomer that interacts with Tf_2N^- anions. The enhanced water-anion interactions relate to decrease in the amount of free water. Although the amount of free water certainly decreases in $ZnSO_4$ solutions due to the hydration of Zn^{2+} cations, the amount of free water in $Zn(Tf_2N)_2$ solutions further decreases by not only the hydration but also the water-anion interactions.

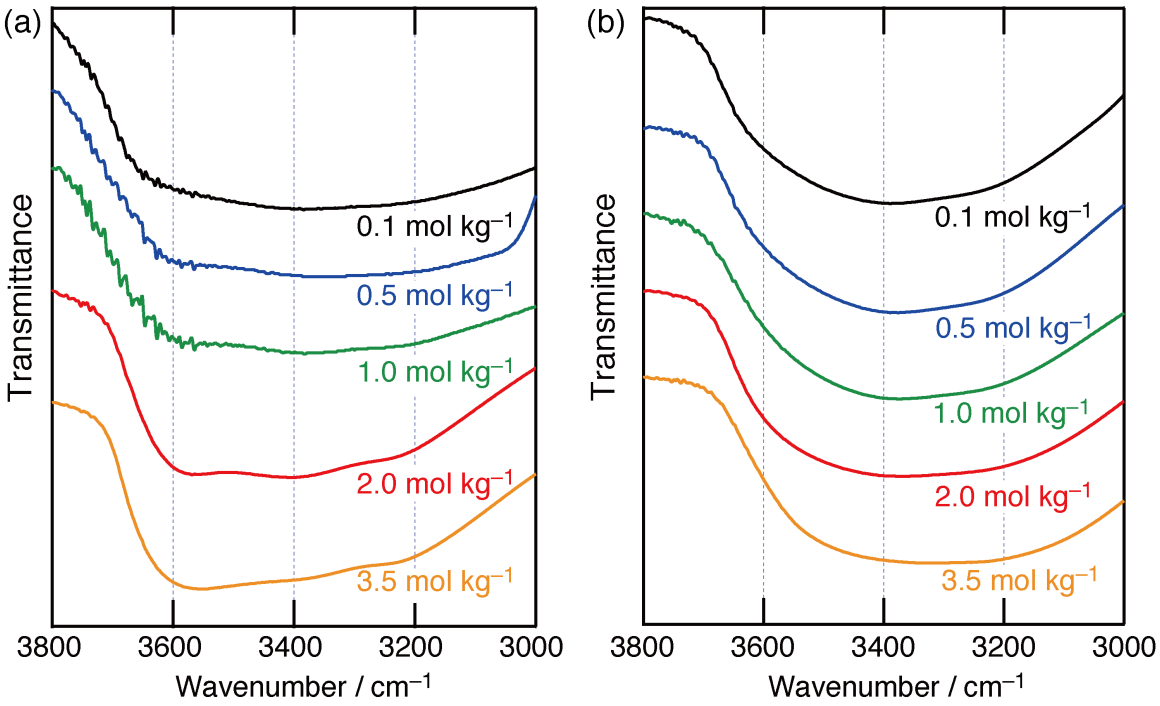

Figure 1.1 IR spectra of O-H stretching vibration modes for (a) $Zn(Tf_2N)_2$ and (b) $ZnSO_4$ solutions.

1.3.2. Raman spectroscopy of aqueous electrolytes.

Figure 1.2 shows the Raman spectra of CF_3 bending vibrations of Tf_2N^- anions for $Zn(Tf_2N)_2$ solutions and a $Zn(Tf_2N)_2$ solid salt. The water content of the solid salt was 5.0 wt%, analyzed by Karl-Fischer titration, which corresponds to the molar ratio $Zn(Tf_2N)_2$:H_2O = 1:1.8. For the solid salt, a shoulder appears at 754 cm^{-1} together with the main peak centered at 747 cm^{-1}. In anhydride solid magnesium bis(trifluoromethylsulfonyl)amide ($Mg(Tf_2N)_2$) a single Raman band has been observed at 754 cm^{-1}, while a single band has been observed at 750 cm^{-1} in its hydrate salts ($Mg(Tf_2N)_2 \cdot 8H_2O$ or $[Mg(H_2O)_6][Tf_2N]_2)(H_2O)_2$). In other words, the hydration of Mg^{2+} cations has resulted in the shift of the wavenumbers of the CF_3 bending vibrations from 754 cm^{-1} to 750 cm^{-1}.[25] The shoulder for the solid salt indicates that $Zn(Tf_2N)_2$ salt with 5.0 wt% H_2O is composed of two phases: anhydride $Zn(Tf_2N)_2$ salt and its hydrate salts.

By contrast, no shoulder peaks are observed for 0.1–3.5 mol kg^{-1}

$Zn(Tf_2N)_2$ solutions, indicating that all Zn^{2+} cations are *not* coordinated with Tf_2N^- anions but hydrated in the 0.1–3.5 mol kg^{-1} solutions. A higher shift for the 3.5 mol kg^{-1} solution indicates the interaction between hydrated Zn^{2+} cations and Tf_2N^- anions, similar to the case of concentrated $LiTf_2N$ aqueous solutions.[5] Namely, the Raman spectra for the solutions indicate that Zn^{2+} cations are hydrated without direct inner-sphere complexations where the high Tf_2N^- concentration causes the outer-sphere interaction with the hydrated cations.

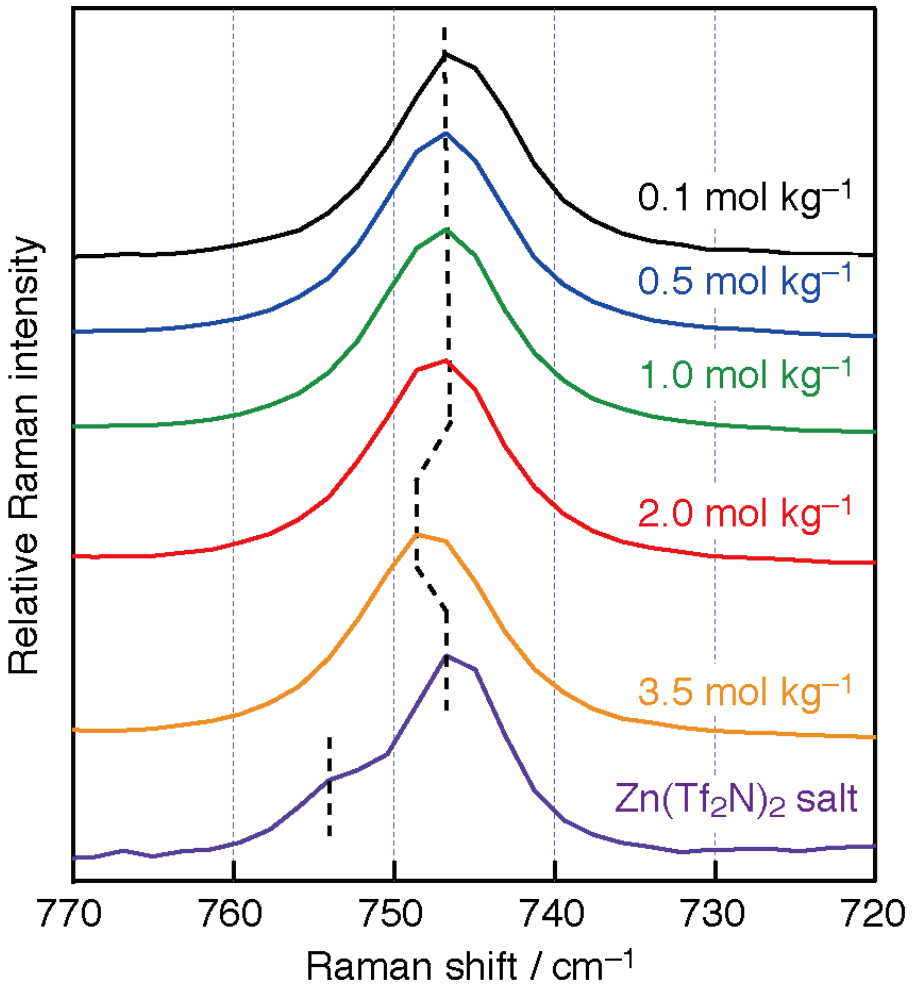

Figure 1.2 Raman spectra between the Raman shift of 770 and 720 cm^{-1} for 1.0, 2.0, 3.5 mol kg^{-1} $Zn(Tf_2N)_2$ solutions and $Zn(Tf_2N)_2$ solid salt.

1.3.3. Open-circuit potentials and prediction of equilibrium potentials.

Table 1.I summarizes the pH values of $Zn(Tf_2N)_2$ and $ZnSO_4$ solutions, showing a slight change with solutes and/or concentrations. Table 1.I also summarizes open-circuit potentials of Zn electrode immersed in $Zn(Tf_2N)_2$ and $ZnSO_4$ solutions. The chemical dissolution of the electrode and hydrogen evolution are not observed during the immersion because $Zn(Tf_2N)_2$ and $ZnSO_4$ solutions are both weak acid with the pH values more than 3. For this reason, the measured potentials *i.e.*, the mixed potentials are very similar to the equilibrium potential of Zn^{2+}/Zn. Compared to the $ZnSO_4$, the measured potentials for the $Zn(Tf_2N)_2$ shift toward positive at the same Zn^{2+} concentration. The equilibrium reaction and the Nernst equation are shown in Eq. (1) and Eq. (2), respectively.

$$Zn(H_2O)_6^{2+} + 2e = Zn + 6H_2O \qquad (1)$$

$$E = E^{\circ} + \frac{RT}{2F} \ln \frac{a_{Zn} a_{H_2O}^{\ 6}}{a_{Zn(H_2O)_6^{2+}}} \qquad (2)$$

where E° and E represent the standard equilibrium potential and the equilibrium potential, respectively, R is gas constant, T is temperature, F is Faraday constant, and a is the activity. As given in Eq. (1), the author assumes that Zn^{2+} cations are hydrated by six water molecules.[26]

Table 1.I also shows the equilibrium potentials predicted from the Nernst equation assuming the activity coefficients of solutes and water to be unity. For the $ZnSO_4$ solutions, the potential values predicted from Eq. (2) are similar to the open-circuit potentials. By contrast, the open-circuit potentials for $Zn(Tf_2N)_2$ solutions are much more positive than the predicted values because of the significant decrease in water activity. In brief, compared to the $ZnSO_4$ solutions, increasing Tf_2N^- concentration with the enhanced water-anion interactions gives a larger activity coefficient of Zn^{2+} cations and/or smaller water activity, proving that the

much decrease in the amount of free water, *i.e.*, loss of free water.

Table 1.I pH, Open circuit potentials of the Zn electrode immersed in $Zn(Tf_2N)_2$ and $ZnSO_4$ solutions, and the equilibrium potential of Zn^{2+}/Zn predicted from the Nernst equation assuming that the activity coefficient of water is 1.

Molality /mol kg^{-1}	pH		Open circuit potential /V vs. SHE		Equilibrium potential (predicted) /V vs. SHE
	$Zn(Tf_2N)_2$	$ZnSO_4$	$Zn(Tf_2N)_2$	$ZnSO_4$	
0.1	5.9	5.8	–0.793	–0.807	–0.793
0.5	5.0	5.5	–0.768	–0.796	–0.772
1.0	4.9	5.1	–0.742	–0.787	–0.763
2.0	4.3	5.3	–0.699	–0.770	–0.754
3.5	3.3	3.9	–0.637	–0.742	–0.747

1.3.4. Linear sweep voltammetry.

Figure 1.3 summarizes linear sweep voltammograms performed on Cu substrate for $Zn(Tf_2N)_2$ and $ZnSO_4$ solutions. Note that the voltammograms are compensated for the ohmic drop between the WE and the RE. In Figure 1.3, the overpotential is converted from V *vs*. Ag/AgCl immersed in 3.0 M NaCl solution to V *vs*. open-circuit potentials of Zn electrode measured in each solution as shown in Table 1.I. Notably, because the measured potentials are very similar to the equilibrium potential of Zn^{2+}/Zn as mentioned above, the horizontal axis of this figure is denoted as 'Potential / V vs. Zn'. In all cases, the limiting current density is more than 100 mA cm^{-2}. The slope of each current–potential curve decreases at a current density of *ca*. 50 mA cm^{-2}. This decrease may be caused by limited

diffusion of hydrated Zn^{2+} cations because hydrogen gas evolution during the cathodic polarization was not detected by eye-inspection. The polarization resistance increases with Zn^{2+} concentration due to enhanced interactions between hydrated Zn^{2+} cation and anion. Compared to the $ZnSO_4$ solutions, the polarization resistance for the $Zn(Tf_2N)_2$ solutions is larger at the same Zn^{2+} concentration. The adsorption of Tf_2N^- anions on Au substrates has been reported.[27] Similarly, Tf_2N^- adsorption will occur on homologous Cu substrate, which may cause the increase in polarization resistance. However, Zn electrodeposition behaviors are affected only by the loss of free water due to concentrating Tf_2N^- anions, not by Tf_2N^- adsorption on the electrode. This is demonstrated and discussed below.

The author also performed cathodic polarization using a Zn^{2+} cation-free $LiTf_2N$ solution with near-neutral pH to investigate Tf_2N^- adsorption on Zn substrate. A platinum rod and Ag/AgCl immersed in 3.0 M NaCl solution were used as CE and RE, respectively. However, no currents specific to Tf_2N^- adsorption on Zn substrate were observed during the polarization.

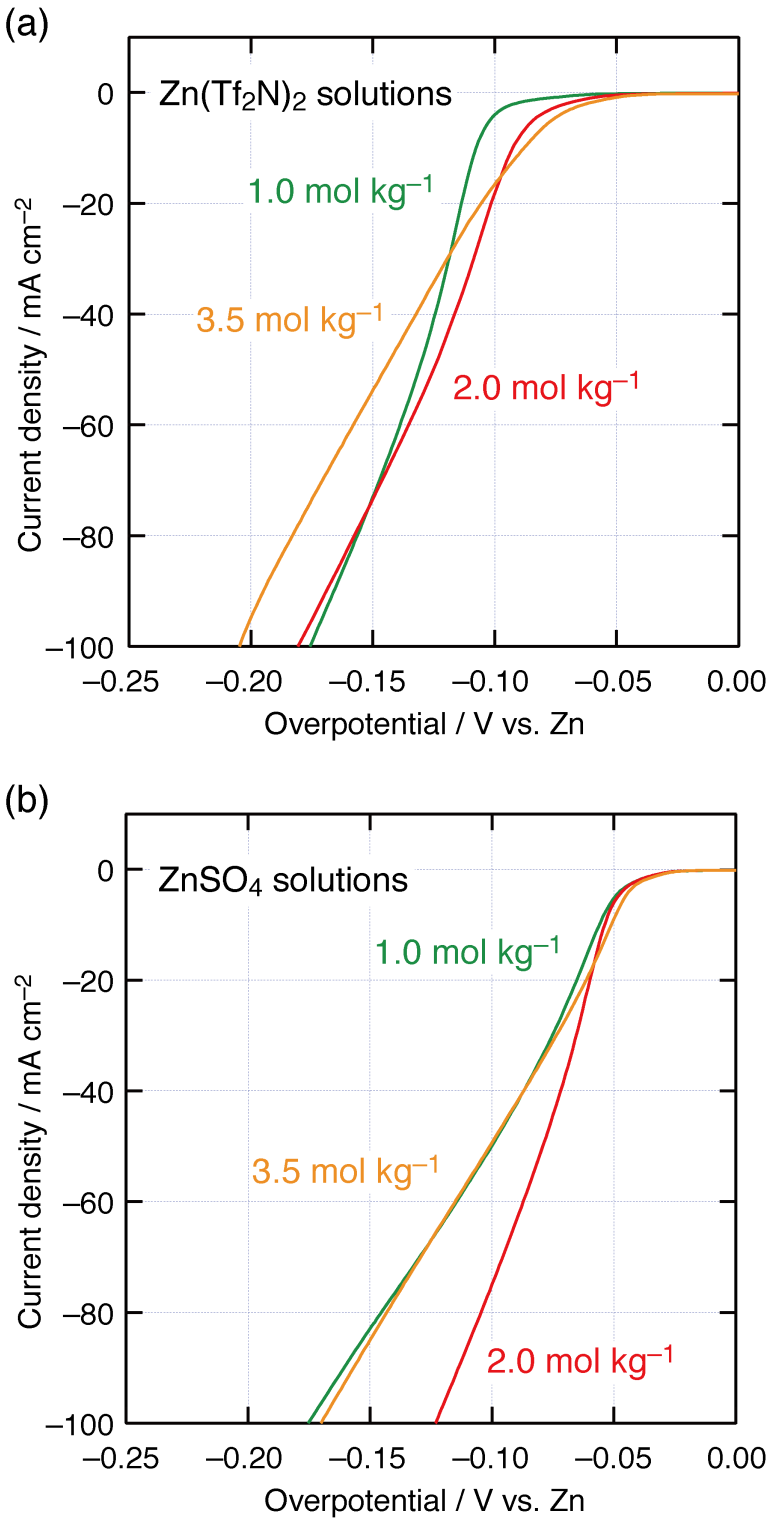

Figure 1.3 Linear sweep voltammograms with ohmic compensation using Cu substrate at a scan rate of 10 mV s^{-1} for (a) $Zn(Tf_2N)_2$ and (b) $ZnSO_4$ solutions.

1.3.5. Electrodeposition from $Zn(Tf_2N)_2$ and $ZnSO_4$ solutions.

Flat and smooth electrodeposits were obtained by the galvanostatic electrolysis at a current density of 50 mA cm^{-2} using $Zn(Tf_2N)_2$ and $ZnSO_4$ solutions. In all cases, the current efficiency was more than 99%, and gas evolution was not detected by eye-inspection. Figure 1.4 shows XRD profiles of metallic Zn deposits obtained from each solution. Electrodeposits with the preferential orientation of hcp basal plane, *i.e.* {001} plane, are obtained from the $Zn(Tf_2N)_2$ solutions, and the degree of preferential orientation increases as the concentration decreases down to 1.0 mol kg^{-1}.

In the case of $ZnSO_4$ solutions, such significant basal-plane orientation is not observed and other diffraction intensities associated with hcp pyramidal and/or prismatic planes increase compared to $Zn(Tf_2N)_2$ solutions. Figure 1.5 displays SEM images of the deposits. The anion dependence of the morphology is also proved by the SEM images. Zn deposits with prismatic planes, which have often been reported in Zn electroplating,[28–30] are obtained from the $ZnSO_4$ solutions, while this is not the case with concentrated $Zn(Tf_2N)_2$ solutions. Zn deposits for $Zn(Tf_2N)_2$ solutions have mossy-like structures. It has been reported that, in the case of zincate baths, mossy-like structures can form on layer-like structures of Zn electrodeposits, *i.e.* on basal planes of Zn.[31,32] Therefore, the fact that mossy-like structures are present only for $Zn(Tf_2N)_2$ solutions proves the preferential orientation of hcp basal plane. The smooth electrodeposits obtained from $ZnCl_2$ hydrate melts have not possessed the preferred orientation of hcp basal planes.[10]

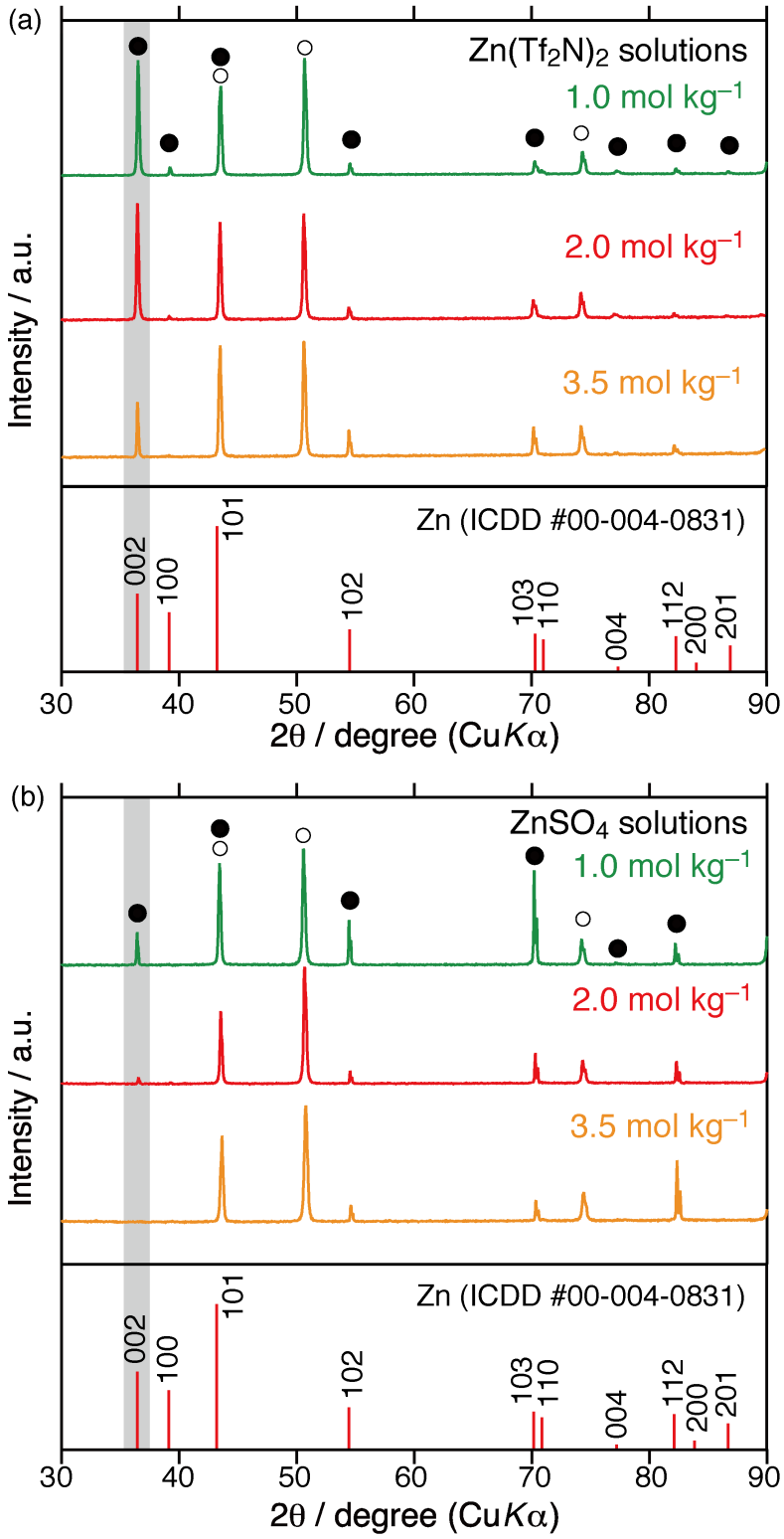

Figure 1.4 XRD profiles of Zn electrodeposits obtained from (a) $Zn(Tf_2N)_2$ and (b) $ZnSO_4$ solutions. Solid circles and open circles indicate Zn electrodeposits and Cu substrate, respectively.

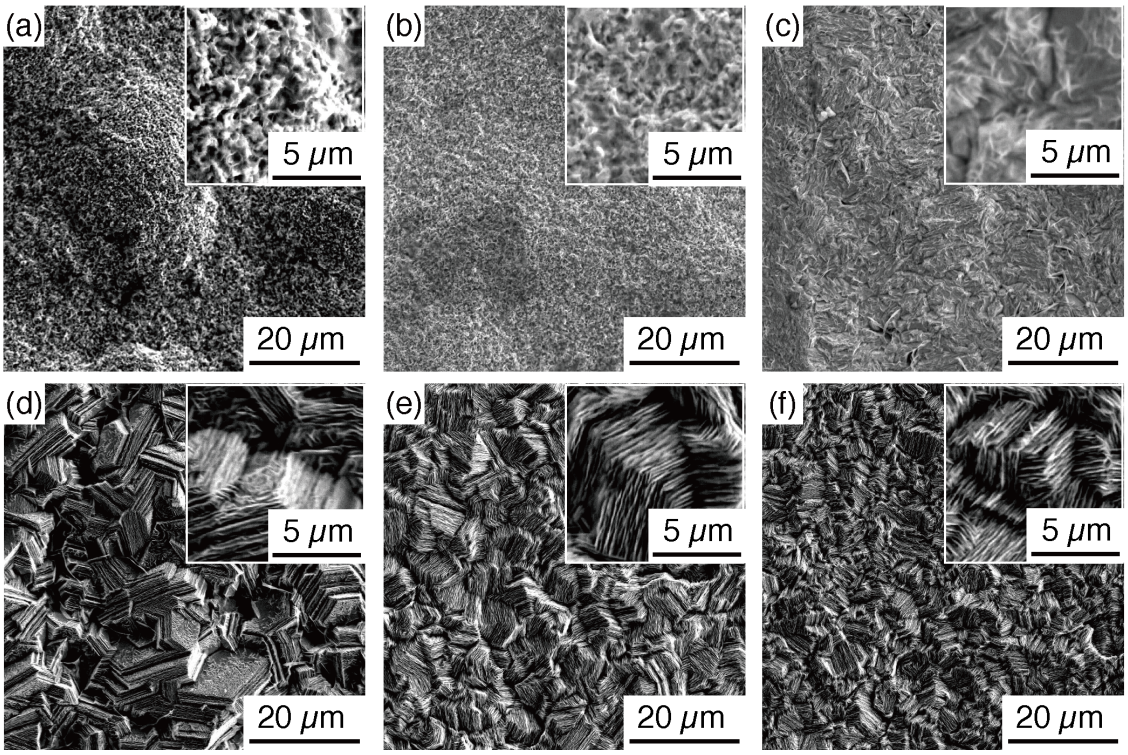

Figure 1.5 SEM images of Zn electrodeposits obtained from (a)–(c) $Zn(Tf_2N)_2$ and (d)–(f) $ZnSO_4$ solutions, with the molality of (a,e) 1.0 mol kg^{-1}, (b,d) 2.0 mol kg^{-1}, and (c,f) 3.5 mol kg^{-1}. Insets show SEM images with higher magnification.

Notably, for 3.5 mol kg^{-1} $Zn(Tf_2N)_2$ solutions, the preferred orientation weakens. The degree of cation-anion dissociation decreases compared to the case of 2.0 mol kg^{-1} as shown by the Raman results. Therefore, the weakened preferential orientation for 3.5 mol kg^{-1} $Zn(Tf_2N)_2$ solutions may well be attributed to the stronger interaction between hydrated Zn^{2+} cations and Tf_2N^- anions. Similarly, an increase in $ZnSO_4$ molality gives a decrease in basal-plane orientation, although the orientation is hardly notable compared to $Zn(Tf_2N)_2$ cases. This is related to an enhanced interaction between hydrated Zn^{2+} cations and SO_4^{2-} anions as $ZnSO_4$ molality increases. The effects of the enhanced interaction between hydrated Zn^{2+} cations and anions on Zn electrodeposition are discussed below. Below the author focuses on 2.0 mol kg^{-1} solutions to identify the

anion effects on Zn electrodeposition.

1.3.6. Identification of the role of Tf_2N^- anions on Zn electrodeposition.

Using mixed $Zn(Tf_2N)_2$-$ZnSO_4$ concentrated aqueous solutions with the total Zn^{2+} concentration of 2.0 mol kg^{-1}, the author also performed the similar experiments of spectroscopy and electrochemistry, to identify the role of Tf_2N^- anions on Zn electrodeposition.

Figure 1.6 shows the IR spectra of O-H stretching vibration for the mixed $Zn(Tf_2N)_2$-$ZnSO_4$ solutions. Adding $Zn(Tf_2N)_2$ salt only slightly breaks hydrogen-bonding networks of water cluster, proving that the amount of free water slightly decreases in the mixed solutions. The pH values listed in Table II depend slightly on x or the molar fraction of $Zn(Tf_2N)_2$ (x = $[Zn(Tf_2N)_2]/\{[Zn(Tf_2N)_2]+[ZnSO_4]\}$). Table II also summarizes open-circuit potentials of the Zn electrode immersed in the mixed solutions. The chemical dissolution of the Zn electrode is not observed during the measurements. Open-circuit potentials gradually shift toward positive with increasing x. Although adding $Zn(Tf_2N)_2$ salt affects the water activity to some extent, these shifts are not significant compared to pure $Zn(Tf_2N)_2$ solutions.

Figure 1.7 summarizes linear sweep voltammograms for the mixed solutions. Note that the voltammograms are compensated for the ohmic drop between the WE and the RE. In Figure 1.7, the overpotential is converted from V *vs*. Ag/AgCl immersed in 3.0 M NaCl solution to V *vs*. open-circuit potentials of Zn electrode measured in each solution as shown in Table II. The increase in the polarization resistance with x indicates a stronger inhibition of the electrodeposition by Tf_2N^- adsorption. However, the slope of the voltammogram polarization resistance for pure $Zn(Tf_2N)_2$ solution, *i.e.* x = 1.00, after the onset of Zn electrodeposition is similar to that for x = 0.20. These results mean that increasing the polarization resistance is attributed to Tf_2N^- adsorption, not to the loss of free water.

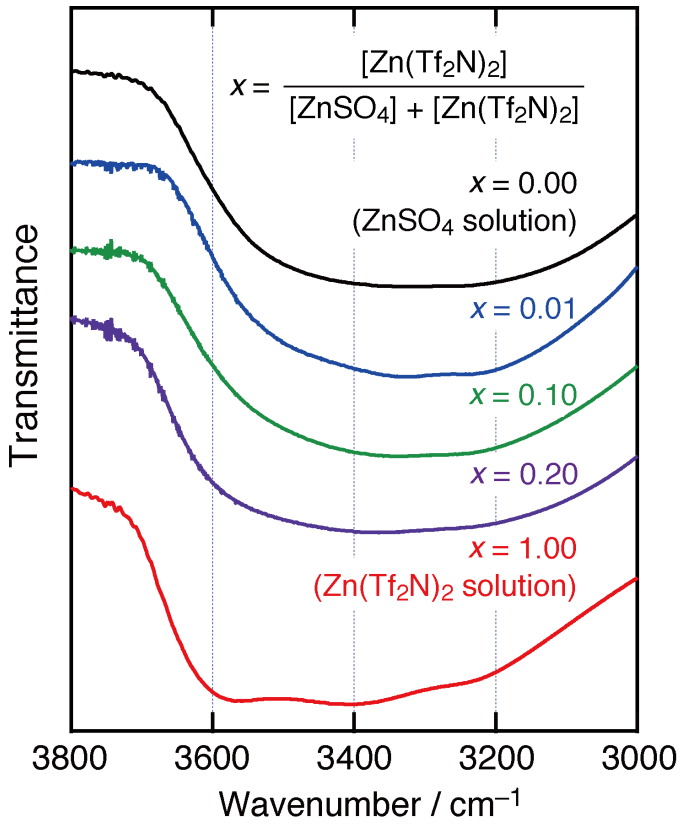

Figure 1.6 IR spectra of O-H stretching vibration modes for $ZnSO_4$-$Zn(Tf_2N)_2$ mixed solutions with $[Zn^{2+}] = 2.0$ mol kg^{-1}.

Table 1.II pH values and open circuit potentials of Zn electrode immersed in the mixed solutions with $[Zn^{2+}] = 2.0$ mol kg^{-1}. x indicates molar fractions of $Zn(Tf_2N)_2$, $x = [Zn(Tf_2N)_2]/\{[Zn(Tf_2N)_2] + [ZnSO_4]\}$ in $ZnSO_4$-$Zn(Tf_2N)_2$ mixed solutions at total Zn^{2+} molality of 2.0 mol kg^{-1}.

x	pH	Open circuit potential / V vs. SHE
0.00	5.3	–0.770
0.01	4.9	–0.761
0.10	5.1	–0.756
0.20	5.0	–0.745
1.00	4.3	–0.699

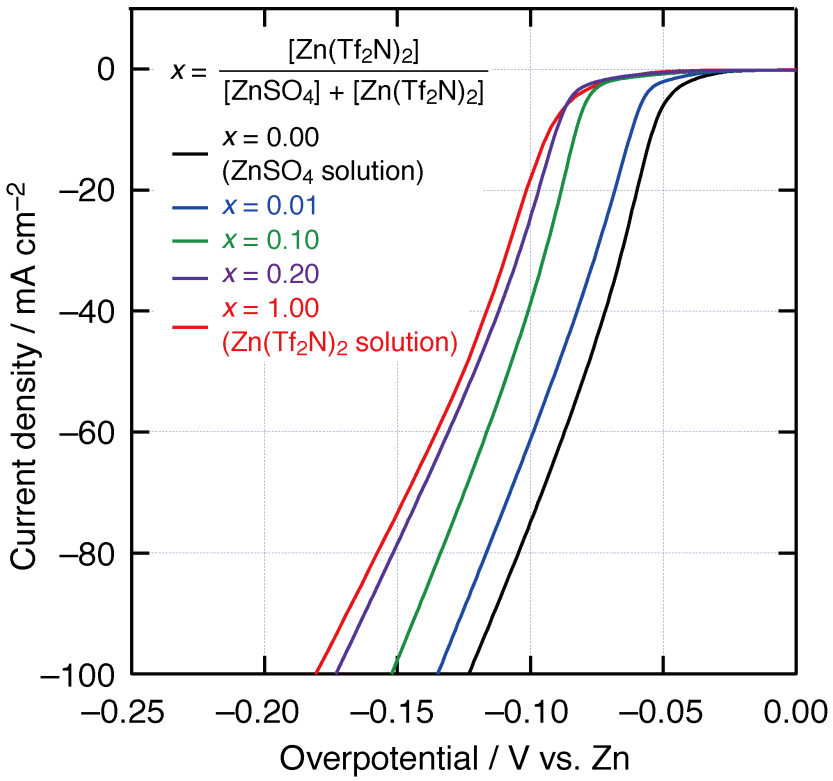

Figure 1.7 Linear sweep voltammograms with ohmic compensation using Cu substrates at a scan rate of 10 mV s^{-1} for the mixed solutions with $[Zn^{2+}] = 2.0$ mol kg^{-1}.

For the mixed solutions, electrodeposits obtained by galvanostatic electrolysis at a current density of 50 mA cm^{-2} showed flat and smooth appearance. The current efficiency was more than 99%, and gas evolution was not observed by eye-inspection. Figure 1.8 shows XRD profiles of the single-phase Zn electrodeposits obtained from the mixed solutions. Basal-plane oriented deposits are *not* obtained from the mixed solutions as in the case of 2.0 mol kg^{-1} $ZnSO_4$ solution. SEM images shown in Figure 1.9 also prove that the addition of $Zn(Tf_2N)_2$ salt has almost no effect on the morphologies of Zn electrodeposits.

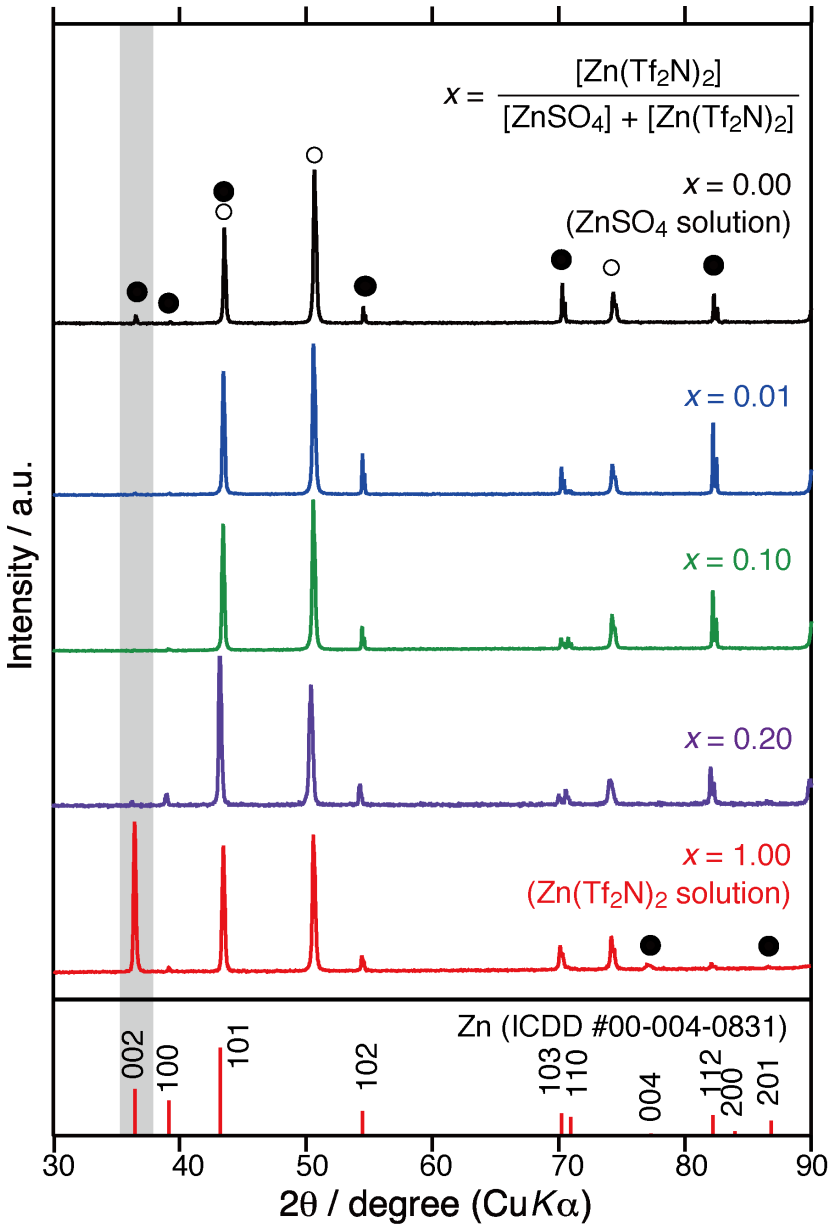

Figure 1.8 XRD profiles of Zn electrodeposits obtained from mixed solutions with $[Zn^{2+}] = 2.0$ mol kg^{-1}. Solid circles and open circles indicate Zn electrodeposits and Cu substrates, respectively.

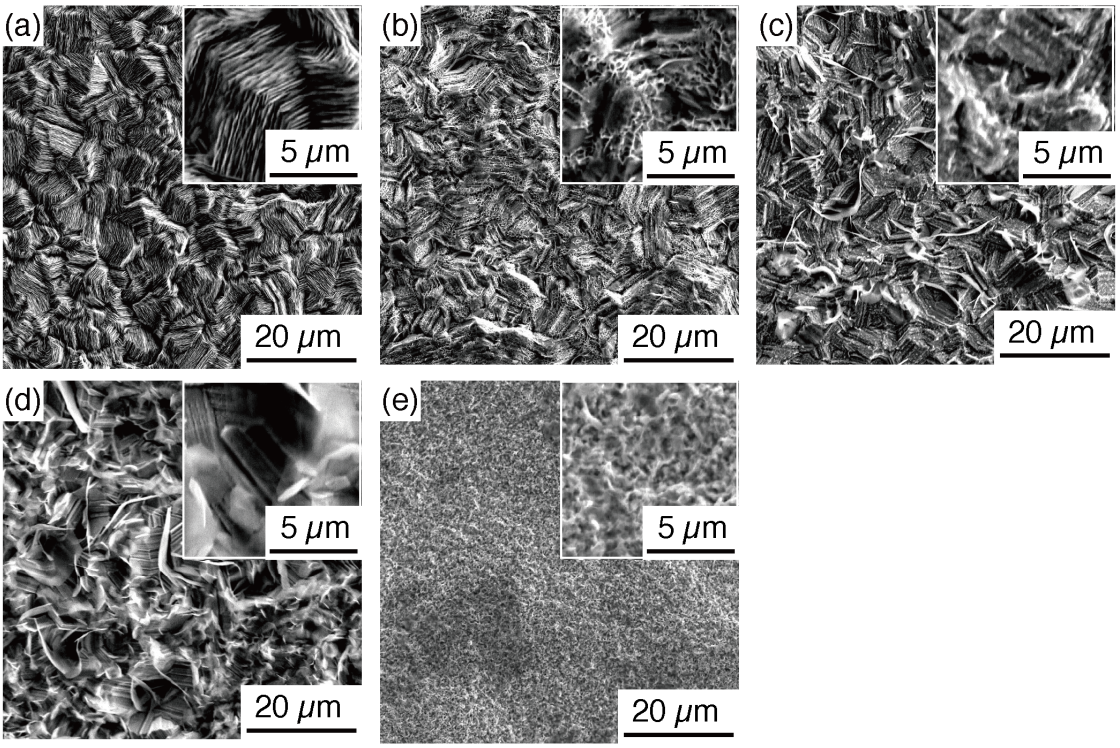

Figure 1.9 SEM images of Zn electrodeposits obtained from the mixed solutions with $[Zn^{2+}]$ = 2.0 mol kg^{-1}; x = (a) 0.00, (b) 0.01, (c) 0.10, (d) 0.20, and (e) 1.00. Insets show SEM images with higher magnification.

These results indicate that the only presence of Tf_2N^- anions does not give the preferred orientation of hcp basal planes, although the Tf_2N^- adsorption that increases the polarization resistances occurs. Therefore, the preferred orientation is derived from the loss of free water due to water-anion interactions, not Tf_2N^- adsorption.

1.3.7. Comparison with conventional trends on Zn electrodeposition.

Surface morphologies of metal electrodeposits obtained from aqueous systems have been conventionally controlled by current density, cathodic overpotential, the composition of aqueous electrolytes, and additives.[28–30,33–42] The effect of the loss of free water on the morphologies is discussed in comparison to the conventional trends.

Current density and/or cathodic overpotentials have been reported to

vary the preferred orientations.[29,30,41,42] Especially in Zn electrodeposition, with increasing the overpotential due to the use of additives and/or the increase in current density, the preferred orientation of hcp basal planes weakens. However, the results of this study differ from this trend. The use of $Zn(Tf_2N)_2$ solutions enhances the preferred orientation of basal planes despite the increased overpotential (see Figure 1.4).

Systematic studies exist on the effects of solute concentration, additives, and complexations of metal ions on the microstructure of electrodeposits. As illustrated in Figure 1.10,[33–35] five main microstructures have been proposed: field-oriented isolated crystals (FI), basis-orientated reproduction (BR), twining intermediate (Z), field orientated texture (FT), and unoriented dispersion (UD). Inhibition intensity means the difficulty of the electrodeposition reactions due to the use of additives or the complexation of ions. Particularly, in the presence of the complexation, the inhibition intensity increases because the strong interaction between metal cations and ligands prevents the discharge of the complexed ions.

In the conventional trends, the increased inhibition intensity leads to UD. The microstructures for $ZnSO_4$ solutions and the mixed solutions are classified as UD because preferred orientations and epitaxial growth are not observed. For concentrated $Zn(Tf_2N)_2$ solutions, by contrast, the microstructure is classified as FT. To consider whether the loss of free water suppresses the electrodeposition, the change in the microstructure is compared to the growth types shown in Figure 1.10, which corresponds to a decrease in the inhibition intensity. This is *not* the case with the use of additives, adsorption of anions and/or the complexation of metal ions. Consequently, the electrodeposition behaviors in the case of loss of free water differ from these conventional trends.

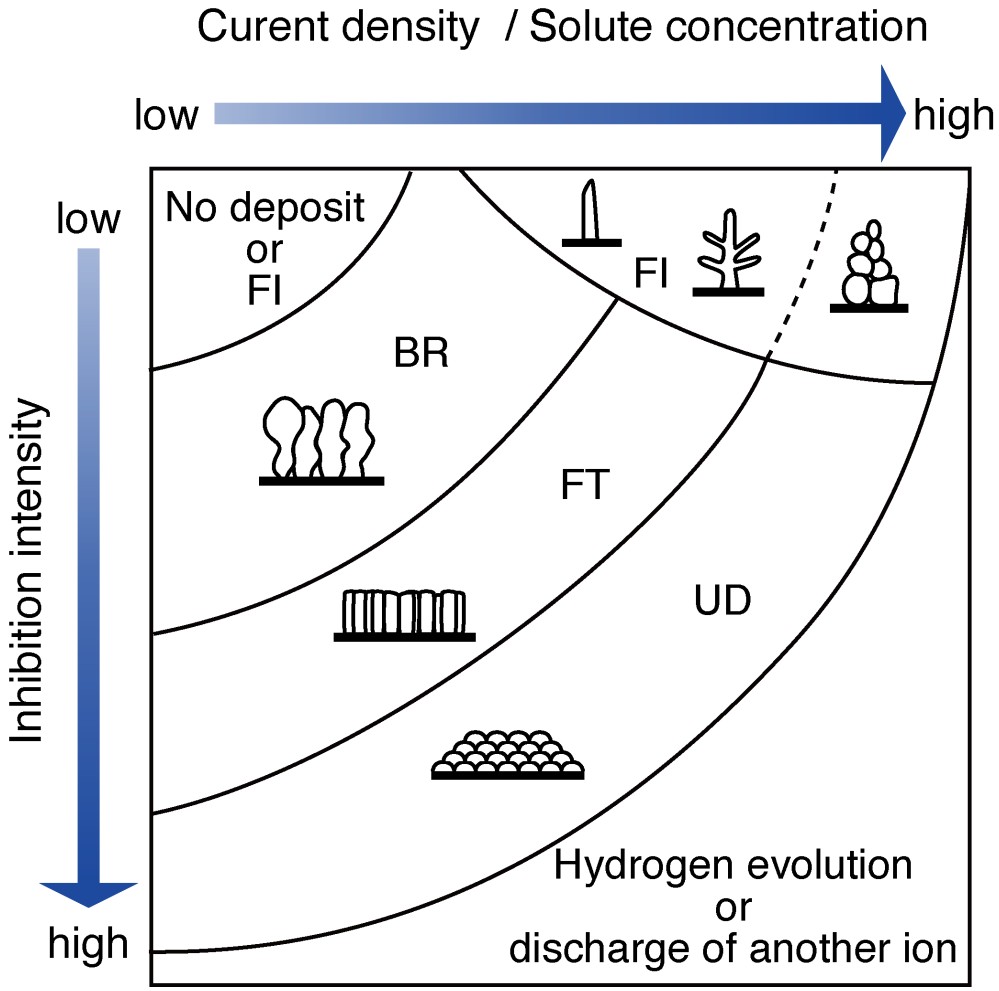

Figure 1.10 Illustration of an accepted correlation between microstructure of electrodeposits and conditions, such as current density, solute concentration, and inhibition intensity in conventional aqueous solutions.[33–35]

Notably, in the $Zn(Tf_2N)_2$ and $ZnSO_4$ cases, the enhanced interaction between hydrated Zn^{2+} and anions with increasing solute concentration gives rise to a decrease in the basal-plane orientation as shown in Figure 1.4. The decrease in the basal-plane orientation due to the enhanced interaction is related to these conventional trends.[33–35] Similarly to the complexation of ions, the enhanced interactions can inhibit the discharge, although this inhibition is weaker than that in the presence of complexation.

In brief, the increase in $Zn(Tf_2N)_2$ or $ZnSO_4$ molality can increase the inhibition intensity and change gradually from the microstructure classified as FT to that as UD. For this reason, increasing $Zn(Tf_2N)_2$ concentration to 3.5 mol kg^{-1} weakens basal-plane orientation as shown in Figure 1.4(a). Similarly, the $ZnSO_4$ molality gives rise to decrease basal-plane orientation as shown in Figure 1.4(b), and make smaller the grain size of Zn crystals as shown in Figure 1.5.

1.3.8. Effect of loss of free water on Zn electrodeposition.

As mentioned in the Introduction, Zn electrodeposition competes with hydrogen adsorption and/or evolution during cathodic reactions due to the relatively negative electrode potential of Zn. Several investigations have reported that the discharge of Zn^{2+} cations is a two-step reaction involving the formation of intermediate Zn^{+} adions and adsorbed hydrogen atoms inhibit the discharge.[43–45] Adsorbed hydrogen has also been suggested to adsorb on active sites for the electrodeposition, such as kink sites.[45] For these reasons, the number of adsorbed hydrogen can affect the nucleation and growth of Zn crystals.

A decrease in the amount of free water by increasing concentrations has been reported to suppress hydrogen evolution due to proton reduction.[14,16] Similarly, hydrogen adsorption due to proton reduction, as well as the hydrogen evolution, can be suppressed in $Zn(Tf_2N)_2$ solutions with a loss of free water compared to $ZnSO_4$ solutions. Besides, the positive shift in open-circuit potentials in $Zn(Tf_2N)_2$ solutions compared to $ZnSO_4$ solutions (see Table 1.I and 1.II) can decrease contributions of hydrogen evolution/adsorption to competing Zn electrodeposition. For these reasons, the number of adsorbed hydrogen atoms will decrease in the concentrated $Zn(Tf_2N)_2$ solutions much more than in the concentrated $ZnSO_4$ solutions despite the similar pH values. Notably, even in the $ZnSO_4$ solutions, the number of adsorbed hydrogens is inherently small due to the low strength of the Zn-H bond.[46]

Because the adsorbed hydrogen inhibits surface diffusion of the adions, newly Zn nuclei can be easily generated before the adions diffuse to already existing Zn crystals. Also, hydrogen adsorption on the active sites can inhibit incorporating the adions into the Zn crystals, *i.e.*, the growth of Zn crystals. In other words, the decreased number of adsorbed hydrogen can promote surface diffusion of Zn^{+} adions and the growth of Zn crystals. Since the interfacial free energy of basal planes of hcp structure is the lowest, the expansion of basal planes is advantageous for decreasing the interfacial free energy of electrodeposits. For this reason, basal-plane oriented crystals are more geometrically advantageous for the horizontal growth of the electrode than those oriented to other planes.

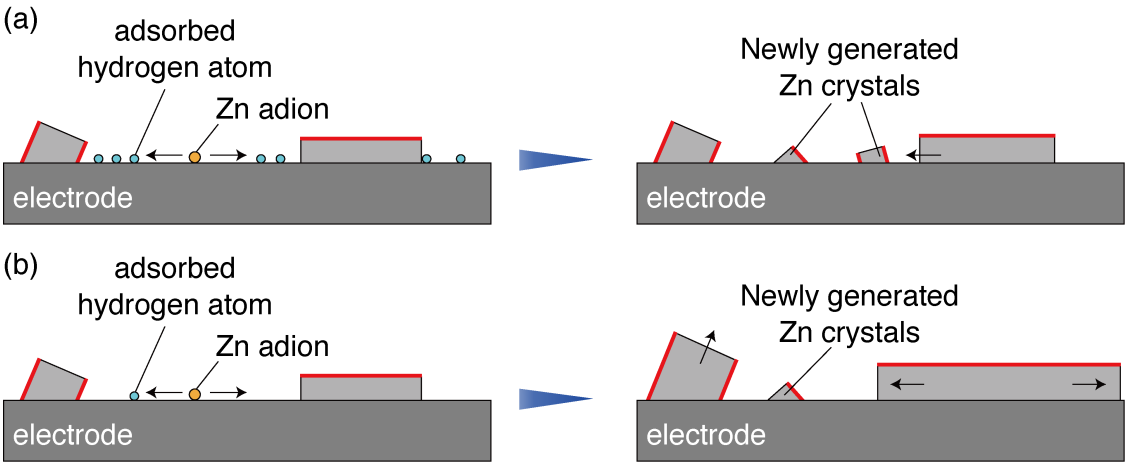

Figure 1.11 Schematic illustrations of nucleation and/or growth of Zn crystals when the amount of adsorbed hydrogen atoms is (a) large and (b) small. Red lines represent hcp basal planes.

Figure 1.11 shows schematic images of the effects of hydrogen adsorption on nucleation and/or growth of Zn crystals. In the case of a large amount of adsorbed hydrogen atoms, surface diffusion of Zn^{+} adions and Zn growth will be inhibited by adsorbed hydrogens (see Figure 1.11(a)). For this reason, the horizontal growth of basal-plane oriented crystals will be disadvantageous. By contrast, in the case of few adsorbed hydrogen

atoms, there is little geometrical limitation for horizontal growth of basal-plane oriented crystals (see Figure 1.11(b)). Therefore, this easier growth by removing the geometrical limitation can lead to the preferred orientation of basal planes. In other words, by the use of Tf_2N^- anions free water is lost and hydrogen adsorption is suppressed, resulting in the change in Zn electrodeposition behaviors.

The use of concentrated aqueous systems with the suppression of hydrogen adsorption could simplify various industrial processes. One is a baking treatment performed after Zn electroplating on steels. The baking treatment is necessary to remove residual hydrogen atoms in the substrates because this residue causes hydrogen embrittlement and degrades the mechanical properties of the substrates.[47,48] There is a possibility that the use of concentrated aqueous systems decreases the risk of hydrogen embrittlement. The author intends to explore this possibility in future studies because the role of reducing the hydrogen adsorption on the mechanical property of Zn electroplated steels is also of interest.

1.4. Conclusions

The effect of loss of free water on Zn electrodeposition behaviors by the use of concentrated $Zn(Tf_2N)_2$ and $ZnSO_4$ aqueous solutions was investigated. Increasing Tf_2N^- concentration enhanced water-anion interactions, giving the breakdown of the hydrogen-bonding networks of water clusters and the loss of free water in stark contrast to the case of $ZnSO_4$ solutions. Hcp basal-plane oriented electrodeposits were obtained only from concentrated $Zn(Tf_2N)_2$ solutions. The use of mixed $Zn(Tf_2N)_2$-$ZnSO_4$ solutions proved that the loss of free water, not Tf_2N^- adsorption, changes the electrodeposition behavior. This change differs from conventional trends of metal electrodeposition using conventional aqueous systems. The loss of free water suppresses hydrogen adsorption on

the electrode, giving that surface diffusion of Zn^+ adions and growth of Zn crystals promote. The promotions and the easier growth of Zn basal planes with the lowest interfacial free energy induce the basal-plane oriented electrodeposits.

The use of concentrated aqueous solutions can improve not only the stability of aqueous electrolytes in electrochemical devices but also the current electrodeposition processes due to the suppression of hydrogen adsorption. The author is confident that this viewpoint will contribute to a deeper understanding of the electrodeposition behaviors of various metals and the improvements of the surface properties of electrodeposits using concentrated aqueous systems.

References

1. C. A. Angell, *J. Electrochem. Soc.*, **112**, 1224 (1965).
2. C. T. Moynihan, C. R. Smalley, C. A. Angell, and E. J. Sare, *J. Phys. Chem.*, **73**, 2287 (1969).
3. C. A. Angell and J. C. Tucker, *J. Phys. Chem.*, **78**, 278 (1974).
4. S. Deki, M. Ohtawa, and Y. Kanaji, *J. Chem. Soc. Jpn.* (in Japanese), **12**, 1623 (1979). [DOI: 10.1246/nikkashi.1979.1623]
5. L. Suo, O. Borodin, T. Gao, M. Olguin, J. Ho, X. Fan, C. Luo, C. Wang, and K. Xu, *Science*, **350**, 938 (2015).
6. Y. Yamada, K. Usui, K. Sodeyama, S. Ko, Y. Tateyama, and A. Yamada, *Nat. Energy*, **1**, 1 (2016).
7. P. Lannelongue, R. Bouchal, E. Mourad, C. Bodin, M. Olarte, S. le Vot, F. Favier, and O. Fontaine, *J. Electrochem. Soc.*, **165**, A657 (2018).
8. W. Deng, X. Wang, C. Liu, C. Li, J. Chen, N. Zhu, R. Li, and M. Xue, *Energy Storage Mater.*, **20**, 373 (2019).
9. F. Wang, O. Borodin, T. Gao, X. Fan, W. Sun, F. Han, A. Faraone, J.

A. Dura, K. Xu, and C. Wang, *Nat. Mater.*, **17**, 543 (2018).
10. C. Y. Chen, K. Matsumoto, K. Kubota, R. Hagiwara, and Q. Xu, *Adv. Energy Mater.*, **9**, 1 (2019).
11. N. Zhang, F. Cheng, Y. Liu, Q. Zhao, K. Lei, C. Chen, X. Liu, and J. Chen, *J. Am. Chem. Soc.*, **138**, 12894 (2016).
12. A. Kitada, M. Kurihara, R. Takai, K. Fukami, and K. Murase, *J. Surf. Finish. Soc. Jpn.*, **71**, 376 (2020). [DOI: 10.4139/sfj.71.376]
13. K. Adachi, A. Kitada, K. Fukami, and K. Murase, *J. Electrochem. Soc.*, **166**, D409 (2019).
14. K. Adachi, A. Kitada, K. Fukami, and K. Murase, *Electrochim. Acta*, **338**, 135873 (2020).
15. Q. Huang and Y. Hu, *J. Electrochem. Soc.*, **165**, D796 (2018).
16. S. De, J. White, T. Brusuelas, C. Patton, A. Koh, and Q. Huang, *Electrochim. Acta*, **338,** 135852 (2020).
17. S. Peulon and D. Lincot, *J. Electrochem. Soc.*, **145**, 864 (1998).
18. T. Yoshida, D. Komatsu, N. Shimokawa, and H. Minoura, *Thin Solid Films*, **451**–**452**, 166 (2004).
19. M. Izaki and T. Omi, *J. Electrochem. Soc.*, **144**, L3 (2019).
20. E. A. Ambundo, M. Deydier, A. J. Grall, N. Aguera-Vega, L. T. Dressel, T. H. Cooper, M. J. Heeg, L. A. Ochrymowycz, and D. B. Rorabacher, *Inorg. Chem.*, **38**, 4233 (1999).
21. Z. Wei, Y. Zhang, L. Zhao, J. Liu, and X. Li, *J. Phys. Chem. A*, **109**, 1337 (2005).
22. A. W. Omta, M. F. Kropman, S. Woutersen, and H. J. Bakker, *J. Chem. Phys.*, **119**, 12457 (2003).
23. Y. Chen, Y. Zhang, and L. Zhao, *Phys. Chem. Chem. Phys.*, **6**, 537 (2004).
24. J. K. Clark, S. J. Paddison, M. Eikerling, M. Dupuis, and T. A. Zawodzinski, *J. Phys. Chem. A*, **116**, 1801 (2012).
25. G. Veryasov, U. Harinaga, K. Matsumoto, and R. Hagiwara, *Eur. J. Inorg. Chem.*, **2017**, 1087 (2017).

26. H. Ohtaki, T. Yamaguchi, and M. Maeda, *Bull. Chem. Soc. Jpn.*, **49**, 701 (1976).
27. L. Coustan, G. Shul, and D. Bélanger, *Electrochem. commun.*, **77**, 89 (2017).
28. K. O. Nayana and T. V. Venkatesha, *J. Electroanal. Chem.*, **663**, 98 (2011).
29. K. Raeissi, A. Saatchi, and M. A. Golozar, *J. Appl. Electrochem.*, **33**, 635 (2003).
30. K. M. Youssef, C. C. Koch, and P. S. Fedkiw, *Electrochim. Acta*, **54**, 677 (2008).
31. T. Mitsuhashi, Y. Ito, Y. Takeuchi, S. Harada, and T. Ujihara, *Thin Solid Films*, **590**, 207 (2015).
32. T. Otani, M. Nagata, Y. Fukunaka, and T. Homma, *Electrochim. Acta*, **206**, 366 (2016).
33. R. Winand, *Mod. Electroplat. Fifth Ed.*,Wiley, New York, 285 (2011).
34. R. Winand, *Hydrometallurgy*, **29**, 567 (1992).
35. R. Winand, *Electrochim. Acta*, **39**, 1091(1994).
36. L. Oniciu and L. Mureşan, *J. Appl. Electrochem.*, **21**, 565 (1991).
37. M. C. Li, L. L. Jiang, W. Q. Zhang, Y. H. Qian, S. Z. Luo, and J. N. Shen, *J. Solid State Electrochem.*, **11**, 549 (2007).
38. A. Gomes and M. I. da S. Pereira, *Electrochim. Acta*, **51**, 1342 (2006).
39. M. Mouanga, L. Ricq, J. Douglade, and P. Berçot, *J. Appl. Electrochem.*, **37**, 283 (2007).
40. M. Mouanga, L. Ricq, G. Douglade, J. Douglade, and P. Berçot, *Surf. Coat. Technol.*, **201**, 762 (2006).
41. J. F. S. Filho and V. F. C. Lins, *Surf. Coat. Technol.*, **200**, 2892 (2006).
42. N. A. Pangarov, *J. Electroanal. Chem.*, **9**, 70 (1965).
43. C. Cachet and R. Wiart, *J. Electrochem. Soc.*, **141**, 131 (1994).
44. F. Ganne, C. Cachet, G. Maurin, R. Wiart, E. Chauveau, and J. Petitjean, *J. Appl. Electrochem.*, **30**, 665 (2000).

45. R. Ichino, C. Cachet, and R. Wiart, *Electrochim. Acta*, **41**, 1031 (1996).
46. S. Trasatti, *J. Electroanal. Chem.*, **39**, 163 (1972).
47. K. R. Sriraman, S. Brahimi, J. A. Szpunar, and S. Yue, *J. Appl. Electrochem.*, **43**, 441 (2013).
48. E. M. K. Hillier and M. J. Robinson, *Corros. Sci.*, **46**, 715 (2004).

Chapter 2

Hydrogen adsorption and desorption on a platinum electrode in acidic aqueous solutions containing lithium salts with extremely high concentrations

2.1. Introduction

Concentrated aqueous systems are powerful tools for electrochemical processes because an increased solute concentration decreases the amount of uncoordinated water, which is the so-called free water, suppressing water decomposition. Since the expansion of the potential window to *ca*. 3.0 V has been reported for a 21 mol kg^{-1} lithium bis(trifluoromethylsulfonyl)amide ($LiTf_2N$, Tf = SO_2CF_3) aqueous solution,[1] several studies have attempted to apply concentrated systems to various electrochemical processes, such as energy storage and surface finishing.[2–21] Some studies on solutes with a high solubility have found that certain compositions decrease the amount of water as solvents, further expanding the potential window.[2–6]

Concentrated solutions with added metal ions as the source of metallic elements have also been used for metal electrodeposition that competes with hydrogen evolution reactions (HER) and hydrogen adsorption.[14–16] Chrome (Cr) plating with a high current efficiency has been demonstrated using concentrated lithium chloride (LiCl) solutions containing Cr^{3+} salt with a strong acidity.[15] The reduction of proton species (H^+ or H_3O^+) and copper deposition in acidic aqueous solutions with high LiCl concentration have also been investigated.[16] Proton reduction is kinetically suppressed because the lack of free water causes slow diffusion and a tight supply of protons to the electrodes.

Although increasing the concentrations certainly suppresses proton reduction, the understanding of HER in concentrated systems is behind that in conventional systems, *i.e.*, relatively diluted aqueous solutions with high water content. In such conventional solutions, the mechanism of HER is discussed mainly using platinum (Pt) electrodes with a low overpotential for HER using acidic or alkaline aqueous solutions. These discussions tend to focus on underpotential deposited hydrogen (H_{upd}) that adsorbs and desorbs on the Pt surface at a positive potential compared to the equilibrium potential of H^+/H_2.[22–33] Note that H_{upd} is strongly bonded on Pt atoms and differs from hydrogen intermediates involving HER.[24–26] In addition, recent electrochemical measurements have focused on HER and hydrogen oxidation reactions (HOR) in not only acidic and alkaline cases but also neutral and near-neutral conditions.[34–41] In weakly acidic conditions, a two-step cathodic current related to HER appears during cathodic polarizations because the reactants switch from protons to water due to the tight proton supply to the electrodes.[34–36] A similar anodic current related to HOR appears in weakly alkaline conditions due to switching reactants from OH^- to water.

Since the conditions of solute addition such as their concentrations and compositions can affect the pH of concentrated aqueous electrolyte solutions, understanding the detailed behaviors such as H_{upd} adsorption and desorption and reactants switching in HER and HOR is essential to apply these systems to a broad range of electrochemical processes. Herein the author investigates the behaviors of proton reduction and H_{upd} adsorption and desorption on a polycrystalline Pt (poly-Pt) electrode in acidic aqueous solutions at various lithium salt concentrations.

The author also examines the effects of counter anion species of the lithium salt on water molecules. Some anion species have been reported to affect the behavior of water molecules such as the formation or breakdown of hydrogen-bonding network among water molecules.[2,17,42,43] Since an increase in solute concentration enhances such effects, electrochemical

reactions associated with water may depend on the anion species in the concentrated systems. Monovalent anions whose electrochemical reactions would not occur in the HER/HOR potential region are selected. It has been reported, for example, that nitrate (NO_3^-) anions are electrochemically reduced into nitrite (NO_2^-) anions on the Pt cathode in the region.[44,45] Consequently, this study avoids using NO_3^- anions because employing a system with side reactions is not well suited to investigate the effects of the solute concentration and anion species. In this study, electrochemical and spectroscopic measurements are conducted using aqueous solutions of lithium salts with three different anions: $LiTf_2N$, LiCl, and lithium perchlorate ($LiClO_4$), at various concentrations.

2.2. Experimental

Solutions. $LiTf_2N$, LiCl, and $LiClO_4$ were purchased from Nacalai Tesque, Kishida Kagaku, and Fujifilm Wako, respectively. These salts were used as received. They were dissolved in ultra-pure water (18.2 MΩ cm, Millipore, Milli-Q Reference A+). Table 2.I shows the prepared solutions with various molar concentrations (*i.e.*, molarities). A solution of 1.0, 3.0, 4.4, and 5.0 M for $LiTf_2N$, 1.0, 5.0, and 10.0 M (= mol dm^{-3}) for LiCl, and 1.0 and 4.5 M for $LiClO_4$ were prepared. Among them, 5.0 M $LiTf_2N$, 10.0 M LiCl, and 4.5 M $LiClO_4$ were nearly saturated solutions. The molality of 4.4 M $LiTf_2N$ and 10.0 M LiCl solutions corresponded to 12.6 mol kg^{-1} (*i.e.*, the molar ratio of water molecules to lithium salts, *n*, is the same). Similarly, 3.0 M $LiTf_2N$, 5.0 M LiCl, and 4.5 M $LiClO_4$ solutions corresponded to *ca*. 5.5 mol kg^{-1}.

For the pH measurements, a pH meter (HORIBA, Laquaact D-71) with an ion-sensitive effect transistor (ISFET) pH electrode (HORIBA, 0030-10D) was used. The pH was adjusted to 2.0 or 3.0 by adding small amounts of 1.0 M bis(trifluoromethylsulfonyl)imide (HTf_2N), hydrochloric

acid (HCl), or perchloric acid ($HClO_4$) solution to the $LiTf_2N$, LiCl, or $LiClO_4$ solution, respectively.

Table 2.I Properties of the sample aqueous solutions.

Electrolyte	Molarity / M	Density / g cm^{-3}	Molality / mol kg^{-1}	$n = H_2O$/lithium salt (molar ratio)
$LiTf_2N$	1.0	1.14	1.2	47.6
	3.0	1.41	5.5	10.2
	4.4	1.61	12.6	4.4
	5.0	1.66	22.3	2.5
LiCl	1.0	1.03	1.0	54.8
	5.0	1.11	5.6	9.9
	10.0	1.22	12.6	4.4
$LiClO_4$	1.0	1.06	1.1	53.0
	4.5	1.28	5.6	9.9

Electrochemical cell. Electrochemical measurements were conducted at 22 ± 1 °C using a potentiostat (Bio-Logic Science Instruments, SP-300) by the three-electrode method. The working electrode (WE) and counter electrode (CE) were a poly-Pt sheet and Pt rod, respectively. The reference electrode (RE) was an Ag/AgCl electrode immersed in a 3.0 M sodium chloride (NaCl) aqueous solution. The author used a double-junction RE (HORIBA, 2565A-10T) to prevent Cl^- contamination of the sample aqueous solution. The outer part of the RE was also filled with the sample solution. NaCl was used instead of potassium chloride (KCl) to avoid precipitation of less-soluble potassium bis(trifluoromethylsulfonyl)amide (KTf_2N) or potassium perchlorate ($KClO_4$) at the internal liquid junction. The potential of the RE was 0.226 ± 0.004 V vs. SHE.[46] The liquid junction potential in

the RE due to the difference of ionic mobility between Na^+ and Cl^- was calculated from Henderson's equation, and was below 15 mV. Before the electrochemical measurements, the Pt plate was mechanically polished with 0.3 μm alumina, rinsed with ultra-pure water, ultrasonically cleaned by acetone and ultra-pure water for 10 min, respectively. Finally, it was placed in a boiling mixture of HNO_3/H_2O_2 (60% HNO_3:30%H_2O_2:H_2O = 1:1:4 by volume) for 20 min.

Electrochemical and spectroscopic measurements. To verify the quality of the Pt surface, cyclic voltammetry was conducted on the Pt WE in a 0.5 M H_2SO_4 from –0.22 to 1.40 V vs. RE at a scan rate of 100 mV sec^{-1} before cyclic voltammetry using each lithium salt solution. This voltammetry was repeated until the voltammogram that indicates that the poly-Pt surface was completely clean and of suitable quality.[26,27] Afterwards, the electrochemical cell and electrodes were carefully rinsed with ultra-pure water and the appropriate sample solution because residual H_2SO_4 affects the pH of the sample solutions. Cyclic voltammetry using the lithium salt solutions were conducted at a scan rate of 100 mV sec^{-1} to detect H_{upd} adsorbed on the Pt WE.

Infrared spectroscopy (IR) was also conducted using a JASCO FT/IR–460 plus system with silicon window materials to evaluate the hydrogen-bonding network among the water molecules in lithium salt solutions.

2.3. Results and discussion

2.3.1. Effects of lithium salt concentrations on HER.

Figure 2.1 shows cyclic voltammograms on a poly-Pt electrode using the $LiTf_2N$ solutions adjusted to pH = 2.0 with four different salt concentrations. As for 1.0 M solution, redox waves appear at *ca*. –0.35 V

vs. RE (Figure 2.1(a)). Because the waves are observed around the equilibrium potential of H^+/H_2 predicted from the Nernst equation, –0.344 V vs. RE, the cathodic current is derived from proton reduction to hydrogen gas. In contrast, the increase in the $LiTf_2N$ concentration causes proton reduction to disappear around the equilibrium potential (Figures 2.1(b)–(d)). In other words, when the $LiTf_2N$ concentration is 3.0 M or higher, HER is derived only from water reduction observed at –0.80 V vs. RE and not from proton reduction. H_{upd} adsorption/desorption currents are discussed in section 2.3.2.

Figure 2.2 summarizes the cyclic voltammograms on a poly-Pt electrode using the LiCl solutions adjusted to pH = 2.0 with three different salt concentrations. Similarly, HER derived from the proton reduction appears only for the 1.0 M solution (Figure 2.2(a)). Proton reduction disappears with a LiCl solution of 5.0 M or higher (Figures 2.2(b)–(c)).

An increase in solute concentration causes HER to disappear due to proton reduction for the acidic LiCl and $LiTf_2N$ solutions, suggesting that a tight proton supply to the electrode occurs regardless of the anion species of the lithium salt. This is because as the salt concentration increases, the water molecules coordinated to Li^+ cations and the anions increase while the free water involved in proton conduction decreases. The effects of the anion species on the tight supply and the behaviors of water molecules involved in the ionic conductions are discussed in section 2.3.3.

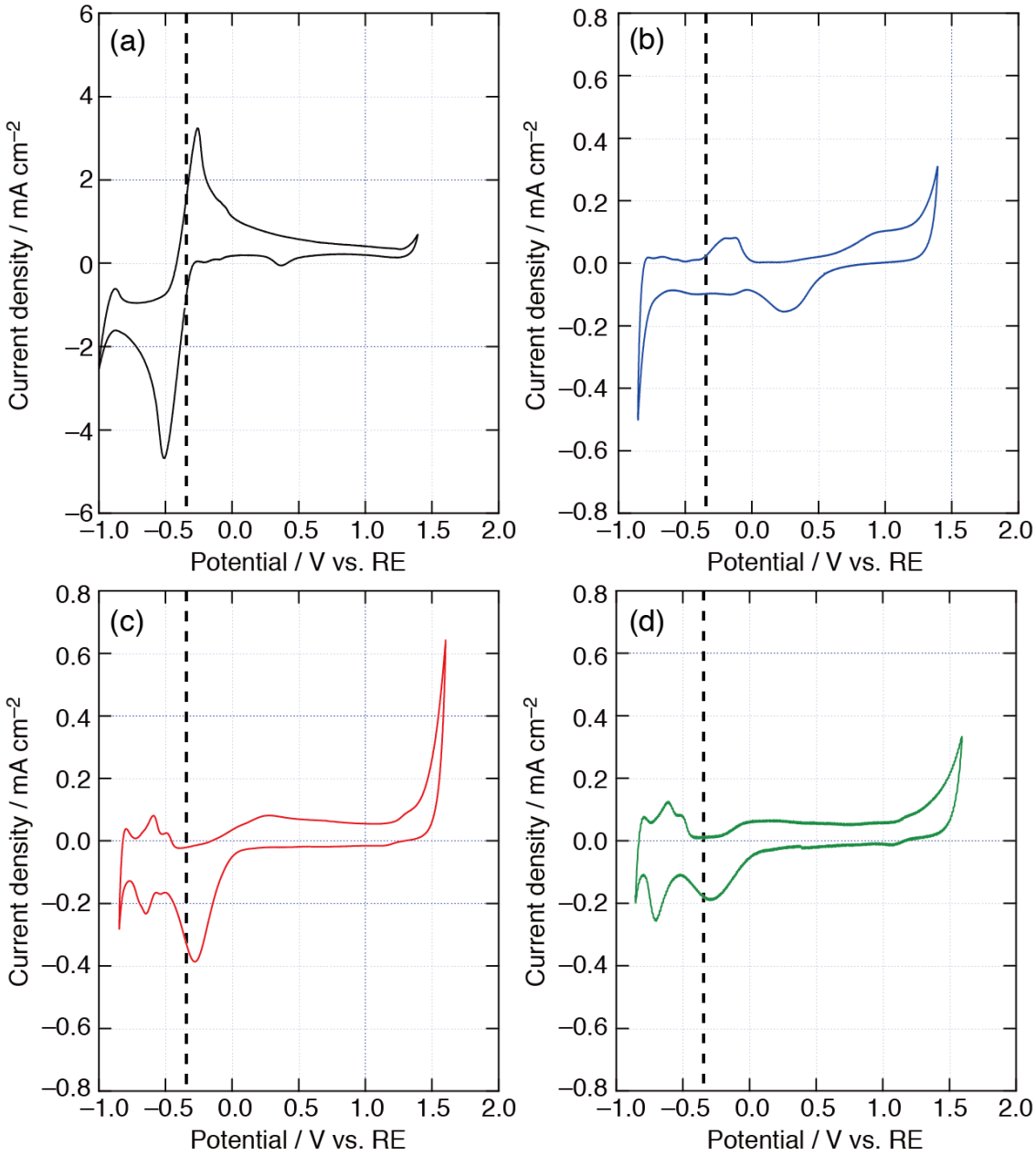

Figure 2.1 Cyclic voltammograms measured on a poly-Pt electrode for (a) 1.0 M, (b) 3.0 M, (c) 4.4 M, and (d) 5.0 M $LiTf_2N$ solutions at a scan rate of 100 mV s^{-1}. pH is 2.0. Black dashed line shows the equilibrium potential of H^+/H_2 predicted from the Nernst equation, –0.344 V vs. RE.

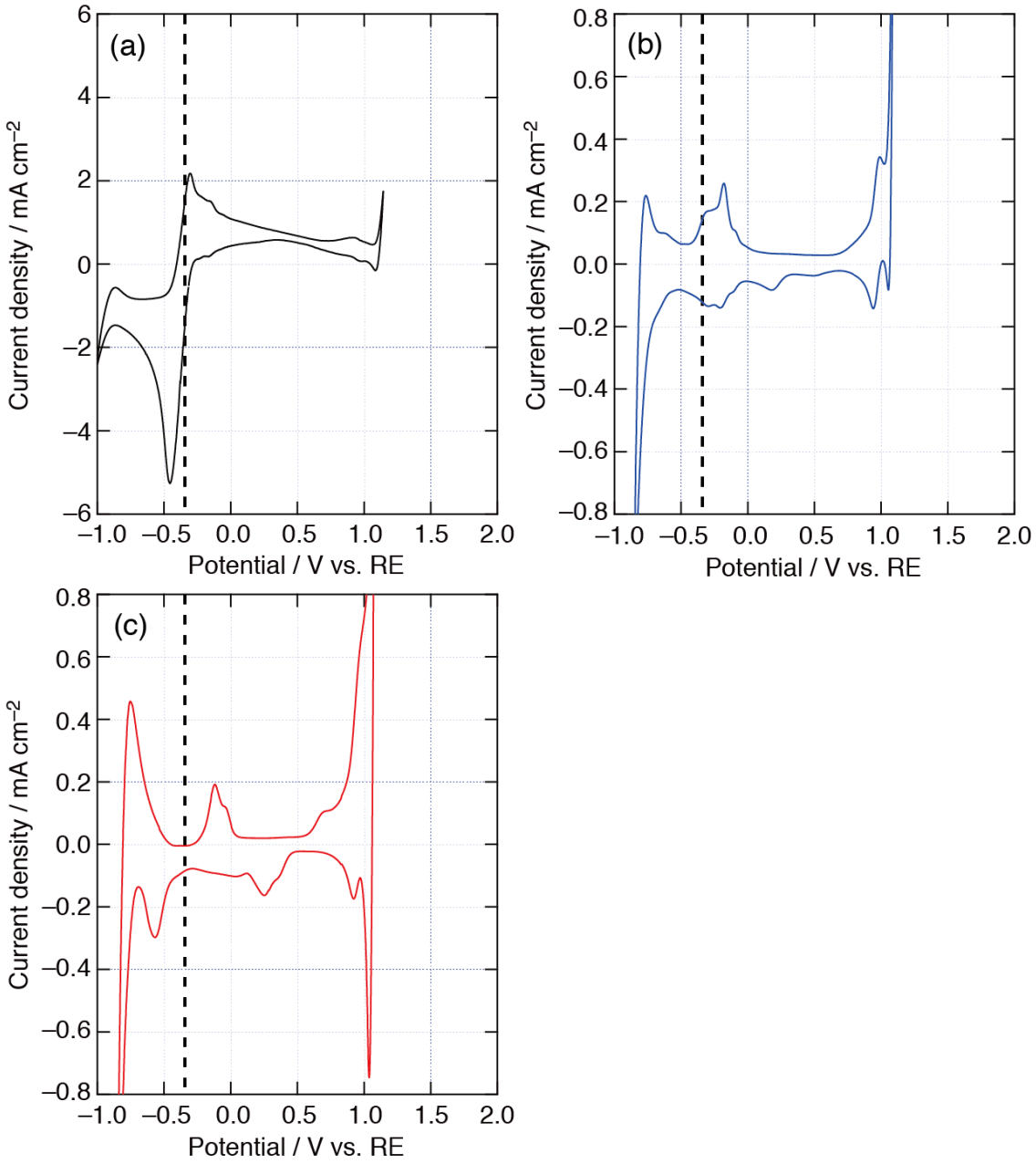

Figure 2.2 Cyclic voltammograms measured on a poly-Pt electrode for (a) 1.0 M, (b) 5.0 M, and (c) 10.0 M LiCl solutions at a scan rate of 100 mV s^{-1}. pH is 2.0. Black dashed line shows the equilibrium potential of H^+/H_2 predicted from the Nernst equation, –0.344 V vs. RE.

2.3.2. Adsorption and desorption behaviors of H_{upd} in lithium salt solutions.

To further understand the effects of anion species in concentrated lithium salt solutions on water reduction and the local conditions in the vicinity of the Pt electrode, the author investigated the H_{upd} adsorption and desorption behaviors. Figure 2.3 shows the cyclic voltammograms on a poly-Pt electrode using 10.0 M LiCl solution and 4.4 M $LiTf_2N$ solution with pH = 2.0. Both concentrated solutions have the same molality of 12.6 mol kg^{-1} (*i.e.*, the molar ratio of H_2O/lithium salt *n* is 4.4). For the $LiTf_2N$ and LiCl solutions, the H_{upd} adsorption current commonly appears at *ca.* – 0.60 V vs. RE, which is negative compared to the equilibrium potential of H^+/H_2.

The author examined the reactions for H_{upd} adsorption and desorption on Pt electrodes to trace why the cathodic current associated the H_{upd} adsorption appears at a potential more negative than the equilibrium potential. Equation (1) shows the reactions of H_{upd} adsorption and desorption on the Pt electrodes in acidic solutions, and Equation (2) shows those in neutral or alkaline aqueous solutions:

$$Pt + H^+ + e = Pt\text{-}H \qquad (1)$$

$$Pt + H_2O + e = Pt\text{-}H + OH^- \qquad (2)$$

where Pt-H represents surface Pt atoms adsorbed by H_{upd}. For simplicity, the proton species is denoted as H^+ in Eq. (1). The tight proton supply to the electrode due to a decrease in free water involved in proton conduction as the solute concentration increases leads to insufficient hydrogen atoms for the H_{upd} adsorption. As a result, the adsorption reaction comes to be derived not from the proton reduction shown in Eq. (1), but from the water reduction shown in Eq. (2).

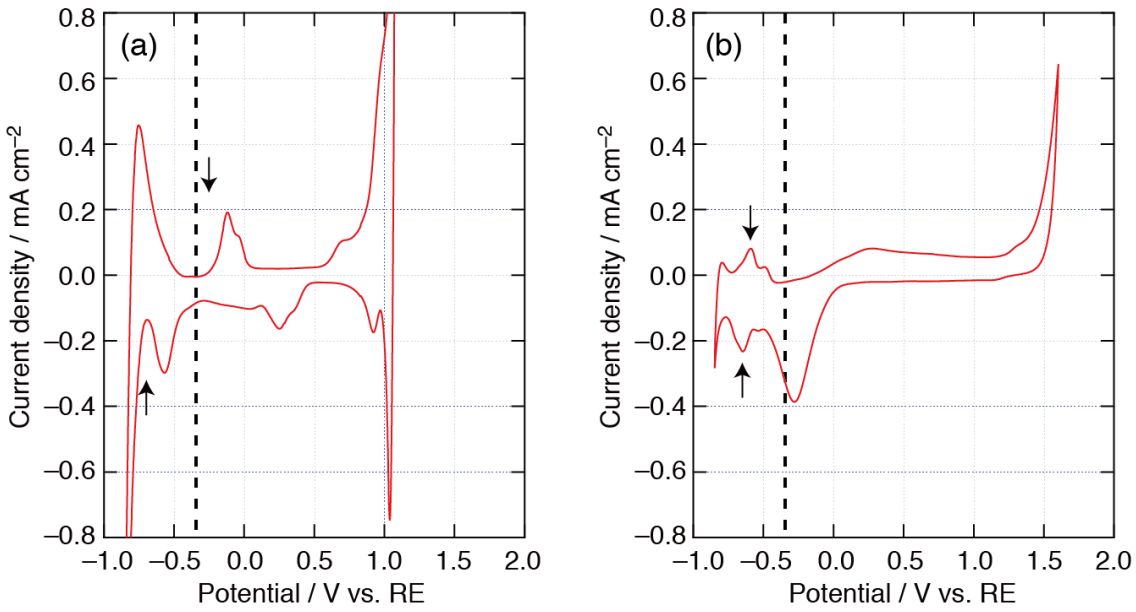

Figure 2.3 Cyclic voltammograms measured on a poly-Pt electrode for (a) 10.0 M LiCl and (b) 4.4 M $LiTf_2N$ solutions at a scan rate of 100 mV s^{-1}. Both solutions have the same molality, 12.6 mol kg^{-1} (the molar ratio of H_2O/lithium salt is n = 4.4). pH is 2.0. Black dashed line shows the equilibrium potential of H^+/H_2 predicted from the Nernst equation, –0.344 V vs. RE. H_{upd} adsorption/desorption currents are indicated by arrows.

Notably, it is widely known that the current waveform related to H_{upd} adsorption on a poly-Pt electrode is double-peaked,[26,27] and the amount of electricity required for the adsorption is *ca.* 210 μC cm^{-2} without considering the electrode roughness. Although the waveforms of the H_{upd} adsorption (Figures 2.1–3) are single-peaked, *not* double-peaked as generally reported, the amount of electricity for the adsorption is on the same order of magnitude. Several studies have mentioned that the surface structure and/or the grain size of Pt electrodes significantly affect the current waveform related to adsorption.[22–33] In particular, similar single peaks have been reported in the case involving Pt crystals with a smaller grain size.[32,33] The change in the waveform is probably derived from the changes in the surface structure and the grain size of the poly-Pt electrode during cyclic voltammetry.

In contrast to the H_{upd} adsorption, the H_{upd} desorption behaviors differ between the LiCl and $LiTf_2N$ solutions, despite having the same molality. In the LiCl solution, the anodic current due to H_{upd} desorption appears positive compared to the equilibrium potential (Figure 2.3(a)), whereas in the $LiTf_2N$ solution, both the adsorption and desorption potentials are negative (Figure 2.3(b)). This difference is accounted for based on the reactions for H_{upd} adsorption and desorption, as shown in Eqs. (1) and (2). It is reasonable to assume that the local pH in the vicinity of the Pt electrode after switching to positive-going scan is increased compared to the bulk pH (*i.e.*, pH = 2.0) due to the H_{upd} adsorption and HER. Because the H_{upd} adsorption and desorption are found at almost the same potential for the $LiTf_2N$ solution, the desorption reaction is the oxidation reaction of Eq. (2). In brief, the desorption potential for the $LiTf_2N$ solution suggests a highly increased local OH^- concentration in the vicinity of the Pt electrode. In contrast, because the desorption potential is far from the adsorption potential and is more positive than the equilibrium potential of H^+/H_2 for the LiCl solution, the desorption reaction is the oxidation reaction of Eq. (1), suggesting that the OH^- concentration is low in the vicinity of the Pt electrode. Only for neutral and near-neutral conditions, the onset potentials for HER and HOR are apart from each other due to the lack of protons and OH^- ions in the vicinity of the electrode, whereas the potentials are the same for acidic and alkaline conditions.[34–36] The discrepancy in the adsorption and desorption potentials for the LiCl suggests almost-neutral or neutral conditions in the vicinity of the Pt electrode. On the other hand, the nearly identical potentials for $LiTf_2N$ suggest that the local OH^- concentration in the vicinity of the electrode is higher compared to the LiCl cases.

Similar effects of the anion species on the H_{upd} adsorption and desorption are observed for systems with lower molality of lithium salt (*i.e.*, more free water) and with a higher bulk pH. Figure 2.4 shows cyclic voltammograms on a poly-Pt electrode using 5.0 M LiCl solution, 3.0 M

$LiTf_2N$ solution, and 4.5 M $LiClO_4$ solution with pH = 3.0. The molality of these solutions is almost the same as *ca*. 5.5 mol kg^{-1}. In solutions with a higher bulk pH and molar ratio of H_2O/lithium salt, HER derived from proton reduction is not observed like the case of Figure 2.3 (pH = 2.0, 12.6 mol kg^{-1}). The increase in free water promotes the proton conduction, whereas increasing the bulk pH leads to a tight proton supply to the electrode. As a result, regardless of the anion species, the cathodic current related to H_{upd} adsorption appears to be negative compared to the equilibrium potential because hydrogen atoms for the adsorption are generated by water reduction as shown in Eq. (2). On the other hand, the potential of H_{upd} desorption depends on the anion species. In the $LiTf_2N$ and $LiClO_4$ solutions, the desorption potential is more negative than the equilibrium potential (Figures 2.4(b) and (c)), whereas the desorption potential is positive only in the LiCl solution (Figure 2.4(a)).

For the LiCl solution, the desorption potential, which is positive compared to the equilibrium potential, indicates that the desorption reaction is the oxidation reaction of Eq. (1). Namely, the adsorption occurs as the reduction reaction of Eq. (2) and the desorption occurs as the oxidation reaction of Eq. (1) because the reduction of protons is kinetically suppressed due to their tight supply for the LiCl solution. In contrast, the desorption potential for the $LiTf_2N$ and $LiClO_4$ solutions indicates that the desorption reaction is the oxidation reaction of Eq. (2). Briefly, the H_{upd} adsorption and desorption reactions reversibly occur as the redox reaction of Eq. (2) for the $LiTf_2N$ and $LiClO_4$ solutions.

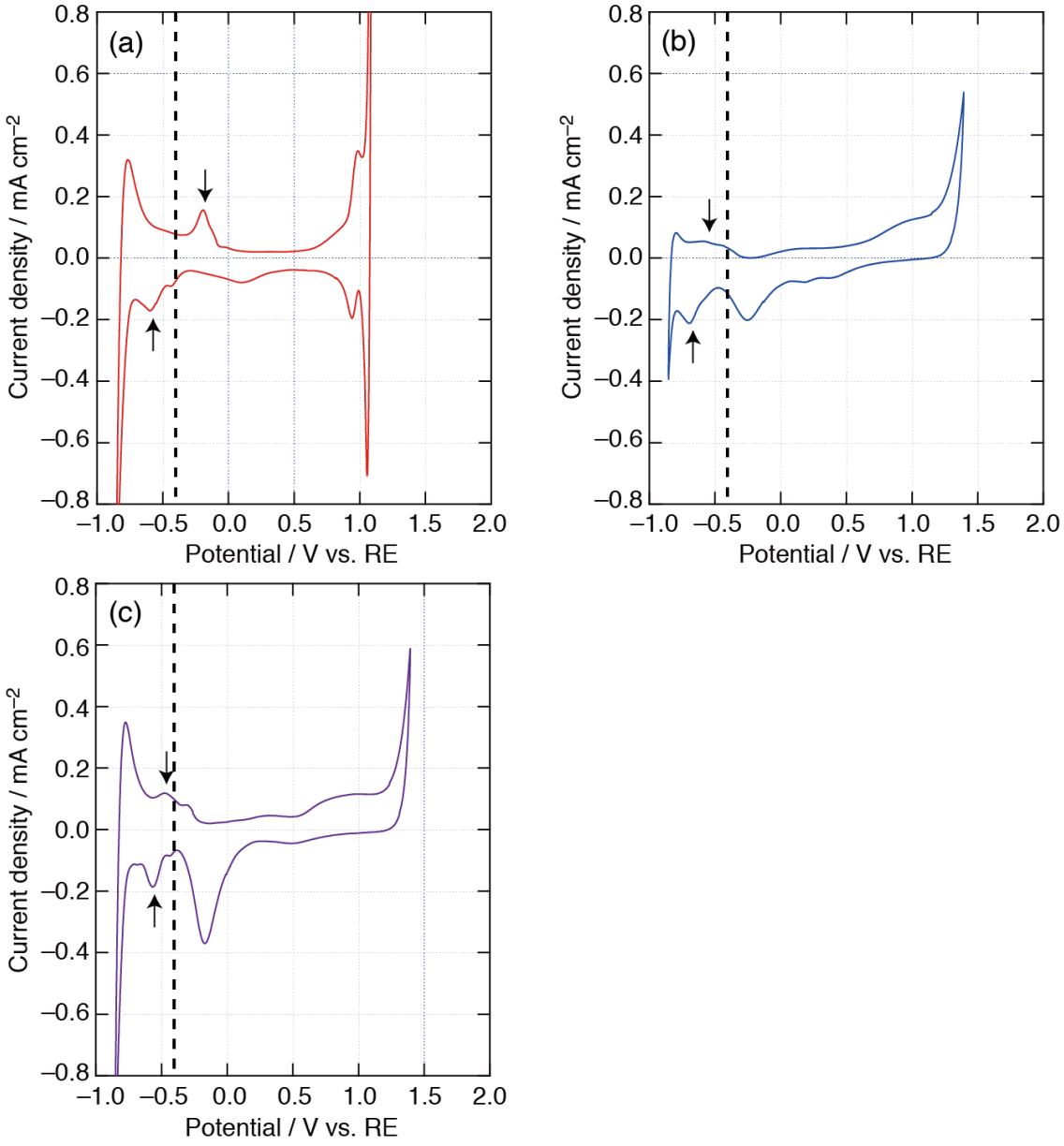

Figure 2.4 Cyclic voltammograms measured on a poly-Pt electrode for (a) 5.0 M LiCl, (b) 3.0 M $LiTf_2N$, and (c) 4.5 M $LiClO_4$ solutions at a scan rate of 100 mV s^{-1}. All solutions have almost the same molality, *ca*. 5.5 mol kg^{-1} (the molar ratio of H_2O/lithium salt is n = 10). pH is 3.0. Black dashed line shows the equilibrium potential of H^+/H_2 predicted from the Nernst equation, –0.403 V *vs*. RE. H_{upd} adsorption/desorption currents are indicated by arrows.

For the same bulk pH and molar ratio of H_2O/lithium salt, the potential of the H_{upd} adsorption is independent of the anion species of lithium salt. On the other hand, the desorption potential depends on the anion species. These results suggest that the local OH^- concentration in the vicinity of the Pt electrode is strongly affected by the anion species.

2.3.3. Discussion on the effects of anion species on H_{upd} adsorption and desorption.

The author focuses on the difference in anodic reactions to consider the effect of the anion species on the local conditions in the vicinity of the electrode, such as the local OH^- concentration. In the $LiTf_2N$ and $LiClO_4$ solutions, the bulk pH does not change because the anodic reaction is oxygen evolution. On the other hand, in the LiCl solutions, the bulk pH can increase because the anodic reaction is chlorine evolution. In fact, however, the bulk pH measured after each voltammetry was almost the same as that before them. Therefore, the difference in the anodic reactions cannot explain the local increase in the OH^- concentration in the vicinity of the Pt electrode in the $LiTf_2N$ and $LiClO_4$ solutions.

Next, the author assessed the structure of water molecules in the lithium salt solutions to understand why the anion species affects the H_{upd} adsorption or desorption behaviors and the local environments in the vicinity of the electrode. Figure 2.5 shows the IR spectra that cover the O-H stretching vibration modes of water for the LiCl, $LiTf_2N$, and $LiClO_4$ solutions with various concentrations. A typical broad absorption, which ranges from 3000 to 3800 cm^{-1}, are observed for 1.0 M $LiTf_2N$ and $LiClO_4$, and all the LiCl solutions, confirming the presence of hydrogen-bonding networks among water molecules. On the other hand, increasing the $LiTf_2N$ and $LiClO_4$ concentrations leads to a different situation. The higher shift in the O-H vibration from 3200–3500 cm^{-1} to 3500–3700 cm^{-1} indicates that the hydrogen-bonding networks among water molecules are broken. Similar shifts have been observed in aqueous solutions containing a high

concentrations of Tf_2N^- or ClO_4^- anions.[2,17.42,43] The blue shift at high ClO_4^- concentrations indicates an increase in the number of water molecules that form hydrogen bonds with ClO_4^- anions.[42] The IR spectra for the concentrated $LiTf_2N$ and $LiClO_4$ solutions show an increase in the number of water molecules interacting not with each other but with these anions, inducing the breakdown of the hydrogen-bonding networks among water molecules.

In aqueous solutions, protons and OH^- ions move with the help of hydrogen-bonding networks among water molecules. The migration is known as the Grotthuss mechanism or hopping mechanism. The breakdown of the networks results in a loss of footholds for the hopping. Therefore, the conduction of protons and OH^- ions can be suppressed compared to the case in the presence of the networks. Figure 2.6 schematically illustrates the ionic conduction between the bulk solution and the electrode affected by the presence or breakdown of the network during the water reduction. In the presence of the networks, protons can migrate quickly from the bulk solution to the electrode through the networks. Similarly, OH^- ions generated by water reduction can be eliminated rapidly from the electrode to the bulk through the network (Figure 2.6(a)). In the concentrated LiCl solutions in the presence of the network, although increasing the concentration more or less suppresses the proton supply to the electrode due to the decrease in free water involved in proton conduction, protons and OH^- ions can move through the remaining network. As a result, the H_{upd} adsorption occurs as the reduction reaction of Eq. (2), whereas the desorption occurs as the oxidation reaction of Eq. (1) due to the low OH^- concentration in the vicinity of the electrode. In contrast, a breakdown that is strong enough to change the shape of the IR spectra can suppress the ionic conduction between the bulk and the Pt electrode through the network (Figure 2.6(b)), giving a high OH^- concentration in the vicinity of the electrode compared to the presence of the networks. Therefore, in the concentrated $LiTf_2N$ and $LiClO_4$ solutions when the

network breaks down, the H_{upd} adsorption and desorption reversibly occur as the redox reactions of Eq. (2) because OH^- ions generated by water reduction stay in the vicinity of the electrode.

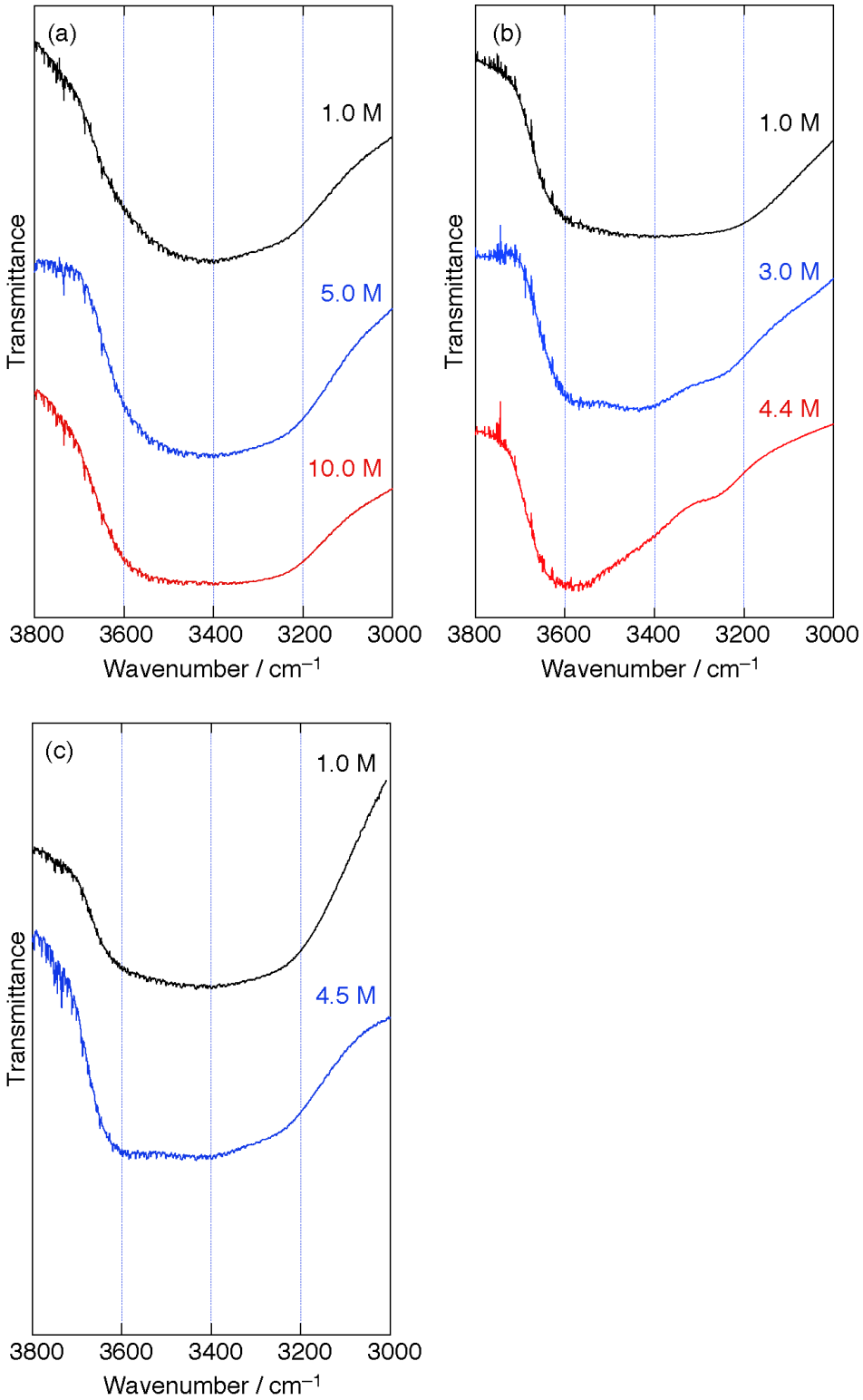

Figure 2.5 IR spectra of the O-H stretching vibration modes for (a) LiCl, (b) $LiTf_2N$, (c) $LiClO_4$ solutions at various concentrations.

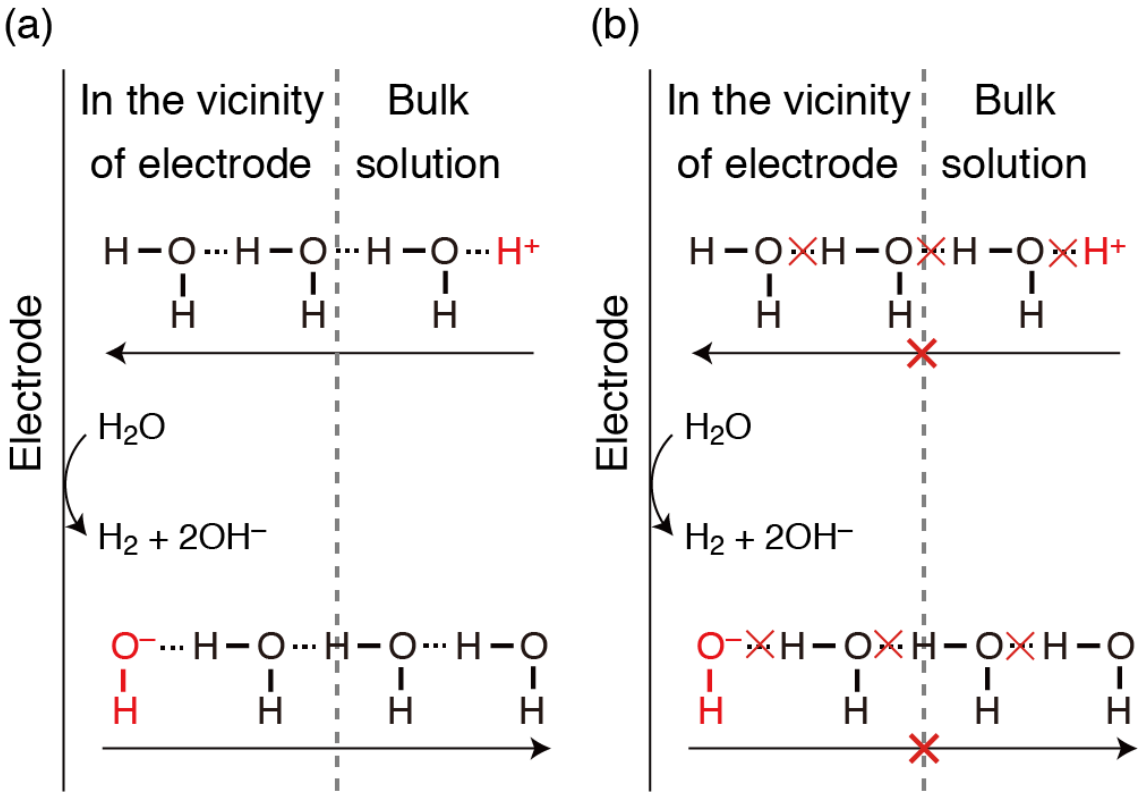

Figure 2.6 Schematic images of water reduction in the vicinity of the electrode and the conductions of protons and OH^- ions between bulk solutions and the electrode when the hydrogen-bonding networks are (a) present and (b) broken, respectively.

Cyclic voltammetry for 4.5 M $LiClO_4$ solutions where the networks are broken down were conducted at two different pH to verify whether ionic conduction affects the local conditions in the vicinity of the electrode and the H_{upd} adsorption and desorption behaviors (see Figure 2.7). For pH = 3.0, the adsorption and desorption potentials are almost the same because the adsorption and desorption reversibly occur as the redox reactions of Eq. (2) (Figure 2.7(a)). However, the potentials are far from each other for pH = 2.0 like in the case of concentrated LiCl solutions (Figure 2.7(b)). The deviation indicates that adsorption occurs as the reduction reaction of Eq. (2), whereas the desorption occurs as the oxidation reaction of Eq. (1). This is because decreasing the bulk pH (*i.e.*, increasing the bulk proton concentration) promotes its supply to the electrode and decreases the local

pH. Consequently, the local OH^- concentration in the vicinity of the electrode decreases and the H_{upd} desorption does not occur through the oxidation reaction of Eq. (2). Instead, it occurs through that of Eq. (1). The H_{upd} adsorption and desorption behaviors in the cyclic voltammetry at different pH values strongly support the fact that, despite the same bulk pH and molality, the local conditions in the vicinity of the electrode (*e.g.*, local pH) are affected by solutes used in concentrated aqueous solutions.

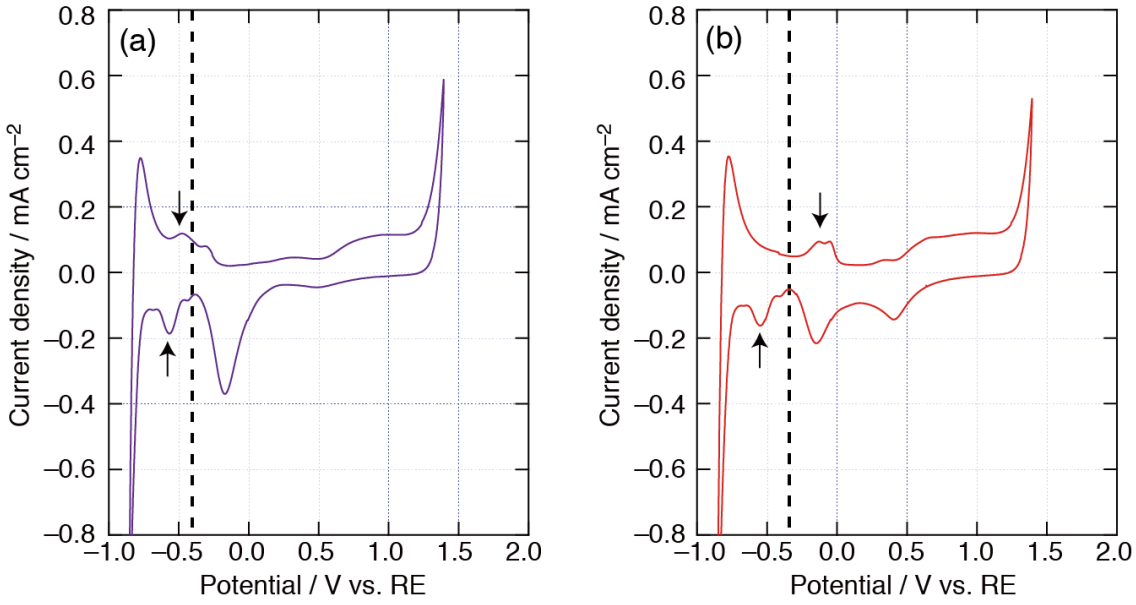

Figure 2.7 Cyclic voltammograms measured on a poly-Pt electrode for 4.5 M $LiClO_4$ solutions at a scan rate of 100 mV s^{-1}. pH values are (a) 3.0 and (b) 2.0. Black dashed lines indicate the equilibrium potentials of H^+/H_2 predicted from the Nernst equation, (a) –0.403 V and (b) –0.344 V vs. RE. H_{upd} adsorption/desorption currents are indicated by arrows.

2.4. Conclusions

Herein the author investigated the effects of the solute concentration and of counter anion species on proton reduction and H_{upd} adsorption/desorption on poly-Pt electrodes in acidic aqueous solutions

containing lithium salt. Cyclic voltammetry revealed that increasing the solute concentration causes proton reduction to disappear at the equilibrium potential of H^+/H_2 regardless of the anion. This is attributed to the suppressed proton supply to the electrode because the increased salt concentration decreases the free water involved with proton conduction. Regardless of the anion, the H_{upd} adsorption appears at a more negative potential than the equilibrium potential since the hydrogen atoms required for the adsorption are derived from the water reduction not the proton reduction. In contrast, the desorption depends on the anion. Compared to the equilibrium potential, the potential is positive only for the LiCl because the local pH in the vicinity of the electrode for the LiCl is lower than that for the $LiTf_2N$ and $LiClO_4$.

The author focused on the presence or breakdown of the hydrogen-bonding networks among water molecules. The breakdown observed only in the $LiTf_2N$ and $LiClO_4$ solutions can suppress the conduction of protons and OH^- ions through the networks, retaining the increase in local OH^- generated by water reduction due to the suppressed conduction. In other words, despite the same bulk pH and water content, the presence or breakdown of the networks due to the anion significantly affects the local conditions in the vicinity of the electrode (*e.g.*, the local pH).

This study shows that the effects of the solute and the water content in concentrated aqueous solutions on water molecules play crucial roles in water decomposition. Since the effects involve electrochemical processes that compete with water decomposition such as metal electrodeposition with a negative electrode potential, the author plans to explore the effects on such electrochemical processes in the future. Because it is essential to optimize the solution compositions to develop electrochemical devices, the author believes that the findings presented here will improve electrochemical processes and develop electrochemical devices with good performances.

References

1. L. Suo, O. Borodin, T. Gao, M. Olguin, J. Ho, X. Fan, C. Luo, C. Wang, and K. Xu, *Science*, **350**, 938 (2015).
2. Y. Yamada, K. Usui, K. Sodeyama, S. Ko, Y. Tateyama, and A. Yamada, *Nat. Energy*, **1**, 1 (2016).
3. L. Suo, O. Borodin, W. Sun, X. Fan, C. Yang, F. Wang, T. Gao, Z. Ma, M. Schroeder, A. von Cresce, M. Russell, M. Armand, A. Angell, K. Xu, and C. Wang, *Angew. Chem. Int. Ed.*, **128**, 7252 (2016).
4. C. Yang, J. Chen, T. Qing, X. Fan, W. Sun, A. von Cresce, M. S. Ding, O. Borodin, J. Vatamanu, M. A. Schroeder, N. Eidson, C. Wang, and K. Xu, *Joule*, 1, 122 (2017).
5. L. Chen, J. Zhang, Q. Li, J. Vatamanu, X. Ji, T. P. Pollard, C. Cui, S. Hou, J. Chen, C. Yang, L. Ma, M. S. Ding, M. Garaga, S. Greenbaum, H. Lee, O. Bolodin, K. Xu, and C. Wang, *ACS Energy Lett.*, **5**, 968 (2020).
6. S. Ko, Y. Yamada, and A. Yamada, *Electrochem. Commun.*, **116**, 106764 (2020).
7. L. Coustan, G. Shul, and D. Bélanger, *Electrochem. Commun.*, **77**, 89 (2017).
8. Y. Yokoyama, T. Fukutsuka, K. Miyazaki, and T. Abe, *J. Electrochem. Soc.*, **165**, A3299 (2018).
9. P. Lannelongue, R. Bouchal, E. Mourad, C. Bodin, M. Olarte, S. le Vot, F. Favier, and O. Fontaine, *J. Electrochem. Soc.*, **165**, A657 (2018).
10. W. S. V. Lee, T. Xiong, G. C. Loh, T. L. Tan, and J. Xue, *ACS Appl. Energy Mater.*, **1**, 3070 (2018).
11. D. Reber, R. S. Kühnel, and C. Battaglia, *Sustain. Energy Fuels*, **1**, 2155 (2017).

12. N. Zhang, F. Cheng, Y. Liu, Q. Zhao, K. Lei, C. Chen, X. Liu, and J. Chen, *J. Am. Chem. Soc.*, **138**, 12894 (2016).
13. C. Y. Chen, K. Matsumoto, K. Kubota, R. Hagiwara, and Q. Xu, *Adv. Energy Mater.*, **9**, 1 (2019).
14. F. Wang, O. Borodin, T. Gao, X. Fan, W. Sun, F. Han, A. Faraone, J. A. Dura, K. Xu, and C. Wang, *Nat. Mater.*, **17**, 543 (2018).
15. K. Adachi, A. Kitada, K. Fukami, and K. Murase, *Electrochim. Acta*, **338**, 135873 (2020).
16. S. De, J. White, T. Brusuelas, C. Patton, A. Koh, and Q. Huang, *Electrochim. Acta*, **338,** 135852 (2020).
17. S. Inoguchi, A. Kitada, K. Fukami, and K. Murase, *J. Electrochem. Soc.*, **167**, 162511 (2020).
18. K. Adachi, A. Kitada, K. Fukami, and K. Murase, *J. Electrochem. Soc.*, **166**, D409 (2019).
19. S. Inoguchi, K. Fukami, K. Amano, A. Kitada, and K. Murase, *ACS Omega*, **5**, 26894 (2020).
20. R. S. Kühnel, D. Reber, A. Remhof, R. Figi, D. Bleiner, and C. Battaglia, *Chem. Commun.*, **52**, 10435 (2016).
21. A. Kitada, M. Kurihara, R. Takai, K. Fukami, and K. Murase, *J. Surf. Finish. Soc. Jpn.*, **71**, 376 (2020). [DOI: 10.4139/sfj.71.376]
22. N. M. Marković, S. T. Sarraf, H. A. Gasteiger, and P. N. Ross, *J. Chem. Soc. Faraday Trans.*, **92**, 3719 (1996).
23. N. M. Marković, B. N. Grgur, and P. N. Ross, *J. Phys. Chem. B*, **101**, 5405 (1997).
24. B. E. Conway and G. Jerkiewicz, *Electrochim. Acta*, **45**, 4075 (2000).
25. K. Kunimatsu, T. Senzaki, G. Samjeské, M. Tsushima, and M. Osawa, *Electrochim. Acta*, **52**, 5715 (2007).
26. G. Jerkiewicz, *Electrocatalysis*, **1**, 179 (2010).
27. A. Zolfaghari, B. E. Conway, and G. Jerkiewicz, *Electrochim. Acta*, **47**, 1173 (2002).
28. T. J. Schmidt, U. A. Paulus, H. A. Gasteiger, and R. J. Behm, *J.*

Electroanal. Chem., **508**, 41 (2001).
29. W. Sheng, H. A. Gasteiger, and Y. Shao-Horn, *J. Electrochem. Soc.*, **157**, B1529 (2010).
30. A. P. Yadav, A. Nishikata, and T. Tsuru, *Electrochim. Acta*, **52**, 7444 (2007).
31. O. Diaz-Morales, T. J. P. Hersbach, C. Badan, A. C. Garcia, and M. T. M. Koper, *Faraday Discuss.*, **210**, 301 (2018).
32. K. J. J. Mayrhofer, B. B Blizanac, M. Arenz, V. R. Stamenkovic, P. N. Ross, and N. M. Markovic, *J. Phys. Chem. B*, **109**, 14433 (2005).
33. S. Cherevko, N. Kulyk, and K. J. J. Mayrhofer, *Nano Energy*, **29**, 275 (2016).
34. D. Strmcnik, M. Uchimura, C. Wang, R. Subbaraman, N. Danilovic, D. van der Vliet, A. P. Paulikas, V. R. Stamenkovic, and N. M. Markovic, *Nat. Chem.*, **5**, 300 (2013).
35. D. Strmcnik, P. P. Lopes, B. Genorio, V. R. Stamenkovic, and N. M. Markovic, *Nano Energy*, **29**, 29 (2016).
36. T. Shinagawa, A. T. Garcia-Esparza, and K. Takanabe, *ChemElectroChem*, **1**, 1497 (2014).
37. P. S. Lamoureux, A. R. Singh, and K. Chan, *ACS Catal.*, **9**, 6194 (2019).
38. T. Shinagawa and K. Takanabe, *Phys. Chem. Chem. Phys.*, **17**, 15111 (2015).
39. I. Katsounaros, J. C. Meier, S. O. Klemm, A. A. Topalov, P. U. Biedermann, M. Auiger, and K. J. J. Mayrhofer, *Electrochem. Commun.*, **13**, 634 (2011).
40. M. Auinger, I. Katsounaros, J. C. Meier, S. O. Klemm, P. U. Biedermann, A. A. Topalov, M. Rohwerder, and K. J. J. Mayrhofer, *Phys. Chem. Chem. Phys.*, **13**, 16384 (2011).
41. Z. Zhou, Z. Pei, L. Wei, S. Zhao, X. Jian, and Y. Chen, *Energy Environ. Sci.*, **13**, 3185 (2020).
42. A. W. Omta, M. F. Kropman, S. Woutersen, and H. J. Bakker, *J.*

Chem. Phys., **119**, 12457 (2003).

43. Y. Chen, Y. Zhang, and L. Zhao, *Phys. Chem. Chem. Phys.*, **6**, 537 (2004).
44. G. E. Dima, A. C. A. De Vooys, and M. T. M. Koper, *J. Elecrtroanal. Chem.*, **555**, 15 (2003).
45. J. Yang, F. Calle-Vallejo, M. Duca, and M. T. M. Koper, *ChemCatChem*, **5**, 1773 (2013).
46. E. A. Ambundo, M. Deydier, A. J. Grall, N. Aguera-Vega, L. T. Dressel, T. H. Cooper, M. J. Heeg, L. A. Ochrymowycz, and D. B. Rorabacher, *Inorg. Chem.*, **38**, 4233 (1999).

Chapter 3

Reactivity of zinc cations under spontaneous accumulation of hydrophobic coexisting cations in hydrophobic nanoporous silicon

3.1. Introduction

Highly concentrated aqueous solutions possess unique functions, which are advantageous for electrochemical reactions and the development of electrochemical devices. For example, water decomposition is suppressed by reducing the amount of water in aqueous solutions. In the case of an extremely high concentration, such solutions are referred to as the so-called hydrate melts.[1–3] Since it has been reported that lithium bis(trifluorosulfonyl)amide hydrate melts (21 mol kg^{-1}) exhibit a remarkable expansion of the electrochemical window,[4] several studies have attempted to apply hydrate melts to batteries and electric double capacitors.[4–7] In addition, concentrated solutions with suppressed hydrogen evolution have been applied to electrodeposition processes.[8–10] Adachi *et al.* demonstrated chrome plating with a high current efficiency using a calcium chloride ($CaCl_2$) or lithium chloride (LiCl) hydrate melt based on trivalent chromium baths.[7] Increasing of an electrolyte concentration also affects the ionic interactions. Smith *et al.* have demonstrated that the Debye length increases as the concentration of sodium chloride (NaCl) aqueous solution increases.[11]

Nanoconfinement also induces other unique properties in aqueous solutions. The properties of solutions confined within nanopores with various shapes, such as cylindrical, spongy, cage-like, and dendritic in

shape, have gained prominence in diverse fields such as biology and nanotechnology.[12–16] According to the IUPAC definition, pores can be divided into 3 categories as macropores being pores with larger than 50 nm in diameter, mesopores being those with 2–50 nm, and micropores being pores with smaller than 2 nm. In such studies including the present study, pores with smaller than 50 nm in diameter have been often utilized as nanoporous materials. As a striking example, the decreased water activity in DNA nanocages has affected the folding of DNA structures.[12] In nanotechnology, Raman spectroscopy has revealed a remarkable increase in the melting points of water inside carbon nanotubes with *ca.* 1 nm in diameter.[15] Otake *et al.* also have reported a high proton conduction in water confined within metal-organic nanotubes.[16]

Porous materials with numerous nanopores exhibit unique phenomena, which are associated with aqueous media. Previous studies have focused on the hydrophobic effect that induced an anomalous behavior in aqueous solutions confined within nanopores.[17–21] Theoretical analyses have suggested that, even when the bulk is stable as a single phase, surface-induced phase separation can create a second phase with high concentrations of hydrophobic solutes in the vicinity of a hydrophobic surface.[22,23] In addition, the acceleration of ion penetration and ion enrichment within the nanopores of porous silicon (Si) have been demonstrated due to surface-induced phase separation by tuning the solute hydrophobicity and the pore diameter. The acceleration of ion penetration and the ion enrichment have enhanced the metal deposition and local pH control within the nanopores.[19–21] In particular, longer alkyl chains of hydrophobic alkylammonium cations have been reported to induce more rapid and a larger shift in the local pH.[21] It should be noted that the term *surface-induced phase transition* has often been used instead of *surface-induced phase separation*. However, the present study deals with the phase transition between a liquid and a solid. To avoid confusion, the term surface-induced phase separation is used to denote the accumulation

of hydrophobic solutes into hydrophobic nanopores. These studies on the surface-induced phase separation in porous Si have examined the behaviors only when using dilute solutions with concentrations less than 0.1 M (= mol dm^{-3}) of alkylammonium cations.

To date, studies have yet to observe surface-induced phase separation using highly concentrated aqueous solutions with anomalous properties. Here, the author investigates the effect of the bulk concentration of an aqueous solution containing alkylammonium cations on the ion enrichment behavior within nanopores of porous Si due to surface-induced phase separation, especially in view of an extremely high concentration in the bulk. Electrochemical measurements and thermal analysis are conducted to evaluate the local increase in the pH as well as the reactivity of hydrated zinc ions confined within nanopores where the surface-induced phase separation of hydrophobic ions is anticipated. Although the original motivation of the present study was to fabricate a sophisticated p–n junction devices by filling n-type zinc oxide within the nanopores of p-type Si driven by the local pH change, the precipitation reaction of zinc oxide is extremely hard within the nanopore of porous Si as reported later. Thus, in the present paper, the author switches the motivation to understand the physicochemical mechanism of the low reactivity of zinc cations confined within the hydrophobic nanopores of porous Si.

3.2. Experimental

Materials. Tetraethylammonium chloride (TEACl), tetrabutylammonium chloride (TBACl) and zinc chloride ($ZnCl_2$) were purchased from Nacalai Tesque. All reagents were used as received. Their aqueous solutions were prepared with ultra-pure water (18.2 MΩ cm, Millipore, Milli-Q Reference A+).

Fabrication of porous Si. Nanoporous Si substrates with dendritic pores growing perpendicular to the substrate surface were prepared by electrochemical anodization of p-type Si (100) with a resistivity of 0.005–0.03 Ω cm in a 22 wt.% HF solution (48 wt.%. HF : ethanol (≥ 95.0% purity in volume) = 1 : 1.7 in volume). Before anodization, the Si wafer was dipped in a 5 wt.% HF solution to remove the native oxide. Electrochemical anodization was performed at an anodic current density of 40 mA cm^{-2} for a pore diameter of *ca*. 20 nm. The duration was tuned to create a membrane thickness of *ca*. 36 μm. The anodized area was 0.79 cm^2. The substrate and the membrane of porous Si were kept wet during the washing process because the solutions for ion enrichment cannot infiltrate the pores if they are dry.

Nanoporous Si substrates with 2 nm in diameter were also prepared by electrochemical anodization of p-type Si (100) with a resistivity of 1.0–4.5 Ω cm in a 22 wt.% HF solution. The substrate possessed also dendritic pores. After using a 5 wt.% HF solution to remove the native oxide, anodization was performed at an anodic current density of 2 mA cm^{-2}. The duration is tuned to fabricate a porosified layer thickness of *ca*. 2 μm because a thick layer cannot be fabricated. The nanoporous Si substrate with 2 nm in diameter was similarly kept wet during the washing process.

Open-circuit potential measurements. The open-circuit potential of nanoporous Si was measured using a potentiostat (SP-150, Bio-Logic Science Instruments) in aqueous solutions containing alkylammonium cations. In the case of TEACl solutions, the concentration was varied from 0.001 to 3.0 M. In the case of TBACl solutions, the concentration was varied from 0.001 to 1.0 M because the solubility of TBACl was lower compared to that of TEACl. A specific amount of a solution containing alkylammonium cations, whose concentration was 1.11 times higher than

the target concentration, was added into the electrochemical cell withnanoporous Si immersed in pure water to observe the ion penetration in the nanopores. In this observation, nanoporous Si was immersed into a small amount of water to realize aqueous solutions with high concentrations.

The open-circuit potential was also measured in the case of dipping in a $ZnCl_2$ solution prior to adding the TEACl solution. In this case, the measurement was performed using a 1.0 M TEACl solution. The nanoporous Si was immersed in a specific amount of the 0.2 M $ZnCl_2$ solution for 10 min. The pH of the $ZnCl_2$ solution was adjusted to 5.0 using HCl. In these $ZnCl_2$ solutions, Zn^{2+} cations exist as a hydrated ion and do not coordinate with Cl^- anions in the bulk.[24] After immersion, the same amount of TEACl solutions but twice as concentrated was added into the electrochemical cell with porous Si. After the measurement, cross-sectional views of the porosified layer were observed with a scanning electron microscope (SEM; VE-7800, KEYENCE) and analyzed by energy-dispersed X-ray spectroscopy (EDX; Element EDS system, EDAX). To examine the dependence of the pore size on the precipitation of the zinc hydroxychloride within the nanopores, the same observations using nanoporous Si substrates with 2 nm in diameter were also performed.

Thermal analysis. Differential scanning calorimetry (DSC) measurements were performed on a standard DSC apparatus (DSC8231, Rigaku). A self-supported porosified layer was detached from the substrate by applying an anodic current density of 500 mA cm^{-2} for 1 sec immediately after anodization.[25] The layer was dipped into the TEACl solution at various concentrations for 10 min. The layer was broken into fragments of a few mm^2 and put in an aluminum capsule with a few mg of aqueous electrolytes prior to hermetically sealing the capsule. For comparison, measurements using TEACl solutions without the porosified layer were also performed.

The author focused only on the melting behavior of aqueous electrolytes because the freezing behavior was not reproducible due to overcooling. Melting was measured at a scanning rate of 2 °C min^{-1}.

3.3. Results

3.3.1. Electrochemical detection of the local increase in pH within the hydrophobic nanopores.

The open-circuit potential is determined by the simultaneous progress of Si oxidation ($SiO_2 + 4H^+ + 4e = Si + 2H_2O$; $E°$ = –0.86 V *vs.* SHE) and proton reduction ($2H^+ + 2e = H_2$; $E°$ = 0 V *vs.* SHE). The electrode potentials of both reactions shift by –0.059 V per pH based on the Nernst equation. Therefore, the open-circuit potential can be regarded as the mixed potential as a function of pH. Figure 3.1 shows the time development of the open-circuit potential measured on a nanoporous Si electrode in a 1.0 M TEACl solution. Immediately after adding the TEACl solution to the electrochemical cell, the potential negatively shifts. The penetration of TEA^+ from the bulk into the nanopores is drastically accelerated due to the surface-induced phase separation of TEA^+ within the hydrophobic nanopores. Upon adding the solution, the TEA^+ concentration within the nanopores is higher than that of Cl^- because the mass-transfer of the surface-induced phase separation is much faster than the diffusion in the bulk solution.[19] Table 3.I summarizes the bulk pH of TEACl solutions at various concentrations. Although the TEACl solution is weakly acidic, the local pH of the solutions confined within the nanopores increases to balance the charge neutrality due to the difference between the concentrations of Cl^- and accumulated TEA^+. The negative potential shift is largest when the TEA^+ concentration within the nanopores is the highest because the large potential shift corresponds to the large increase in the

TEA^+ concentration.

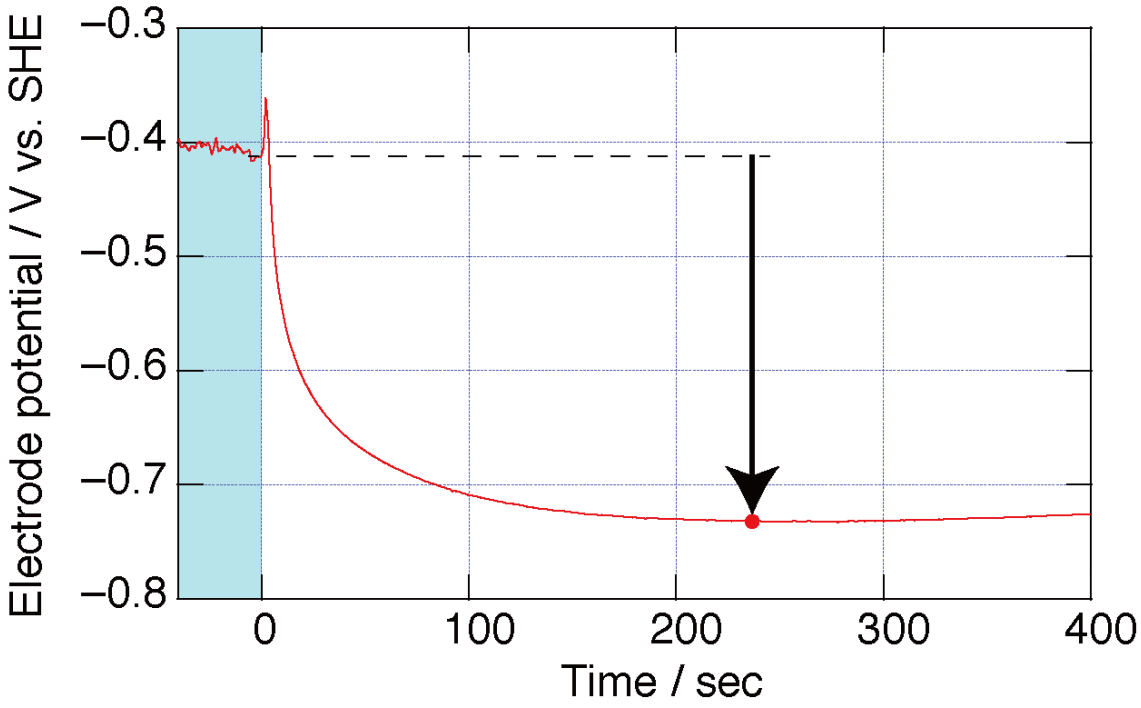

Figure 3.1 Time development of the potential measured on nanoporous Si in 1.0 M TEACl solution. Potential before 0 s is measured in pure water, while the potential after 0 s is measured in 1.0 M TEACl solution. Arrow indicates the maximum potential shift.

Table 3.I Bulk pH for TEACl solutions with various concentrations.

Bulk concentration /M	pH
0.0	5.4
0.001	6.2
0.005	6.1
0.01	5.6
0.02	5.6
0.05	5.5
0.1	5.5
0.2	5.7
0.3	5.7
0.5	5.5
1.0	5.6
1.5	5.5
2.0	5.3
3.0	5.3

Here, the author focuses on the maximum negative potential shift and evaluate the amount of TEA^+ enriched within the nanopores as a function of the TEA^+ concentration in the bulk. Figure 3.2 shows the dependence of the bulk concentration on the potential shift. The maximum potential shift increases as the bulk TEA^+ concentration increases. In addition, the maximum potential shift changes linearly with the logarithm of the bulk concentration. The shift increases by *ca.* 120 mV when the bulk

concentration is 10 times higher. Since the open-circuit potential should be determined by the pH of the solution, the change in the local pH is estimated based on the Nernst equation. According to this equation, the open-circuit potential shifts to –0.059 V per pH change of 1.0. The local increase of pH in the confined solution is *ca*. 2.0 when the bulk TEA^+ concentration was 10 times higher. Thus, as the bulk TEA^+ concentration became higher, the local pH of the confined solution rapidly increases, which is triggered by the significant TEA^+ enrichment within the nanopores with hydrophobic surfaces.

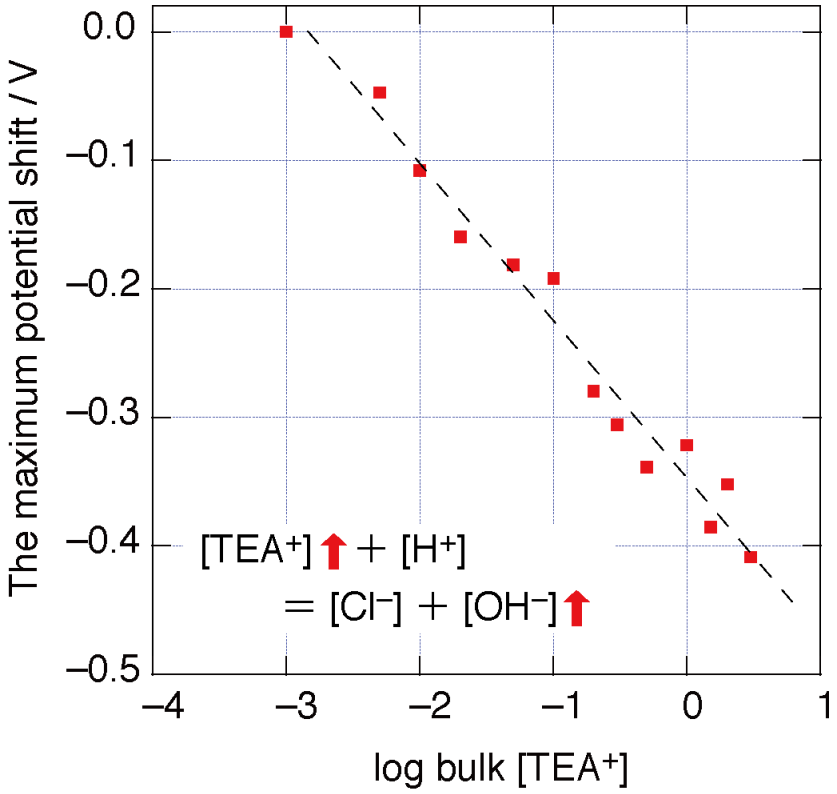

Figure 3.2 Bulk TEA^+ concentration as a function of the maximum potential shift. Bulk TEA^+ concentration is varied from 0.001–3.0 M.

Similarly, the maximum potential shift increased as the bulk concentration increased when using TBACl as the more hydrophobic case. This result indicates that the local pH within the nanopores increases with increasing the bulk TBA^+ concentration.

3.3.2. Thermal detection of the local increase in pH within the hydrophobic nanopores.

Here, the melting behaviors of the bulk and confined solutions within the nanopores are evaluated by DSC measurements to verify the TEA^+ enrichment within the nanopores (Figure 3.3). Figures 3.3(a) and (b) show the DSC melting curves of the bulk TEACl solution and the solution confined within the porosified Si membrane, respectively. It should be noted that the porosified Si membrane contained the confined solution within the nanopore as well as an excess bulk solution outside the membrane. Several thermoporometry studies using porous silica have adopted the extrapolated onset temperature of the endothermal peak in the heating curve as the melting point of the solid phase.[25–27] Here, the author focuses on the extrapolated temperatures of the endothermal peaks in Figure 3.3 as the onset of the solution melting (Table 3.II). In Figure 3.3(a), the endothermal peaks derived from the solution melting gradually shift to a lower temperature as the bulk TEACl concentration increases. When the bulk concentration is 2.0 M or higher, the extrapolated temperature of the peak is fixed at –23.7 °C in accordance with the TEACl-H_2O eutectic temperature.[28] Thus, the TEACl-H_2O eutectic point is detected when the bulk concentration is 2.0 M or higher.

Since the endothermal peaks marked with black circles in Figure 3.3(b) are detected only when the measurements are carried out using the porosified membrane, they are attributed to the phase transition from solid to liquid with regard to the solution confined within the nanopores from solid to liquid. In the case of pure water, the peak derived from the melting of the confined solution is detected at a lower temperature than that derived from the melting of the bulk solution at 0 °C. This drop in the melting point is attributed to the Gibbs-Thomson effect, which appears when confining the solution within the nanopores. Several studies have demonstrated the melting point of pure solvents confined within the nanopores of porous

materials decreases due to the Gibbs-Thomson effect. The shift in the melting point of pure solvents due to the nanoconfinement, ΔT_m, can be calculated by the Gibbs-Thomson equation as

$$\Delta T_m = T_{m,bulk} - T_{m,confined} = 2T_{m,bulk}\gamma_{sl}v_l/(r_{pore}\Delta H_{sl}) \quad (1)$$

where $T_{m,bulk}$ and $T_{m,confined}$ represent the transition temperatures of the bulk solvent and the solvent confined within the nanopores, respectively. γ_{sl} is the surface excess free energy of the solid-liquid interface, v_l is the molar volume of the solvent, ΔH_{sl} is the molar melting enthalpy of the bulk, and r_{pore} is the average pore radius. According to Equation (1), the average diameter can be estimated once ΔT_m is experimentally obtained.[25–27] The reported values of γ_{sl} and ΔH_{sl} of pure water are 25 mJ m^{-2} and 6.01 kJ mol^{-1}, respectively. In the present analysis, the average pore diameter $2r_{pore}$ is calculated from the peak temperature of the endothermal peak. The peak temperature using pure water is –4.7 °C and the calculated average pore diameter is *ca.* 17 nm, which agrees well with the actual pore size reported in previous studies.[17–21]

When the bulk concentration is 0.1 M or less, the extrapolated temperature of the confined solution is 7–10 °C lower than that of the bulk solution. The difference between the extrapolated temperatures of pure water is 9.2 °C. Hence, in the case of dilute TEACl solutions, the dominant factor of the drop in the melting point is the Gibbs-Thomson effect and not solute enrichment.

On the other hand, the endothermal peak derived from the confined solution appears near the TEACl-H_2O eutectic temperature when the bulk concentration is 0.5 M or higher (Figure 3.3(b)). Comparing with Figure 3.3(a), this endothermal peak indicates that the TEACl concentration within the nanopores increased to *ca.* 2.0 M using the 0.5 M TEACl solution. For case of the 0.5 M TEACl solution, the difference of the extrapolated

temperatures between the bulk and the confined solutions is *ca.* 20 °C, which is much larger than that using dilute solutions. The larger difference for the concentrated solutions indicates that the drop in the melting point for the confined solution is due to more than the Gibbs-Thomson effect. The hydrophobic solutes enriched within the nanopores due to the surface-induced phase separation have a non-trivial impact on the expansion of the drop in the melting point. In other words, the DSC thermograms suggest an enrichment behavior of hydrophobic solutes within the nanopores with hydrophobic surfaces.

Furthermore, in the presence of the porosified layer, another endothermal peak appeared below the TEACl-H_2O eutectic temperature when the bulk concentration is 1.0 M or higher (Figure 3.3(b)). The extrapolated temperature of the peak agrees well with the reported value of TEAOH-H_2O eutectic temperature as –35.4 °C.[29] The eutectic point do not appear without the porosified layer. The DSC thermograms reveal not only a simple solute enrichment within the nanopores but also a remarkable increase in the concentration of OH^- to maintain the charge balance due to the accumulation of TEA^+.

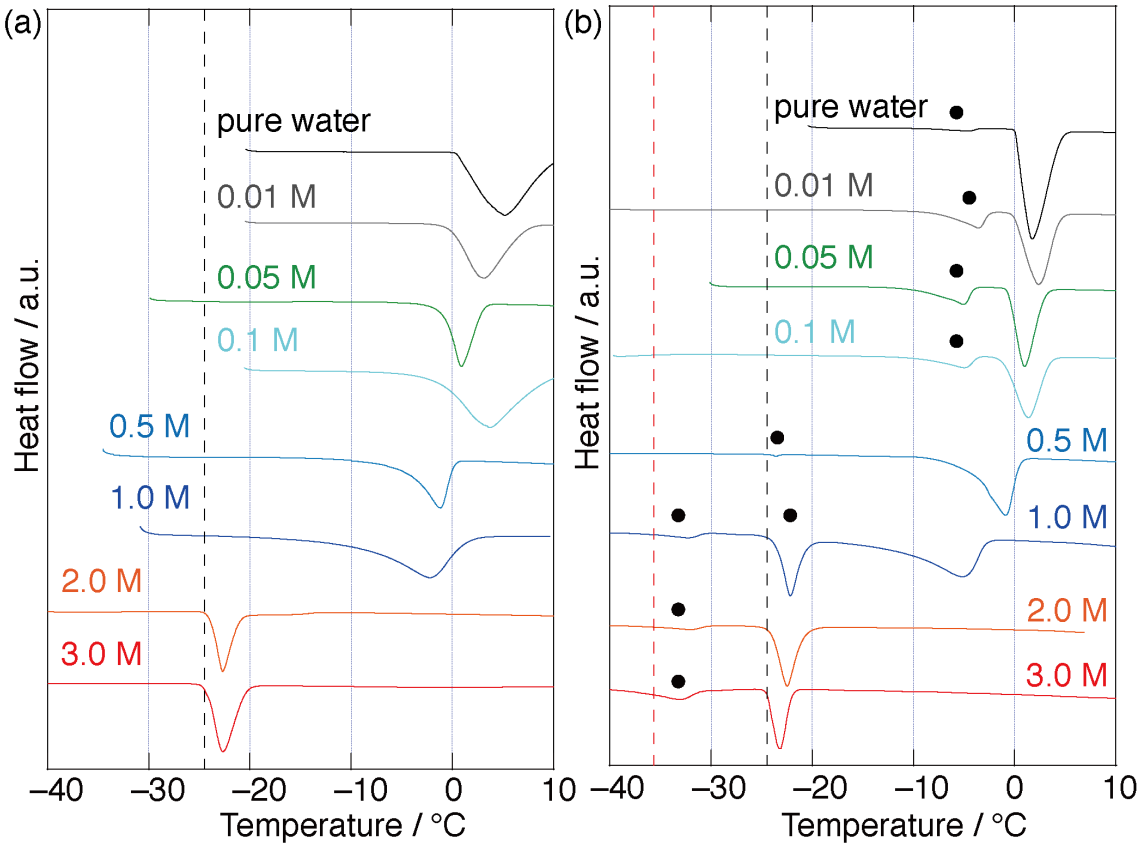

Figure 3.3 DSC melting curves of TEACl solutions with various concentrations. (a) and (b) Melting curves in the absence and presence of the porosified layer of nanoporous Si, respectively. Black and red broken lines indicate the eutectic temperatures of TEACl-H_2O (–24.5 °C) and TEAOH-H_2O (–35.7 °C), respectively. Black circles indicate endothermal peaks that appear only in the presence of the porosified layer. DSC measurement scan rate is 2 °C min^{-1}.

Table 3.II Extrapolated temperatures of the DSC melting curve for TEACl solutions with various concentrations in the bulk and confined within nanopores of nanoporous Si.

Bulk concentration /M	T_{melt} in bulk /°C	T_{melt} within nanopores /°C	
0.0	0.3	–9.5	–
0.01	0.0	–7.5	–
0.05	–1.0	–8.6	–
0.1	–1.2	–9.2	–
0.5	–4.6	–24	–
1.0	–8.2	–24	–37
2.0	–24	–24	–38
3.0	–24	–24	–40

3.3.3. Reactivity of zinc cations confined within the hydrophobic nanopores.

Both electrochemical and DSC measurements confirmed the increase in the OH^- concentration within the nanopore of porous Si. Hence, controlling the local pH should selectively precipitate metal hydroxide. Here, zinc hydroxychloride precipitation to evaluate the reactivity of zinc cations is chosen. According to the thermodynamic data, water-insoluble $Zn_5(OH)_8Cl_2$ precipitates when the pH of the 0.2 M $ZnCl_2$ solution exceeds 5.7.[24] First, the pH of the 0.2 M $ZnCl_2$ solution is adjusted to 5.0 and the nanopore is filled with the solution. Then 2.0 M TEACl is injected to promote the increase in the local pH within the nanopores. Note that the volumes of the abovementioned solutions were the same as those before mixing, so that the solutions have a final concentration that is half of the initial concentration.

Figure 3.4 shows the EDX mapping of the porosified layer of the porous Si immersed in the 0.2 M $ZnCl_2$ solution for 10 min. This experiment is carried out to detect zinc and chlorine within the nanopores. Therefore, this porous Si is not cleaned with pure water after immersion, the excess bulk solution outside the porous layer is removed. Zinc and chlorine are detected in the entire porous layer.

Figure 3.5 shows the time development of the open-circuit potential when adding the solution to a cell where the porous Si is filled with the solution of $ZnCl_2$. When adding the TEACl solution, the potential shift is – 0.20 V. According to the Nernst equation, the pH of the solution confined within the nanopores should be 8.4.

Figure 3.6 shows the cross-section of a sample after the addition of the TEACl solution to the nanopores filled with the $ZnCl_2$ solution. Similar to Figure 3.4, the porous Si is not cleaned to confirm the detection of zinc and chlorine within the nanopores when the TEA^+ cations penetrate. Zinc and chlorine are detected in the porosified layer after adding the TEACl

solution. Hence, a certain zinc compound exists within the nanopores after the TEA^+ penetration. To confirm whether the detected zinc compound is soluble or insoluble in water, the cross-section of a sample, which is prepared using the same scheme as the sample in Figure 3.6 except it is cleaned with ultra-pure water, was analyzed (Figure 3.7). Zinc and chlorine are not detected in the nanopores, indicating that the zinc compound detected in Figure 3.6 is a water-soluble zinc chloride. This result is contradictory to the expectation based on the thermodynamic data of the bulk solution. In the case of nanoporous Si with *ca*. 2-nm pore size, zinc hydroxychloride did not precipitate as well within the nanopores despite the fact that the local OH^- concentration increased similar to the case of nanoporous Si.

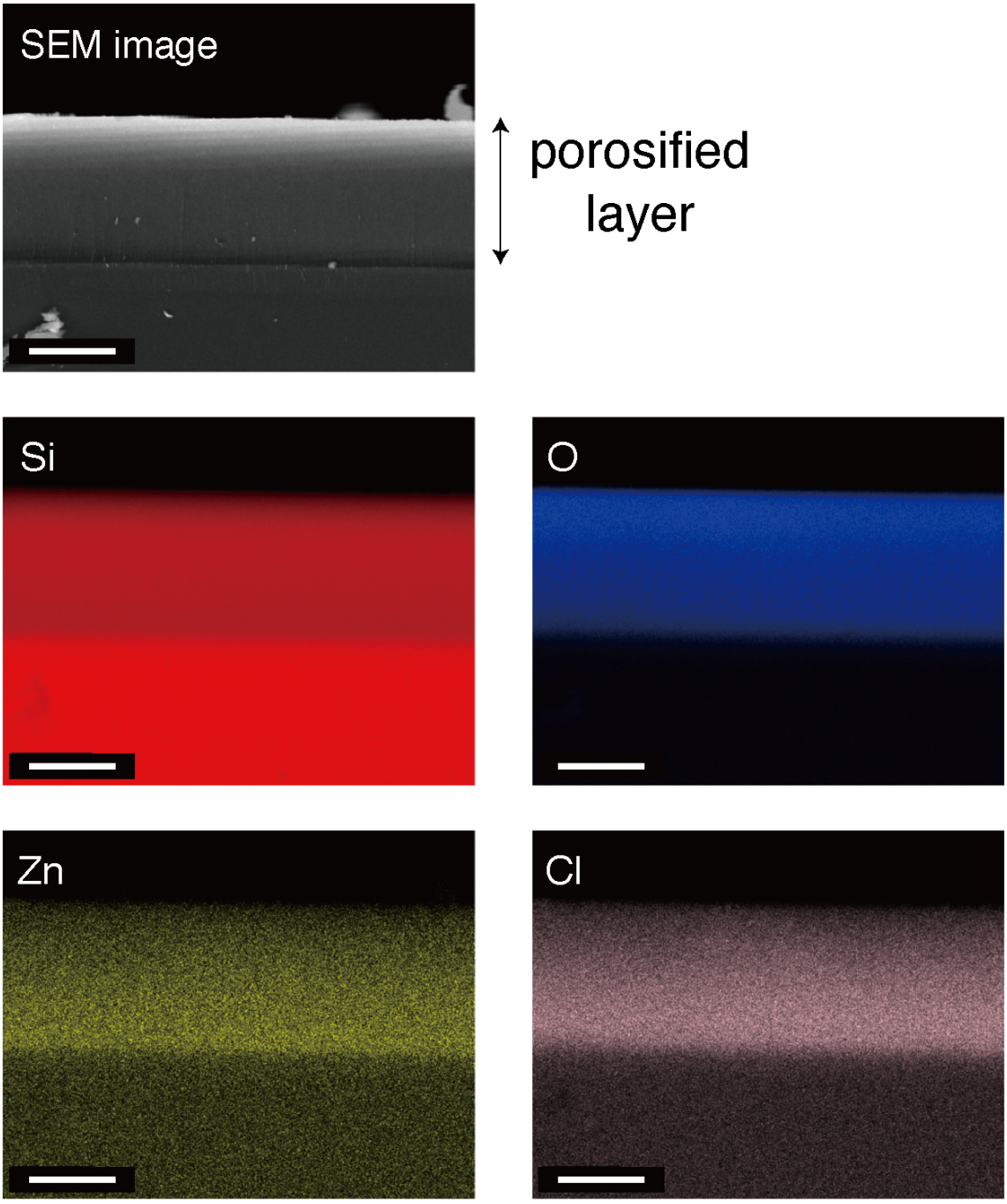

Figure 3.4 SEM image and EDX mappings for the porosified layer of nanoporous Si after immersion in 0.2 M $ZnCl_2$ solution for 10 min without cleaning. White line indicates 20 μm.

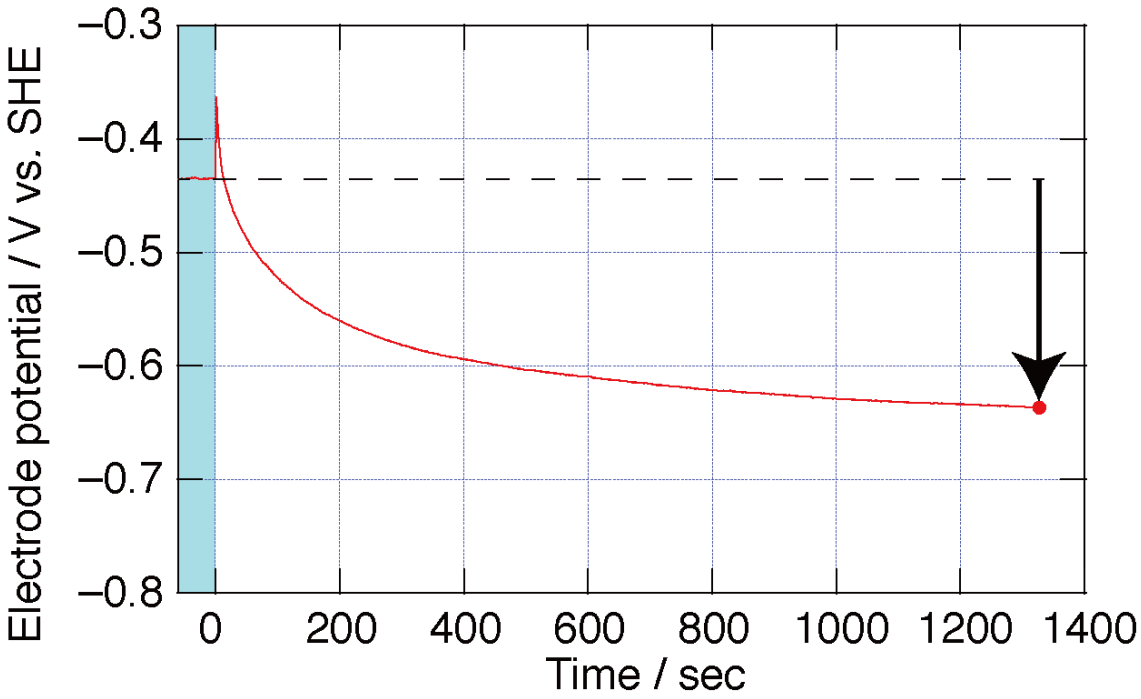

Figure 3.5 Time development of the potential measured on nanoporous Si in 1.0 M TEACl solution after immersion in 0.2 M $ZnCl_2$ solution for 10 min. Potential before 0 s is measured in 0.2 M $ZnCl_2$ solution whose pH is adjusted to 5.0, while the potential after 0 s is measured in 1.0 M TEACl solution. Arrow indicates the potential shift and the value is –0.20 V.

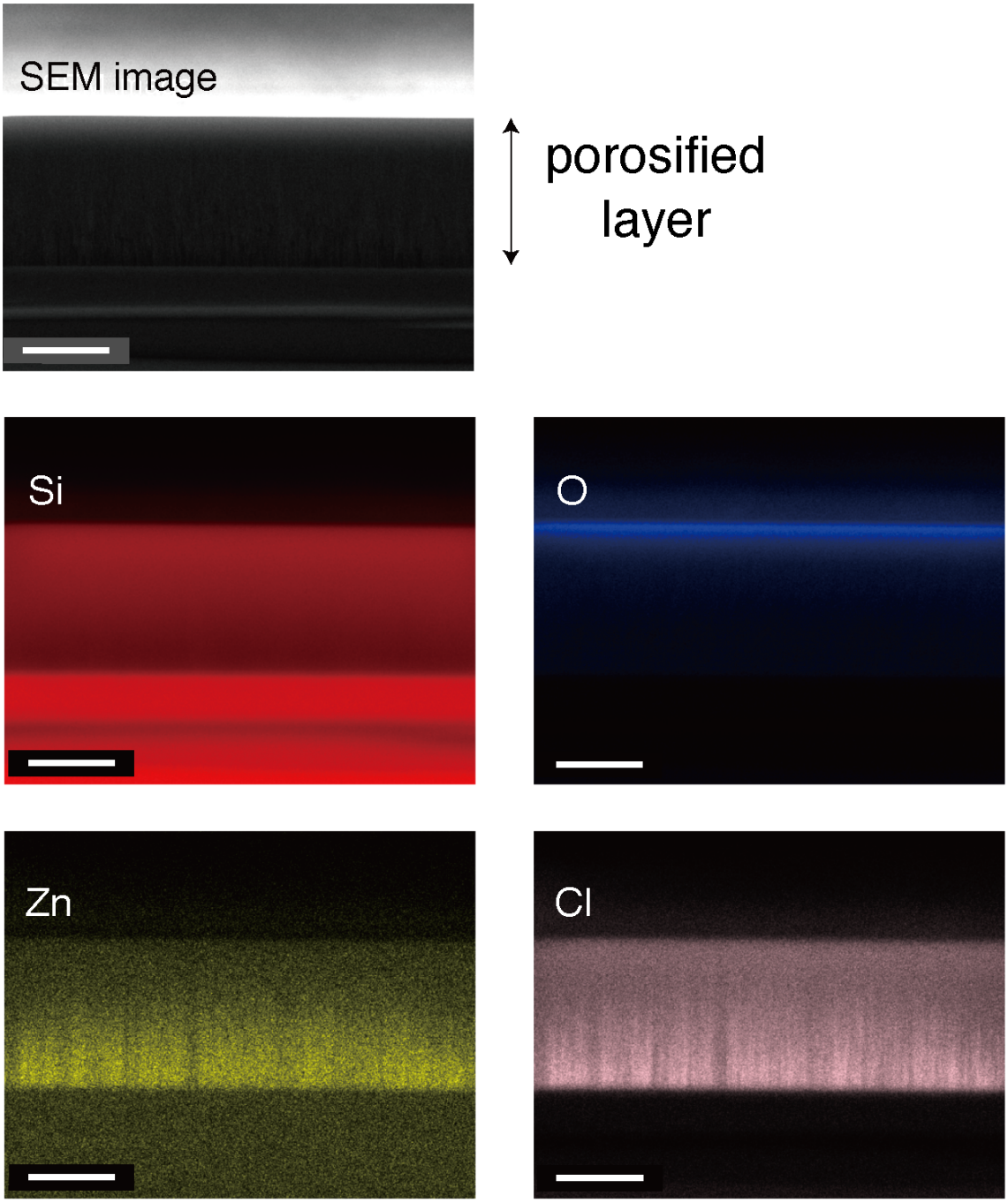

Figure 3.6 SEM image and EDX mappings for the porosified layer of nanoporous Si with the addition of TEACl solution after immersion in $ZnCl_2$ solution for 10 min without cleaning. White line indicates 20 μm.

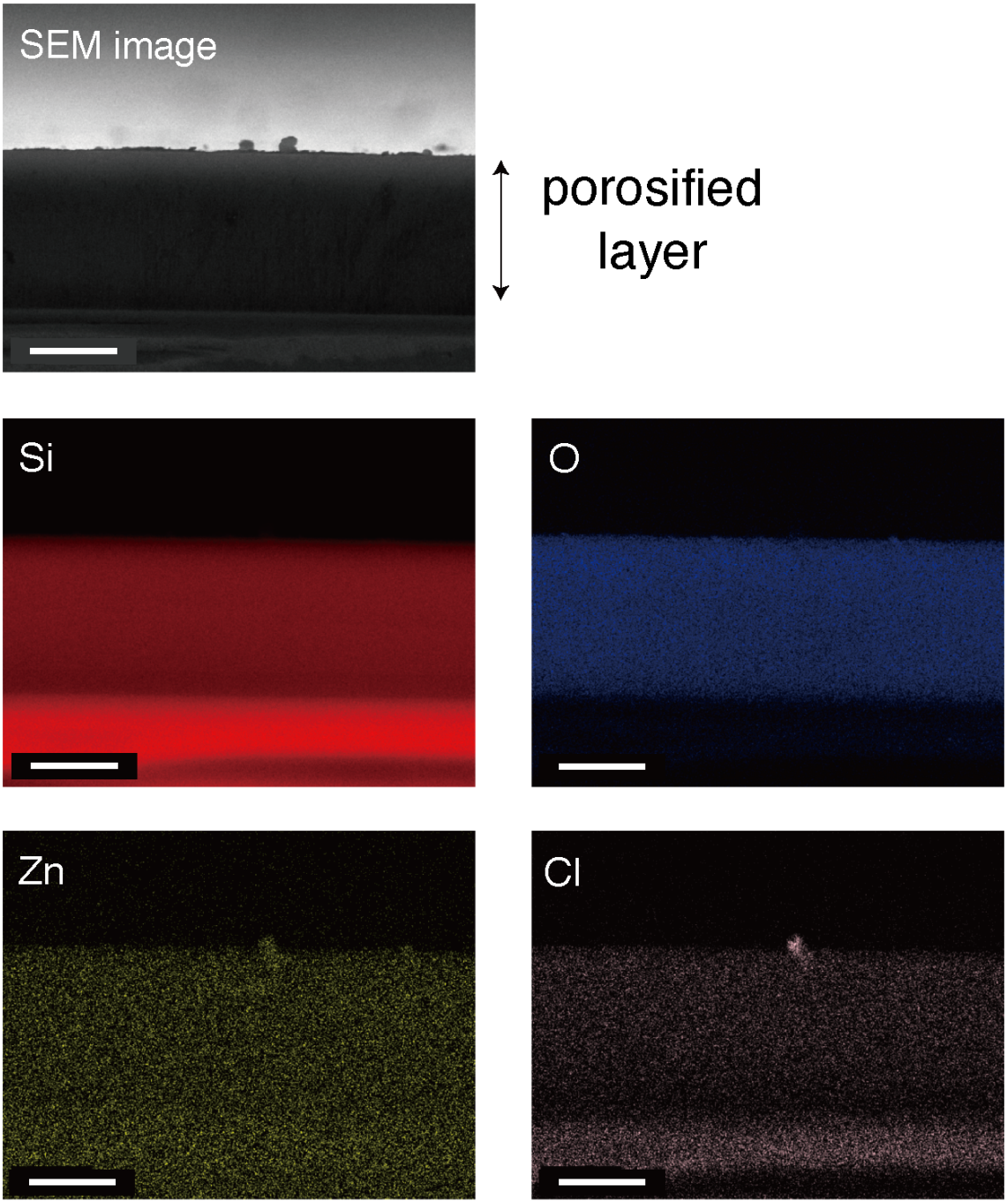

Figure 3.7 SEM image and EDX mappings for the porosified layer of nanoporous Si when adding TEACl solution after immersion in $ZnCl_2$ solution for 10 min with cleaning. White line indicates 20 μm.

In this study, two types of nanoporous Si are used: that with 17 nm in diameter and 36 μm in thickness, and that with 2 nm in diameter and 2 μm in thickness. In the case of 17 nm in diameter, the unique property of the confined solutions is considered to become more dominant with increasing the thickness of the porosified layer. This is because the area fraction of pore surfaces increases compared to the top surface of the layer that contacts the bulk solution. Therefore, the thickness should have an effect on the unique property of the aqueous solutions confined within the nanopores. On the other hand, in the case of 2 nm in diameter, the thickness is considered to exhibit a weak effect on the property of the solution confined because the area fraction is high enough with the thickness being 2 μm.

3.4. Discussion

3.4.1. Dissolution state of zinc cations within hydrophobic nanopores.

According to the EDX mappings in Figure 3.4, zinc and chlorine are detected throughout the porosified layer after immersion in the 0.2 M $ZnCl_2$ solution for 10 min. Because hydrated Zn^{2+} and Cl^- are hydrophilic due to their large charge densities, these ions should be unstable within the hydrophobic nanopores of porous Si. For this reason, Figure 3.4 seems to contradict the instability of hydrophilic ions within hydrophobic nanopores. Recent analysis on the potential of the mean force between oppositely charged particles in ionic liquids has revealed that a particle pair becomes weakly solvophobic when they are coupled.[30] The positive and negative particle pair behaves as if it is a single particle with a low surface charge density.[11] The high ion concentration and the short mean distance between oppositely charged ions lead to a similar coupling between Zn^{2+} and Cl^-, resulting in the formation of a hydrophobic pair with a lower surface

charge density (Figure 3.8). According to the thermodynamics data,[21] this coupling may lead to the formation of complex ions such as $ZnCl^+$. Therefore, this pair between Zn^{2+} and Cl^- is stabilized within the hydrophobic nanoporous Si and diffuses to all of the hydrophobic nanopores.

3.4.2. Comparison between the experimental and theoretical results for TEA^+ enrichment within the hydrophobic nanopores.

The DSC thermograms shown in Figure 3.3 indicate that the endothermal peak of the TEACl-H_2O eutectic point appears when the bulk TEACl concentration is higher than 2.0 M or 0.5 M in the absence or presence of the nanoporous layer, respectively. The TEA^+ concentration within the nanopores increases *ca*. 4 times compared to the bulk concentration. Theoretical analyses in the previous studies using a statistical mechanical theory have showed that the entropic component plays a significant role in the enrichment of hydrophobic solutes within hydrophobic nanopores.[17,18] The concentration of the hydrophobic ions in nanoporous Si can be orders of magnitude higher than that in the bulk. The present thermal analysis shows that the hydrophobic ions are certainly enriched within the nanopores, but the extent is several times higher at most.

3.4.3. Reactivity of zinc cations confined in nanoporous Si.

Due to the formation of the ion pairs between Zn^{2+} and Cl^- within the hydrophobic nanopores, the isolation of Cl^- from Zn^{2+} is more difficult. This is due to the enhanced stability of the ion pairs. The reason for the suppressed precipitation of zinc hydroxychloride may be related to kinetic factors as well as the increased stability of the ion pairs. There are two possible kinetics factors: the kinetic salt effect and the rigid cage-like structure among water molecules on hydrophobic surfaces. TEA^+ enriched

within the nanopores, which is not related to this precipitation, induces the kinetic salt effect. The enriched TEA^+ cations weaken the Coulomb interaction between the reactants such as the ion pairs and OH^- anions, suppressing precipitation. Moreover, hydrogen-bonding networks among water molecules within the nanopores can suppress this precipitation due to the relatively low mobility of the networks within the nanopores caused by the rigid cage-like structure among water molecules on hydrophobic surfaces.[31,32] These factors may inhibit the isolation of Cl^- from the ion pairs, increasing the activation energy for the precipitation. According to the enhanced stabilities of the ion pairs and these kinetics factors, the precipitation of zinc hydroxychloride does not occur in nanoporous Si. It is doubtless that the length of the alkyl chain does not show a significant impact on the suppression of precipitation. This is because the kinetic salt effect is applicable to the cations with different alkyl chain lengths as well. It should be noted the precipitation of zinc hydroxychloride can be suppressed when the Zn^{2+} concentration is low.

Considering the solubility product for the precipitation of zinc hydroxychloride, the pH required for this precipitation shifts to a higher value when the local Zn^{2+} concentration within the nanopores becomes low. The present study uses the solution of 0.2 M $ZnCl_2$. If the Zn^{2+} concentration within the nanopores becomes one-hundredth of the bulk solution, this is equivalent to a shift of the equilibrium pH to 7.5. According to the electrochemical measurements, the expected pH after the TEA^+ penetration is 8.4. This suggests that the precipitation must occur within the nanopores if the thermodynamics of the bulk solution is simply applicable to the system confined within the nanopores. However, precipitation of zinc compounds is not detected in the nanopores, strongly suggesting that the enhanced stability of the ionic species in the nanopores is derived from the formation of the hydrophobic ion pairs and the above kinetic factors.

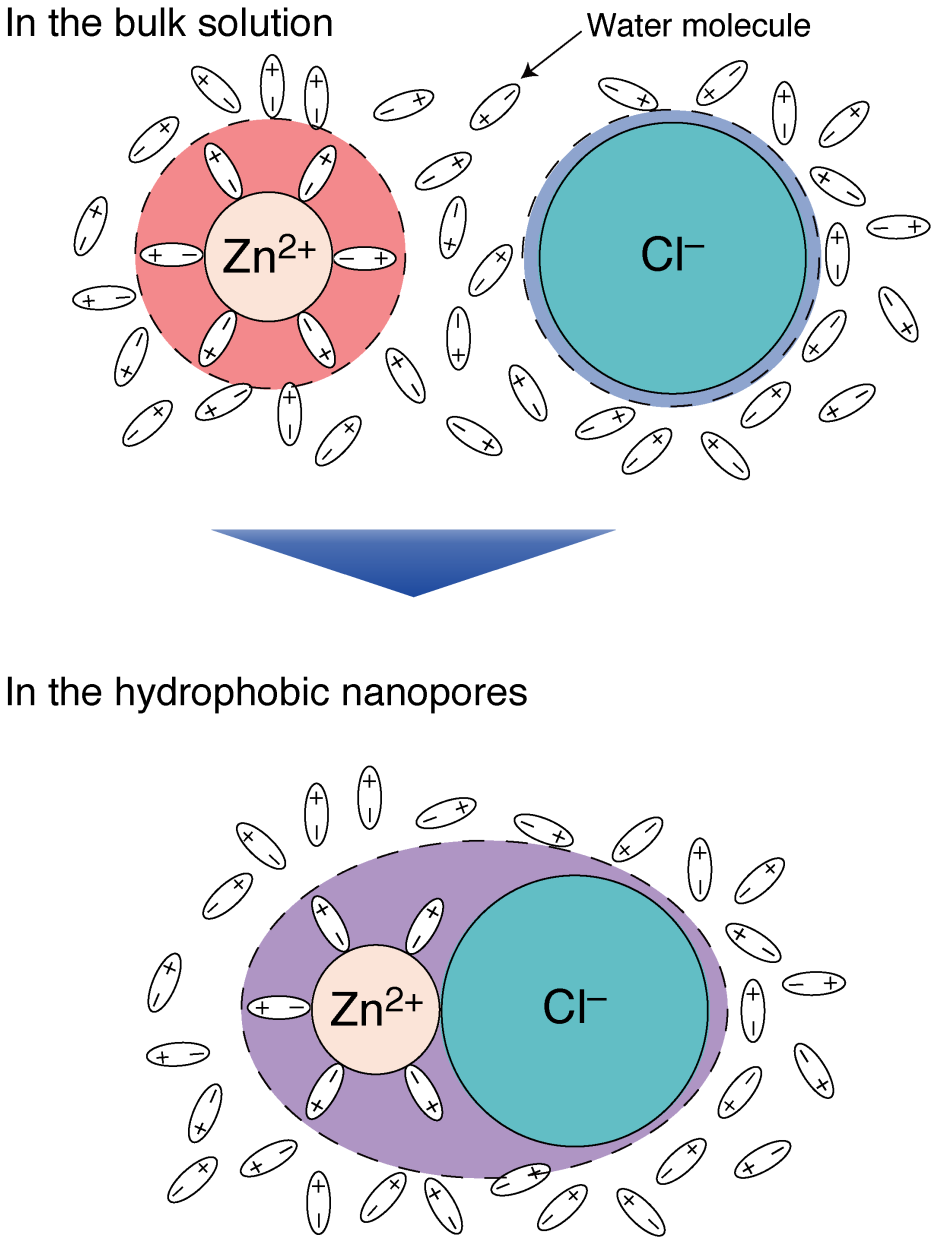

Figure 3.8 Schematic images of the ionization states in bulk 0.2 M $ZnCl_2$ solution and the solution confined within the hydrophobic nanopores of porous Si. In the bulk 0.2 M $ZnCl_2$ solution, Zn^{2+} cations and Cl^- anions are uniformly ionized. Zinc and chlorine are detected within the hydrophobic nanopores. Although the hydrophobic surfaces of the nanopores are not favorable to hydrophilic Zn^{2+} and Cl^-, the detection of zinc and chlorine suggests the formation of hydrophobic ion pairs between Zn^{2+} and Cl^- within the hydrophobic nanopores.

3.5. Conclusions

The enrichment behavior of hydrophobic ions and the phase transition within the nanopores of porous Si were investigated as a function of the bulk TEACl concentration. Open-circuit potential measurements revealed an increase in the local pH within the nanopores with the bulk TEACl concentration. DSC thermograms indicated that TEA^+ cations are enriched and the concentration of OH^- remarkably increases within the nanopores when the bulk TEA^+ concentration is extremely high. Therefore, the ion enrichment behavior and the phase transition within the nanopores become more prominent when the bulk concentration of TEA^+ is high. The DSC thermograms strongly suggest that the enrichment of the hydrophobic TEA^+ is not high compared with the expectation based on the previous theoretical analyses. The selective precipitation of metal hydroxide within the nanopores where the local pH increases was also attempted. However, contrary to the expectation from the thermodynamics applied in the bulk solution, the precipitation expected was not observed in the investigations using aqueous solutions containing zinc cations. This contradiction originates from the formation of the hydrophobic ion pairs with an enhanced stability and the kinetics factors with an increased activation energy for precipitation. The enhanced stability and the increased activation energy can explain the low reactivity for the precipitation of zinc hydroxychloride in the confined nanopores. In the previous studies, the enrichment of hydrophobic solutes within the hydrophobic nanopores based only on the *thermodynamics* has been discussed. The newly found physicochemical point to be discussed in this paper is the low reactivity of dissolved species within the nanopores affected by *kinetics factors* as well as the thermodynamics.

Although the low reactivity is not preferable to design a porous material as a host matrix for reactions, it certainly provides important insight.

Namely, the thermodynamics of bulk solutions cannot be applied directly to nanoporous systems. This result will open further studies on the design of highly concentrated aqueous solutions using nanoporous materials. As mentioned in the introduction, highly concentrated aqueous solutions without precipitation have attracted keen attention. The author believes that the combination between the design of nanoporous materials and the control of the liquid state in view of their hydration properties is an important strategy to design novel rechargeable batteries whose aqueous electrolytes work under the condition where metal oxides are expected to be precipitated in the bulk condition.

Refferences

1. C. A. Angell, *J. Electrochem. Soc.*, **112**, 1224 (1965).
2. C. T. Moynihan, C. R. Smalley, C. A. Angell, and E. J. Sare, *J. Phys. Chem.*, **73**, 2287 (1969).
3. C. A. Angell and J. C. Tucker, *J. Phys. Chem.*, **78**, 278 (1974).
4. L. Suo, O. Borodin, T. Gao, M. Olguin, J. Ho, X. Fan, C. Luo, C. Wang, and K. Xu, *Science*, **350**, 938 (2015).
5. Y. Yamada, K. Usui, K. Sodeyama, S. Ko, Y. Tateyama, and A. Yamada, *Nat. Energy*, **1**, 1 (2016).
6. P. Lannelongue, R. Bouchal, E. Mourad, C. Bodin, M. Olarte, S. le Vot, F. Favier, and O. Fontaine, *J. Electrochem. Soc.*, **165**, A657 (2018).
7. W. Deng, X. Wang, C. Liu, C. Li, J. Chen, N. Zhu, R. Li, and M. Xue, *Energy Storage Mater.*, **20**, 373 (2019).
8. K. Adachi, A. Kitada, K. Fukami, and K. Murase, *Electrochim. Acta*, **338**, 135873 (2020).
9. Q. Huang and Y. Hu, *J. Electrochem. Soc.*, **165**, D796 (2018).
10. A. Uehara, O. Shirai, T. Fujii, T. Nagai, and H. Yamana, *J. Appl.*

Electrochem., **42**, 455 (2012).
11. A. M. Smith, A. A. Lee, and S. Perkin, *J. Phys. Chem. Lett.*, **7**, 2157 (2016).
12. S. Jonchhe, S. Pandey, T. Emura, K. Hidaka, M. A. Hossain, P. Shrestha, H. Sugiyama, M. Endo, and H. Mao, *Proc. Natl. Acad. Sci. U. S. A.*, **115**, 9539 (2018).
13. K. Mawatari, Y. Kazoe, H. Shimizu, Y. Pihosh, and T. Kitamori, *Anal. Chem.*, **86**, 4068 (2014).
14. W. Choi, Z. W. Ulissi, S. F. E. Shimizu, D. O. Bellisario, M. D. Ellison, and M. S. Strano, *Nat. Commun.*, **4**, 1 (2013).
15. K. V. Agrawal, S. Shimizu, L. W. Drahushuk, D. Kilcoyne, and M. S. Strano, *Nat. Nanotechnol.*, **12**, 267 (2017).
16. K. Otake, K. Otsubo, T. Komatsu, S. Dekura, J. M. Taylor, R. Ikeda, K. Sugimoto, K. Fujiwara, C. P. Chou, A. W. Sakti, Y. Nishimura, H. Nakai, and H. Kitagawa, *Nat. Commun.*, **11** (2020).
17. K. Fukami, R. Koda, T. Sakka, Y. Ogata, and M. Kinoshita, *J. Chem. Phys.*, **138** (2013).
18. R. Koda, A. Koyama, K. Fukami, N. Nishi, T. Sakka, T. Abe, A. Kitada, K. Murase, and M. Kinoshita, *J. Chem. Phys.*, **141** (2014).
19. A. Koyama, K. Fukami, T. Sakka, T. Abe, A. Kitada, K. Murase, and M. Kinoshita, *J. Phys. Chem. C*, **119**, 19105 (2015).
20. A. Koyama, K. Fukami, Y. Suzuki, A. Kitada, T. Sakka, T. Abe, K. Murase, and M. Kinoshita, *J. Phys. Chem. C*, **120**, 24112 (2016).
21. A. Koyama, K. Fukami, Y. Imaoka, A. Kitada, T. Sakka, T. Abe, K. Murase, and M. Kinoshita, *Phys. Chem. Chem. Phys.*, **19**, 16323 (2017).
22. M. Kinoshita, *J. Solution Chem.*, **33**, 661 (2004).
23. M. Kinoshita, *Biophys. Rev.*, **5**, 283 (2013).
24. S. Peulon and D. Lincot, *J. Electrochem. Soc.*, **145**, 864 (1998).
25. C. Faivre, D. Bellet, and G. Dolino, *Eur. Phys. J. B*, **7**, 19 (1999).
26. A. Schreiber, I. Ketelsen, and G. H. Findenegg, *Phys. Chem. Chem.*

Phys., **3**, 1185 (2001).
27. M. R. Landry, *Thermochim. Acta*, **433**, 27 (2005).
28. L. S. Aladko, *Russ. J. Gen. Chem.*, **79**, 1613 (2009).
29. L. S. Aladko, *Russ. J. Inorg. Chem.*, **56**, 2009 (2011).
30. K. Amano, T. Hayashi, K. Hashimoto, N. Nishi, and T. Sakka, *J. Mol. Liq.*, **257**, 121 (2018).
31. N. Galamba, *J. Phys. Chem. B*, **117**, 2153 (2013).
32. D. Laage, G. Stirnemann, and J. T. Hynes, *J. Phys. Chem. B*, **113**, 2428 (2009).

General conclusions

In this work, the author comprehensively studied electrochemical reactions using concentrated aqueous electrolytes in the view of the effects of dissolved ions on water molecules. The solute concentrations highlighted the effects of dissolved ions and thus affected electrochemical reactions that are directly and/or indirectly associated with water. Tf_2N^- anions that break the hydrogen-bonding networks among water molecules were applied to Zn electrodeposition competing with hydrogen evolution and adsorption. The use of concentrated $Zn(Tf_2N)_2$ solutions with the breakdown of the networks and the loss of free water gave the basal-plane oriented Zn was obtained because the adsorption was suppressed and the growth of the electrodeposits promoted. The effects of the breakdown were also verified to observe the H_{upd} adsorption/desorption on Pt electrodes in acidic solutions with high concentration of lithium salts. The desorption behavior for the $LiTf_2N$ or $LiClO_4$ solutions with the breakdown differed from that for the LiCl cases without the breakdown, indicating that the breakdown affects the local pH in the vicinity of the Pt electrode. This is because the ionic conductions through the hydrogen-bonding networks depends on the anions used in the concentrated aqueous solutions. The author also evaluated the effects of bulk concentration of hydrophobic TEA^+ cations on their accumulation within hydrophobic nanopores of porous Si and the hydrolytic reactivity of metal cations under the accumulation. Increasing the TEA^+ concentration enhanced the accumulation and thus the decrease in local pH within the nanopores. Besides, the hydrolysis of zinc cations that was predicted to occur with increasing the local pH was kinetically suppressed due to the unique properties in the nanopores with the TEA^+ accumulation.

Although concentrated aqueous electrolytes have been recently

attracted due to both suppressed water electrolysis and easy handling, many hidden potentials for the concentrated systems are still present. The author believes that the findings presented here help improve electrochemical processes and develop electrochemical devices with good performances using concentrated aqueous electrolytes.

List of publications

Chapter 1

Shota Inoguchi, Atsushi Kitada, Kazuhiro Fukami, and Kuniaki Murase,
‘‘Basal-Plane Orientation of Zn Electrodeposits Induced by Loss of Free Water in Concentrated Aqueous Solutions’’,
Journal of the Electrochemical Society, **167**(16), 162511/1-9 (2020).

Chapter 2

Shota Inoguchi, Kazuhiro Fukami, Atsushi Kitada, and Kuniaki Murase,
‘‘Hydrogen Adsorption and Desorption on a Platinum Electrode in Acidic Solutions Containing Lithium Salts with Extremely High Concentrations’’,
Submitted.

Chapter 3

Shota Inoguchi, Kazuhiro Fukami, Ken-ichi Amano, Atsushi Kitada, and Kuniaki Murase,
‘‘Reactivity of Zinc Cations under Spontaneous Accumulation of Hydrophobic Coexisting Cations in Hydrophobic Nanoporous Silicon’’,
*ACS Omeg*a, **5**(41), 26894-26901 (2020).

Acknowledments

This work was carried out under the supervision of Professor Kuniaki Murase, Department of Materials Science and Engineering, Graduate School of Engineering, Kyoto University. First of all, I would like to express my sincere gratitude to Professor Kuniaki Murase for his consistent guidance and constructive suggestions, and kind support when I was mentally challenged. His guidance and support helped me research and writing of this thesis.

I am also profoundly grateful to Professor Tetsuya Uda, Department of Materials Science and Engineering, Kyoto University, and Professor Tetsuo Sakka, Department of Energy and Hydrocarbon Chemistry, Kyoto University, for their careful review, critical comments, and encouragement on this thesis.

My sincere thanks also go to Associate Professor Kazuhiro Fukami at Department of Materials Science and Engineering, Graduate School of Engineering, Kyoto University, for his helpful comments, continuous encouragement, tremendous supports that were essential to complete this work. Special thanks to Assistant Professor Atsushi Kitada, Department of Materials Science and Engineering, Graduate School of Engineering, Kyoto University, for his generous guidance, insightful advice, and thorough teaching me academic writing.

I would like to express my deep appreciation to Associate Professor Ken-ichi Amano, Faculty of Agriculture, Meijo University, for his fruitful discussions that helped me finish my research.

Deep thanks are expressed to the assistant administrative staff of Murase laboratory, Ms. Akiko Yasui and Ms. Sari Nakano, who provided strong supports to me that allowed me to focus on my research.

Thank you to all the members of Murase laboratory from the past to the

present. That time I spent with my fellow labmates will definitely become an unforgettable memory for me. Particular thanks to Dr. Ken Adachi, Dr. Tianyu Chen, Dr. Zelei Zhang, Mr. Takumi Yasuda, Mr. Takahiro Mori, for their insightful advice, invaluable discussions, and the supremely fulfilling time we had.

Finally, I would like to express my deep appreciation to my parents, Kouji and Hiromi Inoguchi, for their understanding, support, and encouragement.

March 2021

Shota Inoguchi